THERMAL PERFORMANCE OF 4-LOBE SWIRL GENERATOR UNDER DIFFERENT TWISTED ANGLES AND β-TRANSITION USING GO-CuO/WATER AND SiO2/WATER NANOFLUIDS

By

AYAD FARAG ABD ALLAH DIABIS

Thesis Submitted to the School of Graduate Studies, Universiti Putra Malaysia, in Fulfilment of the Requirements for the Degree of Doctor of Philosophy

April 2024

FK 2024 64

DEDICATION

I dedicate this thesis to the relationships that surrounded me during my study, including my family and friends, who provided inspiration, support, and encouragement. I also dedicate my dissertation work to my supervisory committee: Professor Ir. Ts. Dr. Abd Rahim Abu Talib, Associate Professor Ts. Dr. Norkhairunnisa Mazlan and Associate Professor Dr. Eris Elianddy Supeni, thank you for your invaluable assistance throughout my academic journey.

Abstract of thesis presented to the Senate of Universiti Putra Malaysia in fulfilment of the requirement for the degree of Doctor of Philosophy

THERMAL PERFORMANCE OF 4-LOBE SWIRL GENERATOR UNDER DIFFERENT TWISTED ANGLES AND β-TRANSITION USING GO-CuO/WATER AND SiO2/WATER NANOFLUIDS

By

AYAD FARAG ABD ALLAH DIABIS

April 2024

Chairman : Professor Ir. Ts. Abd Rahim bin Abu Talib, PhD
Faculty : Engineering

Heat transfer enhancement has been the target outcome of many researchers in the thermal engineering application. A lobed swirl generator has been applied in the application of fluid flow due to its ability to produce a high swirl intensity and reduce the pressure drop when placed before a smooth channel. It is worth mentioning that no study has been reported to have performed the enhancement by combining both the lobed swirl generator and its transition parts with hybrid and single nanofluids in a thermal application. A lot of studies have proved that swirl flow techniques come with an increase in the penalty pressure drop. Therefore, the phenomena of lobed swirl generators in reducing the pressure loss have to be considered in order to identify unique methods to increase heat transfer with an acceptable level of pressure drop as a crucial factor in determining the pumping power and eventual cost. In addition, exploring the thermal characteristics of this device for more understanding is the motivation behind this study. In the present work, the thermal performance of a four-lobed swirl generator was investigated numerically and experimentally under different

parameters such as twisted angles (ranging from 90º to 450º), transition multiplier values (ranging from n = 0.25 to 0.75 mm), and variable helix dimensions (t = 0.5 to 1.5 mm). The working fluids adopted are water, different nanofluids, including SiO_2, Al_2O_3, and CuO, with volume concentrations ranging from 1% to 5% in water and hybrid nanofluid GO-CuO/water with volume fractions varying from 0.15% to 0.75% under different Reynolds numbers (ranging from 15,000 to 55,000). The turbulence swirling flow is modelled using the shear-stress transport (SST) k-ω model. According to the obtained results, the lobed swirl generator at (θ =360) and beta transition of (n = 0.5 mm) and (t =1 mm), the heat transfer and pressure loss increase compared with plain tube by 28.78 % and 17.35 %, respectively; and by reducing the value to (n = 0.25 mm), a slight increase in heat transfer and pressure loss in the percentage by 40.32 % and 17.89 %, respectively are observed. A maximum heat transfer and pressure drop of 49-59% and 33-45% were obtained with SiO_2/water with a volume concentration of 5% and a Reynolds number of 15,000. The heat transfer and pressure drop experimental results showed a maximum improvement of 65-78.57% and 36-47%, respectively, at Reynolds number 15,000 and a volume fraction of 0.75%. Finally, the study proposed a novel empirical correlation related to the thermal conductivity experimental data of GO-CuO/hybrid nanofluid.

Keywords: Heat transfer enhancement, Lobed swirl generator, CFD, Nanofluid, Experimental study

SDG: GOAL 3: Affordable and clean energy, industry, innovation and infrastructure

Abstrak tesis yang dikemukakan kepada Senat Universiti Putra Malaysia sebagai memenuhi keperluan untuk ijazah Doktor Falsafah

PRESTASI TERMA PENJANA PUTAR 4-LOBE DI BAWAH SUDUT PULIH YANG BERBEZA DAN PERALIHAN β MENGGUNAKAN NANO BENDALIR GO-CuO/AIR DAN SiO2/AIR

Oleh

AYAD FARAG ABD ALLAH DIABIS

April 2024

Pengerusi : Professor Ir. Ts. Abd Rahim bin Abu Talib, PhD
Fakulti : Kejuruteraan

Peningkatan pemindahan haba telah menjadi fokus utama para penyelidik dalam aplikasi kejuruteraan haba. Penjana pusaran lob telah digunakan dalam aplikasi aliran bendalir kerana kemampuannya menghasilkan intensiti pusaran yang tinggi dan mengurangkan kejatuhan tekanan apabila diletakkan sebelum saluran licin. Perlu diingatkan bahawa tiada kajian yang dilaksanakan untuk peningkatan dengan menggabungkan penjana pusaran lob dan bahagian peralihan dengan nanobendalir hibrid dan tunggal dalam aplikasi terma telah dilaporkan. Banyak kajian membuktikan bahawa teknik aliran pusaran datang dengan peningkatan kejatuhan tekanan penalti. Oleh itu, fenomena penjana pusaran lob dalam mengurangkan kehilangan tekanan perlu dipertimbangkan untuk mengenal pasti kaedah unik untuk meningkatkan pemindahan haba dengan tahap kejatuhan tekanan yang boleh diterima sebagai faktor penting dalam menentukan kuasa pam dan kos keseluruhan. Selain itu, meneroka ciri-ciri terma peranti ini untuk pemahaman yang lebih mendalam adalah motivasi di sebalik kajian ini. Dalam kajian ini, prestasi terma penjana pusaran berlob empat telah diselidiki secara numerikal dan eksperimen di bawah parameter yang berbeza seperti sudut berpintal (berkisar antara 90º hingga 450º), nilai pengganda peralihan (berkisar dari n = 0.25 hingga 0.75 mm), dan dimensi heliks berubah (t = 0.5 hingga 1.5 mm). Bendalir kerja yang digunakan adalah air, pelbagai nanobendalir termasuk SiO_2, Al_2O_3, dan CuO dengan kepekatan isipadu dari 1% hingga 5% dalam air dan nanobendalir hibrid GO-CuO/air dengan pecahan isipadu berbeza dari 0.15% hingga 0.75% di bawah pelbagai nombor Reynolds (berkisar dari 15,000 hingga 55,000). Aliran pusaran bergelora dimodelkan menggunakan model k-ω pengangkutan tegasan ricih (SST). Menurut keputusan yang diperoleh, penjana pusaran berlob pada (θ =360) dan peralihan beta (n = 0.5 mm) dan (t = 1 mm), peningkatan pemindahan haba dan kehilangan tekanan dibandingkan dengan tiub biasa masing-masing sebanyak 28.78% dan 17.35%; dan dengan mengurangkan nilai kepada (n = 0.25 mm), sedikit peningkatan dalam pemindahan haba dan kehilangan tekanan dalam peratusan sebanyak 40.32% dan 17.89% masing-masing diperhatikan. Peningkatan maksimum dalam pemindahan haba dan kejatuhan tekanan masing-masing adalah 49-59% dan 33-45% diperoleh dengan SiO_2/air dengan kepekatan isipadu 5% dan nombor Reynolds sebanyak 15,000. Keputusan eksperimen pemindahan haba dan kejatuhan tekanan menunjukkan peningkatan maksimum sebanyak 65-78.57% dan 36-47% masing-masing pada nombor Reynolds 15,000 dan pecahan isipadu sebanyak 0.75%. Akhirnya, kajian ini mencadangkan korelasi empirikal baharu yang berkaitan dengan data eksperimen konduksi terma nanobendalir hibrid GO-CuO.

Kata kunci: Penambahbaikan pemindahan haba, Penjana pusaran bercuping, Dinamik Bendalir Berkomputer, nanobendalir, kajian eksperimen

SDG: MATLAMAT 3: Mampu milik dan tenaga bersih, industri, innovasi dan infrastruktur

ACKNOWLEDGEMENTS

First and foremost, I would like to express my gratitude to Allah for His blessings and guidance throughout my life. I want to extend my heartfelt thanks to Professor Ir. Ts. Dr. Abd Rahim Abu Talib, thank you for dedicating your time, effort, and expertise to guide me during my studies. The valuable memories and lessons we shared have been instrumental in my academic journey, and his motivation has driven me to excel in all aspects of my life.

I also want to thank my supervisory committee, Associate Professor Ts, sincerely. Dr Norkhairunnisa Mazlan and Associate Professor Dr Eris Elianddy Supeni, thank you for your invaluable contributions and support. I hold deep respect and gratitude to my classmates for your advice, guidance, and collaboration throughout this journey.

I am profoundly thankful to my parents and siblings for their unwavering love, encouragement, and dedication. I believe that the prayers of my family, especially my mother, have played a significant role in my accomplishments.

To all my friends, your unwavering support has strengthened me during challenging times. Lastly, I thank my brother, Dr. Ali Kareem Hilo, for his continuous support and care throughout my studies.

This thesis was submitted to the Senate of the Universiti Putra Malaysia and has been accepted as fulfilment of the requirement for the degree of Doctor of Philosophy. The members of the Supervisory Committee were as follows:

Abd Rahim bin Abu Talib, PhD
Professor Ir. Ts.
Faculty of Engineering
Universiti Putra Malaysia
(Chairman)

Norkhairunnisa binti Mazlan, PhD
Associate Professor
Faculty of Design and Architecture
Universiti Putra Malaysia
(Member)

Eris Elianddy bin Supeni, PhD
Associate Professor
Faculty of Engineering
Universiti Putra Malaysia
(Member)

ZALILAH MOHD SHARIFF, PhD
Professor and Dean
School of Graduate Studies
Universiti Putra Malaysia

Date: 17 April 2025

TABLE OF CONTENTS

LIST OF TABLES

LIST OF FIGURES

LIST OF ABBREVIATIONS

A	area (m^2)
$\dot{m}$	mass flow rate (m^2/s)
H	heat transfer coefficient ($W/m^2.K$)
Q	heat transfer (W)
Nu	Nusselt number
Nu_o	Nusselt number at plane tube
Pr	Prandtl number
K	thermal conductivity (W/m.K)
Re	Reynolds number
ΔP	pressure drop (Pa)
ΔT	temperature different
L	test section length (m)
N	velocity (m/s)
F	friction factor
f_o	friction factor at plane tube
R	test section radius (m)
T	temperature (K)
Cp	Specific heat (J /kg.K)
L	test section length (m)
Le	entry section length (m)
Lobed swirl notation	
A_{4L}	area of four segments (mm^2)
r_{lobe}	lobe swirl radius (mm)
R_{cs}	swirl core radius (mm)
P_{4L}	four lobe perimeter (mm)

LA_i	intermediate area (mm)
LA_{FD}	fully developed area (mm^2)
B	beta transition
A	alpha transition
N	transition multiplier (mm)
L_t	length of transition (m)
$f\&f_1$	variables to facilitate y calculation
Y	variable length from transition core origin (mm)
Υ	increment angle during lobe development (degree)
X	Intermediate lobe length (mm)
L_t	transition part length (m)
De	equivalent diameter (mm)
l	twisted length (m)
L	Total lobe length (m)
Creek letter	
ρ	density (kg/m^3)
μ	viscosity kg/m.s
Φ	solid volume concentration
θ	twisted angle (^{o})
Sup/Superscripts	
S	m^2
P	plane tube
Ave	average
In	inlet
B	bulk temperature
Cs	circle inscribe

FD	fully developed
I	intermediate

Abbreviations

PEC	Performance Evaluation Criteria
LSG	Lobe Swirl Generator
DSC	Differential Scanning Calorimetry
SEM	Scanning Electron Microscope
CFD	Computational Fluid Dynamic
SST	Shear-Stress Transport
ICM-CFD	Integrated Computer Engineering and Manufacturing

CHAPTER 1

INTRODUCTION

1.1 Background

The increase in industrial development and human population in recent decades is associated with increasing demand for energy globally. Despite the potential of green energy sources as the future alternative energy, fossil fuels remain the primary global energy source. The application of various global thermal energy technologies is efficient at different costs and offers a correct economic development process by utilizing multiple fossil fuels by enhancing throughout the globe (Patel, 2023). CO_2 results from most thermal energy sources, including waste heat recovery, nuclear, solar, and fossil fuel combustion. As a result, the effect of CO_2 on the environment has been investigated for many years and is constantly being improved (Cheng et al., 2021). Fossil fuels, including coal, natural gas, and oil, have been extensively utilized in energy production and are anticipated to continue being the primary energy source until 2050. Fossil fuels are used to produce energy and chemicals, which release solid particles and greenhouse gases into the atmosphere that cause global climate change. These gases include carbon dioxide, nitrogen oxides, and other volatile molecules (Megia et al., 2021). The heating and cooling industry is crucial because the sector now consumes half of all energy produced worldwide. In 2018, fossil fuels, primarily natural gas, accounted for 75% of all heating and cooling energy (Lindroos et al., 2021). Therefore, creating more effective heat exchangers would make it possible to use better energy, which benefits the system operator monetarily and reduces energy consumption (i.e., decreased consumption of fossil fuels) (Mousa et al., 2021). However, the increasing cost of energy and the poor performance of equipment used for harnessing natural energy have necessitated innovative techniques to improve the performance of this equipment. Over the past century, many innovations have been employed to improve the thermal performance of heat transfer applications.

A swirling flow is one type of complex flow that occurs under the effect of different parameters. It is caused by a spiral-shaped structure which generates azimuthal and axial velocity downstream (Tang et al., 2015a). Heat transfer improvement techniques in twisted tape can be divided into two categories: (i) curvature wall, which leads to secondary motions and fluid flow increase by particular geometrical characteristics, and (ii) fluid flow enhancement at the core region and the adjacent wall (Eiamsa-Ard et al., 2013). The centrifugal phenomena associated with lobed swirl flow are considered the most crucial factor leading to an increase in the level of turbulent flow (Gorelikov et al., 2021). A swirl tube is a practical cooling technique for thermally demanding components because it increases rotational velocity and improves turbulent fluid (Biegger et al., 2015). Royds (1921) is the first researcher to study swirl flow's impact on enhancing heat transfer. The structure of the swirl flow is a vital step in improving the heat transfer rate by destroying the thermal boundary layer (Pang et al., 2021). Applying one or more of the following classifications is beneficial in promoting the thermal boundary layer and increasing the rate of heat transfer with an undesirable rise in friction augmentation: (i) disturbing the boundary layer by increasing the angular turbulence, (ii) increasing the heat transfer area, and (iii) swirling flows generation (Promvonge, 2008). The increased heat rate has resulted from the improved swirl flow, promoting turbulent flow and creating a thin, viscous boundary layer (Al-Obaidi & Sharif, 2021). The lobe cross-section is one of the latest innovative devices (Jafari et al., 2017b). C. Ariyaratne & Jones (2007) inserted two types of transition parts (cylindrical and lobed shape) on a lobed swirl tube to examine their impact on tangential velocity, pressure loss and swirl effectiveness. Due to the sudden change of transition shape between the cylindrical and lobed swirl tube, a high-pressure loss is obtained. Therefore, the gradual change of the transition lobed parts from circular shape to lobed cross-section and vice versa resulted in high swirl effectiveness and was considered the optimum design.

1.2 Heat Transfer Mechanism in A Swirl Generator

The lobed swirl device's mechanism depends on its curvature shape, which is the main reason for converting the straight flow from the smooth channel upstream to the spiral flow toward the smooth channel downstream. The mechanism of applying a lobed device in the field of heat transfer is represented in (i) The characteristics of its curvature geometry, which results in promoting the velocity and secondary flow, and (ii) creating the fluctuation flow between the core and the wall (Omidi & Farhadi, 2018). The features of the swirling flow of intensive swirl flow, a reduction in the thermal boundary layer, and turbulent fluid close to the wall play the leading role in promoting a higher heat transfer rate over single-phase as well as multiphase flows (Ajeel et al., 2019). As seen in Figure 1.1, three separate swirl types were identified by Hoekstra et al., (1999) based on the radial velocity pattern. The first type, called Concentrate Vortex (CV), occurs when the rotation occurs close to the pipe centre. The second type is Solid Body (SB), which is characterized as a rotational uniform. The third one, known as Wall Jet (WJ), is highly dependent on the angular momentum; in this case, the swirl is concentrated adjacent to the wall.

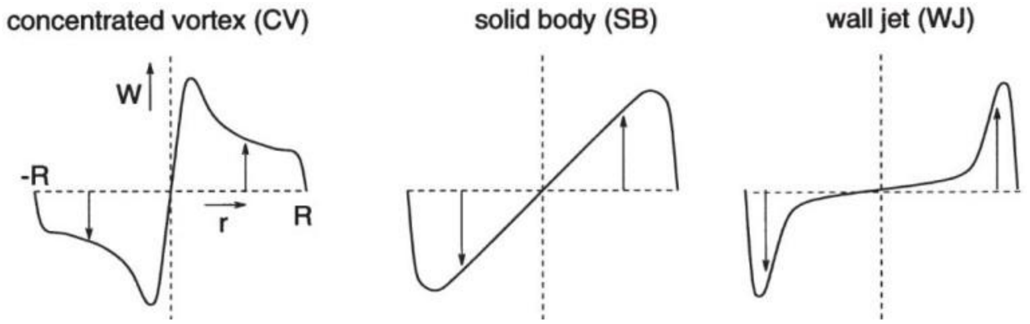

Figure 1.1: Categorization of swirl types (Hoekstra et al., 1999)

One of the three well-known methods listed below can be used to generate the swirling flow: (i) According to the first technique, shown in Figure 1.2(a), fluid flow gains swirl motion as it passes through a rotating section and leaves the pipe as a swirling flow, which is the primary goal of this study, (ii) The second technique, shown in Figure 1.2(b), uses stationary blades (vanes) placed within the pipe at an appropriate angle to ensure a fluid flow into the pipe, and (iii) The third technique, shown in Figure 1.2(c), involves the entrance of fluid flow into the pipe so that it can achieve rotational velocity and move into the pipe as a swirling flow (Najafi et al., 2011).

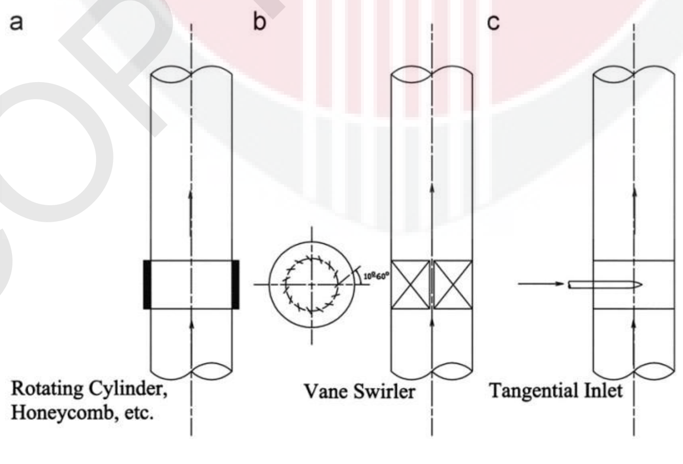

Figure 1.2: Three methods of swirl flow (Najafi et al., 2011)

1.3 Techniques to Improve Heat Transfer in a Circular Tube

Due to the consequences of pressure losses, moving a single or multiphase fluid through a pipe requires a lot of pumping power or energy (H. Liu et al., 2022). There has been an increase in interest in determining ways to use less energy while also increasing pipe flow, particularly when optimizing fluid heat transfer. One of the most essential techniques to overcome this issue is to induce a swirl flow inside the pipeline (Siba et al., 2016). The interaction of vortex and axial motion along the pipe's axis is called swirling flow in the pipe. Heat transfer can benefit from the helical pipe's increased axial velocities and induction of a swirl (Tang et al., 2015a). Over the last few decades, many researchers have encountered the challenges of producing a mechanical whirling flow in a pipeline. Many techniques related to non-circular pipes have been developed to investigate the swirl flow. (Chanchala Ariyaratne, 2005a; G. Li et al., 2015a). Several studies have introduced distinctive varieties of swirl flow generators to improve thermal performance and reduce the pressure drop in heat exchanger tubes. Due to the poor heat transfer associated with smooth channels, several techniques have been developed to generate swirl flow within circular tubes. It can divide the swirl flow induced within a circular tube into different crucial categories: the swirl flow generated by the propeller-type swirl, as seen in Figure 1.3 (Omar Al-Abbasi, 2019), swirl flow by converting the circular tube to several types of curved tubes as illustrated in Figure 1.4 and creating swirl flow by inserting device techniques.

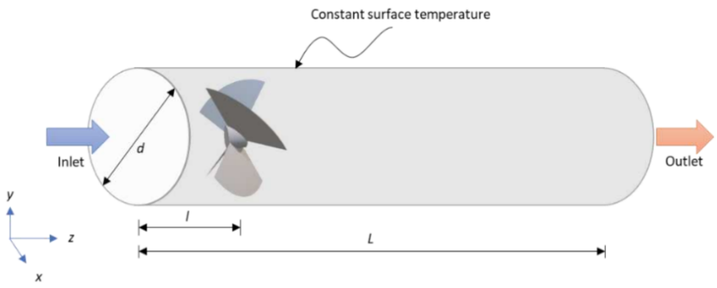

Figure 1.3: Propeller-type swirl inserted inside the smooth channel (Omar Al-Abbasi, 2019)

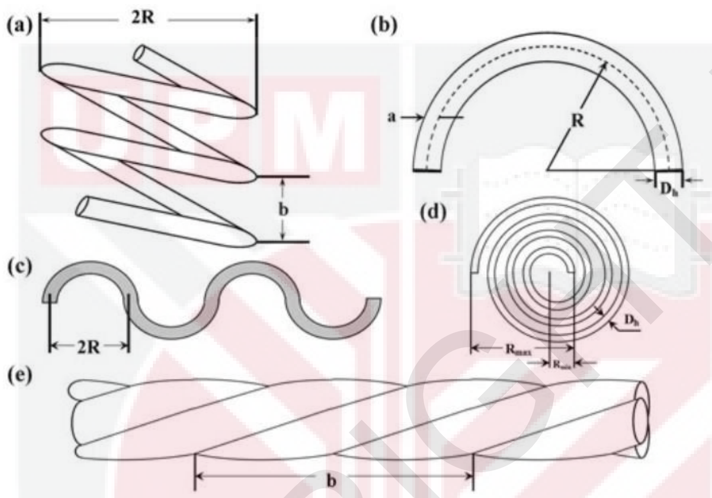

Figure 1.4: Curved tubes under different geometrical structures (a) helical coil, (b) bend tube, (c) serpentine rube, (d) spiral and (e) twisted tubes (Ghobadi & Muzychka, 2016)

The swirl internal flow techniques using the passive method in many industries are a beneficial choice. It is evident from the study mentioned above and our knowledge that implanted swirl generators in heat-exchanging tubes provide higher thermal performance. However, the penalty pressure drop rises along with this improvement in heat transfer, considering the limits of these innovations. There is a more significant pressure drop in conjunction with the thermal improvements using twisted tape techniques due to the blockage of surface area and obstruction of fluid flow (Feizabadi et al., 2019). The insert technique and twisted tape within the flow passage led to less flow area, flow blockage, and viscous effects intensifying due to the augmentation in pressure drop observed (S. V. Patil & Babu, 2011). Although many techniques have recently been developed to increase heat transfer by generating swirl flow inside the smooth channel, The associated augmentation of pressure drop is still a big challenge. Therefore, many steps are required to find unique techniques to improve heat transfer with an applicable pressure-loss change. A lobed swirl generator is one of the essential techniques, with no need to insert technique or place the device in a flow passage.

Moreover, the device has appealing transition parts placed before and after the swirl device itself. The feature of the transition parts is represented by their ability to produce high swirl intensity, reduce the pressure drop, and enhance the overall swirl effectiveness (Ariyaratne, C and Jones, 2007). It is worth mentioning that using a lobed swirl generator in heat transfer is rare. Therefore, placing the lobed swirl generator with its transition parts at the entrance of the smooth channel is expected to generate swirl flow and improve heat transfer, which is the motivation behind the present study.

Although many swirl flow techniques have been innovated to improve heat transfer of heat exchanger surface area, the smooth channel is still a vital step of heat exchangers. The induced swirl flow using corrugated channels led to increased heat transfer associated with augmentation of pressure loss. Therefore, creating swirl flow inside the smooth channel by mounted lobed swirl generator at the entrance of the pipe is the motivation behind this study. The advantage of a lobed swirl generator is represented in its ability to produce high swirl intensity and reduce pressure loss. Moreover, the capability of a lobed swirl generator makes the particles suspension during fluid flow, as well as the ability of nanofluid to improve heat transfer due to the contain of high thermal conductivity, is the motivation for the use of nanofluid and hybrid nanofluid in the present study.

1.4 Problem Statement

The heat transfer regarding smooth channels is considered low due to the poor mixing between the cold flow at the centre and the hot flow adjacent to the wall (Khoshvaght-aliabadi & Ghods-nahry, 2023). Therefore, many studies have been performed to promote heat transfer by generating swirl flow induced within a circular, straight tube. Hence, different studies focused on changing the shape to become a corrugated channel (Ghobadi & Muzychka, 2016). Others used insert techniques (Chaurasia & Sarviya, 2019; Dang & Wang, 2021; D. Kumar et al., 2020). Also, placing the device in a flow passage was the target of several other researchers (Bali & Sarac, 2014; Nikoozadeh et al., 2020; Omar Al-Abbasi, 2019). Due to the reduction of the free flow area, the viscous effect and flow passage blockage occur, leading to an increased pressure drop and limiting the improvement of heat transfer, which were the dominant outcomes of the studies mentioned above (S. V. Patil & Babu, 2011). As a result, there is a need to enhance the thermal performance of smooth channels while considering a balance between promoting heat transfer and maintaining a pressure drop at an acceptable level. The lobed swirl generator is one of the latest innovative devices used to generate swirl flow within a circular tube without changing the geometrical cross-section of the smooth channel itself. It is worth mentioning that the lobed swirl generator with its transition parts is widely used in the field of fluid flow, especially in the area of improved transportation of Particle-Laden Liquids (Tonkin, 2005) and swirl pipe Clean-In-Place procedures (G. Li et al., 2015a). Therefore, the use of this system in the field of thermal application is rare, and the characteristics of the fluid flow in the field of thermal application are new and require further numerical and experimental investigation to understand the behaviour of the swirl flow inside smooth channels, which is the motivation behind this study.

Moreover, the poor thermal conductivity associated with conventional liquids motivates using different nanofluids as a working fluid in the present study. No study has been conducted on a combined lobed swirl generator with its transition components and nanofluids for thermal applications. In addition, several researchers encountered challenges related to sedimentation and agglomeration when using nanofluid (Borzuei & Baniamerian, 2020; Chakraborty & Panigrahi, 2020). Also, using nanofluid linked with most swirl flow techniques led to a considerable increase in pressure drop (Ali et al., 2021). On the other hand, (C. Ariyaratne & Jones, 2007) proved the ability of a lobed swirl generator and its transition parts to keep the particles suspension and prevent the pipeline from blockage, which is also the motivation of the current study and further componential and experimental investigations are required for more understanding. Therefore, this study provides comprehensive data on these complex flows, which will present a practical assessment in the field of thermal application.

1.5 Objectives

This study aims to investigate the thermal performance of lobed swirl generators across various design parameters and working fluids. This aim is realized through the following specific objectives:

1- To evaluate the thermal performance of a lobed swirl generator under various twisted angles,

2- To evaluate the thermal performance of lobed swirl generators across various beta transition (β) values via the effects of changes in transition multipliers (n) and variable helices (t).

3- To compare the thermal performance of lobed swirl generators using water against nanofluids with various concentrations (SiO_2, Al_2O_3, and CuO) as working fluids via simulation analysis.

4- To compare the thermal performance of lobed swirl generators using water against GO-CuO/water hybrid nanofluids as working fluids via experimental analysis.

1.6 The Novelty of the Research

The present research has provided a unique study on the impact of nanofluid and hybrid nanofluid applied over a lobed swirl generator under different geometric parameters on fluid flow and heat transfer on a smooth channel. A new result of the capability of the lobed swirl generator with (SiO_2, Al_2O_3, and CuO) numerically and (GO-CuO/water) hybrid nanofluid experimentally has been carried out. Regarding thermal performance improvement, the highest performance evaluation criteria of 1.67 were recorded for the case of SiO_2/water at a volume fraction of 5% and a Reynolds number of 15,000. According to the heat transfer enhancement, the lobed swirl generator associated with SiO_2-nanofluid presented a high value from 1.35 to 1.87. The outcomes demonstrated the benefit of using nanofluid as a working fluid with a lobed swirl generator and their appealing transition components in thermal applications.

1.7 Research Hypothesis

When the lobed swirl generator is placed at the entrance of the tube of a heat exchanger, the heat transfer will significantly be enhanced as the acceptable pressure drops occur, leading to a reduction of power consumption because:

1- The feature of the lobed swirl generator is represented in its ability to produce swirl flow adjacent to the wall and axial velocity concentrated on the core (Hangi et al., 2022). Due to the considerable effect of the lobed swirl angle (Jafari et al., 2017b), it is expected the angle deviation, together with a high Reynolds number (Li et al., 2015), led to improved swirl fluctuation and then enhanced heat transfer.

2- A lobed swirl generator can be divided into three vital parts: (i) entry transition part, which is gradually changed from circular shape to lobed cross-section. The circular shape is connected to the entry section, and the lobed shape is placed at the entrance of the lobed device. (ii) lobed swirl device is designed as a constant geometry swirl pipe (no gradual changes in its cross-section). It is placed between transition parts. (iii) The exit transition part forms gradually from a lobed shape to a circular cross-section. The lobed shape is fixed at the end of the lobed swirl device, and its circular shape is placed at the entrance of the test section, which is a circular, straight tube. According to research by Ariyaratne and Jones (2007), the gradual change of entry and exit led to improved swirl intensity and decreased pressure loss within the circular, straight tube. Also, the transition parts have two beneficial parameters:

transition multiplier (n), which leads to control of the intermediate area of the transition part and variable helix (t), which can decrease or increase the transition helix as desired. Therefore, using the transition parts under different parameters is expected to promote the system's thermal performance.

3- Incorporating nanoparticles of highly thermally conductive into conventional liquids increases their overall thermal conductivity (Younes et al., 2022). Therefore, its expected employment of nanofluid and a lobed swirl generator results in high heat transfer improvement and thermal performance.

1.8 Research Scope

The scope and limitation of the current study are related to examining the characteristics of swirling flow induced by LSG over the smooth channel. This study was conducted under different geometrical parameters using nanofluid and hybrid nanofluid as follows;

1- The study considers lobed swirl generators at various twisted angles to investigate their impact on heat transfer under different swirl flows.

2- Jafari et al., (2017b) examined the impact of a 4-lobed swirl generator under different angles from (90^o to 360^o) on thermal performance, and Li et al.,(2015b) studied the effect of different twisted angles of (360^o and 540^o) on Clean-In-Place procedures. Therefore, the current study aimed to investigate the lobed swirl generator under different twisted angles from (360^o to 450^o) on thermal performance. Moreover, other studies proved that the effectiveness of lobed swirl generators was achieved at short lengths of 0.2 m (Jafari, Dabiri, et al., 2017; G. Li et al., 2015b) and pitch to a diameter of 8 as optimum design (Ganeshalingam, 2002; Yan et al., 2020) based on the length of 0.4 m (with transition parts), twisted angle of 360 degrees and tube diameter of 0.5 m. Therefore, the current study employed the lobed twisted length at 0.4 m (with transition parts). Regarding the lobed number, the adoption of 4-lobed is based on the studies (Jafari, Dabiri, et al., 2017; Jafari, Farhadi, et al., 2017b, 2017a) and the comparison between a different lobed number (3, 4, 5, 6, 8, 9, 10 lobed) conducted by Yan et al.,(2020) and a comparison study performed by Ganeshalingam (2002), which all proved that the 4-lobed swirl generators were more efficient than all of the lobed numbers investigated. The following advantages motivate the use of water as a working fluid (Pifre, 2017): (i) suitable heat transfer fluid, (ii) low viscosity, (iii) high thermal capacity, and (iv) cheaper to use.

3- A comparison between beta transition (β) and alpha transition (α) was undertaken by Chanchala Ariyaratne (2005b). The study revealed that the β-transition is more efficient than α- transition by the value of 5%; as a result, β-transition was adopted in the present study. The transition parts can reduce the pressure loss, improve the overall swirl intensity, and reduce the swirl decay (C. Ariyaratne & Jones, 2007). Therefore, the same length of 0.1 m has been employed in the current study. There are two practical factors related to the transition parts. The transition multiplier (n) controls the intermediate area of transition parts at the n-value. The other parameter, known as a variable helix (t), leads to a decrease or increase in the transition helix as desired. Therefore, examining transition parts at different transition multipliers of (n = 0.25, 0.5, 0.75 mm) and the variable helix (t = 0.5, 1, 1.5 mm) was also the target outcome behind this study.

4- Li et al., (2015b) proved that the lobed swirl generator is more efficient with a high Reynolds number; as a result, a Reynolds number between 15,000 and 55,000 was used in the present study.

5- Applicable shear-stress transport (SST) k-ω model was used to model the turbulence swirling flow and the pressure adverse (Huang et al., 2022). SiO_2, Al_2O_3, and CuO nanofluids with volume concentrations ranging from 1 to 5% have been used to enhance heat transfer and improve water's thermal conductivity.

6- Considering their affective properties, the base fluid and nanoparticles were modelled as a single phase. The mixture assumes a homogeneous and has the same temperature and velocity field (Göktepe et al., 2014).

7- Due to the superior thermal properties of hybrid nanofluids over mono nanofluids (Babar, 2019) and the advantage of CuO of high thermal conductivity, low cost and better compatibility with basic liquids (Guangbin et al., 2016), also the advantages of GO of (i) higher thermal conductivity, (ii) a greater surface area to volume ratio, (iii) a reduced need for pumping power, (iv) improved stability, (v) reduced corrosion and (vi) significant energy savings (Alhakeem, 2022), A hybrid nanofluid of GO-CuO at different volume concentration of (0.15% to 0.75%) has been adopted in the current study.

1.9 The Layout of the Thesis

The thesis outlines are divided into the following five chapters:

The first chapter introduces the fundamental background, ideas, problem statement, principal objectives, research methods, and novelty of the study. The second chapter presents a literature review that is divided into four sections. The first section is related to the fundamental concept of heat transfer. The second section deals with the fundamentals of computational fluid dynamics. The third section expresses convective heat transfer over swirl flow. The fourth section provides the fundamentals of nanofluids. The third chapter explains the physical model of current geometry; the numerical approach includes (meshing, modelling, governing equation, boundary condition, grid-independent test, and validation of numerical study), and the experimental approach includes measurement instruments and hybrid nanofluid preparation. The fourth chapter extensively discusses the numerical and experimental outcomes. The last chapter discusses the conclusion of the study and presents a recommended proposal for future work of lobed swirl generators in thermal application.

CHAPTER 2

LITERATURE REVIEW

2.1 Overview

Understanding the flow and fluid characteristics is highly required to determine system parameters and the scope of this study. The circulation of fluids via pipes is essential in many thermal application sectors, including heat exchangers, cooling systems, chemical techniques, vehicles, and environmental systems. The swirl flow is a helical or spiral flow formed due to swirl flow induced near the wall surface and the axial velocity concentrated at the core through a smooth channel. The conveyance of fluids through a pipe requires an evaluation of pressure drops, pumping power, and flow rates (George, 2008).

2.2 Fundamental Concept in Heat Transfer

The fundamental study of heat and mass transfer addresses the rate at which thermal energy is transferred. The movement of heat from one substance or material to another is known as heat transfer (McEligoi, 1970). Heat transfer occurs when a different temperature between two adjacent substances takes place. As a result, heat travelled from high to low temperatures until the material's temperature differences were zero. Applications for heat transmission vary considerably and involve biological systems, typical home appliances, residential and commercial structures, industrial operations, electronic gadgets, and food preparation (Annaratone, 2010). Radiation, convection, and conduction are three primary mechanisms in heat transmission. Convection requires fluid mobility, whereas conduction demands to take place with a material medium.

2.2.1 Heat Transfer by Conduction

It is defined by the heat transfer within the solid medium due to close contact between the atoms or the molecules of the substance. Thermal energy is transferred from a region with higher kinetic energy to an area with lower kinetic energy. When slow-moving particles collide with fast-moving particles, the slower-moving particles gain more kinetic energy (Çengel & Cimbala, 2010). This is a typical type of heat transmission that occurs through physical contact. Conduction is also known as thermal or heat conduction. The following equation can be used to calculate the heat transfer rate by conduction, which is called Fourier's law of heat conduction.

$$q_{cond} = -K\frac{dT}{dx} \tag{1}$$

K refers to the thermal conductivity, and the reason behind the negative is that the heat transfer rate (q) is in the negative direction of the temperature gradient. Therefore, heat transfer is caused by going from a higher to a lower temperature. dT is the temperature gradient, and dx is the thickness.

2.2.2 Heat Transfer by Convection

Convection transfers heat through the bulk movement of molecules in fluids, including gases and liquids. Conduction is responsible for the initial heat transmission between the item and the fluid, while bulk heat transfer is caused by the rate at which the fluid moves (Çengel & Cimbala, 2010). The following formula can be employed to determine the rate of convection, which is expressed by Newton's law of cooling;

$$q_{cond} = hA(Ts - T_\infty) \quad (2)$$

Where h represents the heat transfer coefficient and Ts, Too refers to the surface's and surroundings' temperatures, respectively.

2.2.3 Heat Transfer by Radiation

In most of our lives, radiant heat is indispensable to everyday life. Radiant heat is the term used to describe thermal radiation. Electromagnetic wave emission is the source of thermal radiation. These waves take out the energy from the body that is emitting. Radiation is transmitted via a transparent, solid, or liquid medium in a vacuum. The heat transfer by radiation occurs due to the random movement of the molecules within matter. The movement of energized protons and electrons creates electromagnetic radiation. The Stefan-Boltzmann law can be utilized for determining thermal radiation:

$$q_{radation} = \varepsilon\sigma A(T_s^4 - T_{sur}^4) \quad (3)$$

Where Ts and Tsur are the temperature of the surface and the temperature of the surroundings, due to the temperature being exponential in the fourth, the temperature always has to be in Kelvin. Also, the ε and σ refer to the emissivity and Dtefan-Blatzman constant, respectively.

2.2.4 Nusselt Number

Wilhelm Nusselt developed the concept of the Nusselt number between 1909 and 1915 to describe the heat flow at a wall or solid surface (Çengel & Cimbala, 2010). In convective heat transfer studies, the Nusselt number is a dimensionless value. The Nusselt number is defined as the ratio between the heat transfer by convection ($\dot{q}_{conv.}$) To the heat transfer by the conduction ($\dot{q}_{cond.}$) and it is evaluated as the following:

$$N_u = \frac{Convection\ Heat\ Transfer}{Conduction\ Heat\ Transfer} = \frac{\dot{q}_{conv.}}{\dot{q}_{cond.}} \tag{4}$$

By substituting equations 1 and 2 for equation 4, the actual formula of the Nusselt number can be determined as follows:

$$N_u = \frac{\dot{q}_{conv.}}{\dot{q}_{cond.}} = \frac{h\Delta T}{k \times \frac{\Delta T}{L}} = \frac{hL}{k} \tag{5}$$

From the formula, it can be concluded that the Nusselt number explains how the characteristics of heat are transferred. For further clarification, A higher Nusselt number refers to the heat transferred by the convective force. In contrast, the low Nusselt number value is inducted to the heat transfer by conduction instead of convection (Iyer et al., 2022). That is the Nusselt number, and it is the most basic.

2.2.5 Reynolds Number

Osborne Reynolds 1903 innovated the dimensionless formula Known as (the Reynolds number), which describes the changes in the flow under turbulent or laminar flow. Severe geometric cross-sections lead to slight differences in Reynolds number value in the same conditions (Ahmadi et al., 2022). Thus, turbulent flow results from high Reynolds numbers, and laminar smooth flow results from low Reynolds numbers.

$$Re = \frac{Inertial\ Force}{Viscose\ Force} = \frac{\rho \nu L}{\mu} \tag{6}$$

L = Traveled length /Diameter of system

ρ = Density of fluid (Kg/m3)

ν = Velocity of the fluid (m/s)

μ = viscosity (Kg/m. s)

The Reynolds number for flow in a round tube can be expressed as

$$Re = \frac{V_{avg} D}{\upsilon} = \frac{\rho V_{avg} D}{\mu} = \frac{\rho D}{\mu}\left(\frac{\dot{m}}{\rho \pi D^2/4}\right) \tag{7}$$

D is the tube's diameter, ν = μ/ρ is the fluid's kinematic viscosity, and Vavg is the average flow velocity.

It can determine the Reynolds number by the ratio between the inertial and viscous forces. The motion force of the liquid can be induced through the different geometrical cross-sections. Consequently, the motion resembles the fluid's momentum and the interactions between its molecules and sides, which can be attributed to the inertial force. Conversely, the viscous force would be the attempt to slow the flow down (Agarwal et al., 2024). The velocity (ν) is one of the most significant parameters influencing the flow pattern. If the velocity is indicated at a substantial value, the augmentation of inertial force takes place. As a result, higher Reynolds numbers are associated with a more significant potential for turbulent flow.

Moreover, the characteristic length, hydraulic diameter, and density (ρ)of the working fluid are essential parameters that directly affect the flow pattern. Depending upon the geometry, If the range of Reynolds number indicated greater than 2000, the fluid is turbulent flow. The behaviour of the flow is laminar if the Reynolds number is less than 2000 (Gustenyov et al., 2023).

2.2.5.1 Turbulent and Laminar Flows

The distinction between turbulent and laminar flow is considered the most crucial theory in fluid mechanics. Significant variances in patterns between these two flow regimes result in different effects on global fluid flow. Therefore, laminar flow characteristics between the layers exhibit a smoothness pattern with slight fluctuation, as seen in Figure 2.1(a). In the case of gradually increasing the flow velocity, the flow pattern exhibits random motion; this is the beginning of the transition flow regimes, as seen in Figure 2.1(b). If the flow velocity is high, the flow regime changes from the transition region to the turbulent flow regime, as seen in Figure 2.1(c).

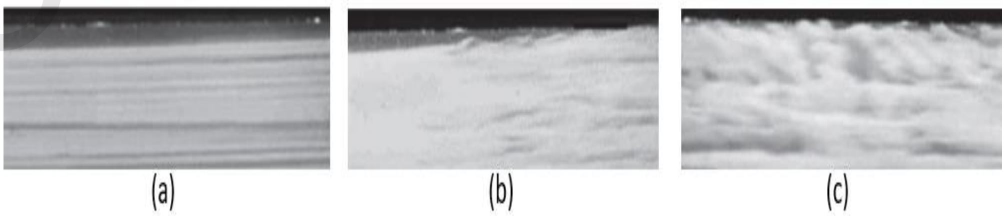

Figure 2.1: Flow regime at (a) Laminar, (b) Transition and (c) Turbulent flow (Çengel & Cimbala, 2010)

Chaotic movement and rotation regions, called eddies, are turbulent flow features (Hunt & Morrison, 2000). Different types of eddies will be created due to the significant mixing of the fluid. Figure 2.2 shows fluid characteristics under a smooth flow regime (Laminar flow could be easily analyzed since there are often no random changes in velocity). According to turbulent flow, the data on its characteristic behaviour is also depicted in Figure 2.2. This flow is much more complicated to analyse since it has more and more fluctuation and eddies. Therefore, the flow velocity in a turbulent regime is divided into two significant components known as fluctuating components $\acute{\mathcal{U}}(t)$ and time-averaged $\overline{\mathcal{U}}$.

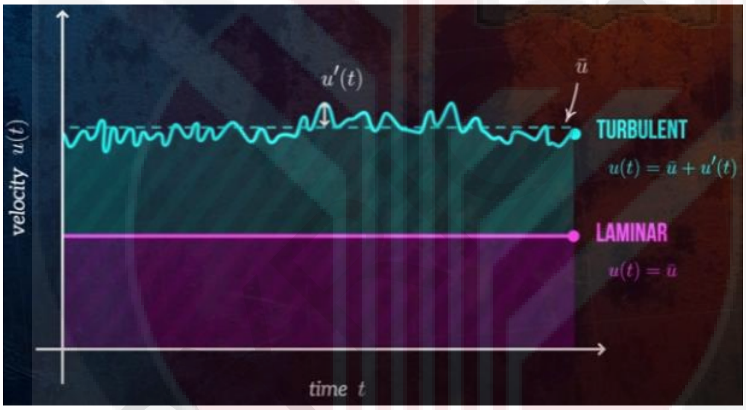

Figure 2.2: The difference between the smooth laminar and turbulent flow and fluctuating (Çengel & Cimbala, 2010)

Evaluating which flow regime is most likely to result from a given set of parameters is vital since laminar and turbulent flow are quite different and require different analyses. Therefore, the related parameters used by Osborne Reynolds in 1883 were considered. Reynolds conducted a great deal of testing to determine the factors that influenced the flow regime and developed the non-dimensional equation, which is used to estimate if the flow will be turbulent or laminar. The equation can be written depending on kinematic viscosity (υ) instead of dynamic viscosity (μ). According to the flow analysis type, a characteristic length (L) is considered. The hydraulic diameter is changed as the geometrical cross-section is considered. If the flow passes through the cylinder, the hydraulic diameter will be the cylinder diameter. It would be cord length for the airfoil and pipe diameter for the pipe cross-sections (Bérut et al., 2022). One of the importance of the Reynolds number is represented in its ability to describe inertial forces (ρvL) and viscous forces (μ). For more understanding, let's look at how the flow regime affects flow through circular pipe. The flow velocity at the pipe wall is always zero, known as the no-slip condition. For fully developed laminar flow, the velocity increases to reach the maximum velocity near the centre of the pipe, resulting in a parabolic velocity profile, as seen in Figure. 2.3.

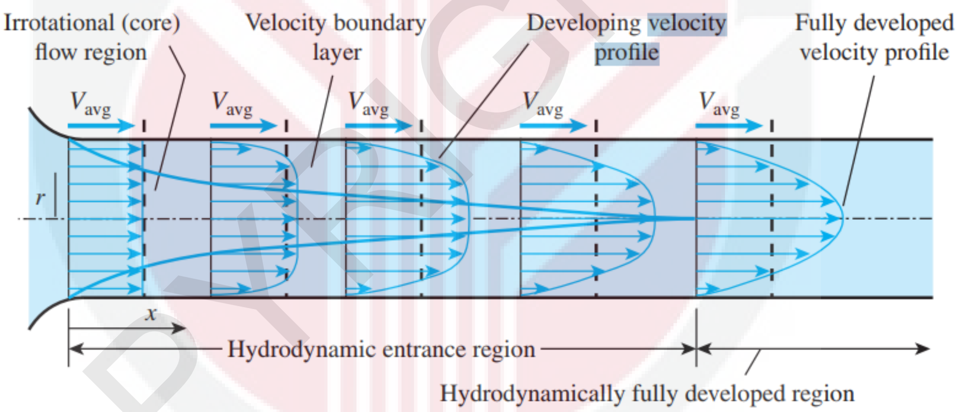

Figure 2.3: Velocity profile at laminar flow (Çengel & Cimbala, 2010)

2.2.5.2 Fully Developed Flow

The velocity profile changed to the axial direction shape at the pipe's entrance (entry region). The no-slip boundary condition, however, will cause the fluid velocity near the walls to be zero; as a result, the fluid layers next to the wall will decelerate due to shear stress from the velocity gradients. The outer layers of the velocity profile will be deformed as the fluid moves down the pipe because more and more layers will be affected by this shear stress (Reduction, 2024). At the core of the velocity profile, the velocity gradients are still small, and the velocity profile is relatively uniform. The boundary layer forms and expands in the axial direction. This boundary layer has considerable velocity gradients and significant shear stress. The core region is named (inviscid) because this region has negligible shear stress. After the flow continues travelling within the pipe, the developing shape begins to form, and the velocity profile changes in the axial direction. The flow is (fully developed) at the end of the entry area, where the boundary layer has expanded to enclose the whole flow. Shear stress is present throughout the entire velocity profile, as shown in Fig. 39. The developing region length, also known as the entry length (Le), is determined based on the pipe diameter (D) and Reynolds number flow regimes (Re). Equation (8) is considered to evaluate the laminar flow, while Eq. (9) is used for turbulent flow (Çengel & Cimbala, 2010) as the following;

$$L_e = 0.06DRe \tag{8}$$

$$L_e = 4.4D \times (Re)^{1/6} \tag{9}$$

2.2.5.3 Hydraulic Diameter

When considering flow in noncircular tubes and channels, the term "hydraulic diameter" (Dh) is frequently employed. The following equation is commonly used to determine hydraulic diameter;

$$D_h = \frac{4Af}{P} \tag{10}$$

Where Dh, Af, and P are the hydraulic diameter, flow area, and wetted perimeter, respectively. Hydraulic diameter is mainly used for calculations involving turbulent flow. The hydraulic diameter formula is highly dependent on the geometry structure, as seen in Figure 2.4.

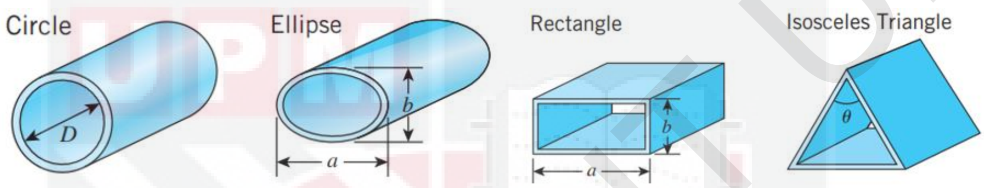

Figure 2.4: The hydraulic diameter at different geometries cross-sections (Çengel & Cimbala, 2010)

2.2.6 Differential Pressure

The pressure drop (ΔP) is an essential parameter in pipe flow analysis because it is directly connected to the power the pump or fan needs to maintain flow. Pressure drop in fluid flow is denoted by the symbol ΔP, P1 - P2. It can be evaluated using equation (11). An irreversible pressure loss is called pressure loss when viscous processes cause a decrease in pressure. ΔPL should stress that this is a loss. According to equation (12), there is a direct relation between the pressure drop and the fluid's viscosity, and the dP could be Zero if there is no friction effect. As a result, in this case, the pressure drop from P1 to P2 is mainly due to viscous impact. Equation (13) refers to the flow through the pipe. Pressure loss occurs at different effective flow viscosity μ, constant diameter D, tube length L and average velocity Vavg. For any fully developed internal flow, including laminar or turbulent flows, circular or noncircular pipes, smooth or rough surfaces, and horizontal or inclined pipes, it is practical to represent the pressure loss as depicted in Figure 2.5.

$$\frac{dp}{dx} = \frac{P_2 - P_1}{L} \tag{11}$$

$$Laminar\ flow: \quad \Delta P = P_1 - P_2 = \frac{P_2 - P_1}{L} = \frac{8\mu L V_{avg}}{R^2} = \frac{32\mu L V_{avg}}{D^2} \tag{12}$$

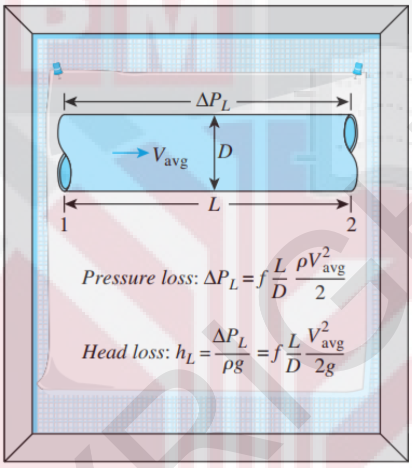

Figure 2.5: Pressure loss and head loss (Çengel & Cimbala, 2010)

$$Pressure\ loss \quad \Delta P_L = f\frac{L}{D}\frac{\rho V_{avg}^2}{2} \tag{13}$$

Where ρV2avg/2 represented dynamic pressure and f refers to Darcy friction factor.

In fluid mechanics, one of the most common relations is the one for pressure loss (and head loss), which is used for pipes with smooth or rough surfaces, laminar or turbulent flows, and circular or noncircular tubes. It is worth to mention there is a difference between the Fanning friction factor Cf and Darcy friction factor. Therefore Cf =

2τw/(ρV2avg) = f/4. When Equations 12 and 13 are set to be equal, the friction factor for fully developed laminar flow in a circular

tube could be found by solving for f as follows;

$$Circular\ tube\ laminar \qquad f = \frac{64\mu}{\rho D V_{avg}} = \frac{64}{Re} \tag{14}$$

The friction factor (f) for a fully developed turbulent flow with rough surfaces could be determined on the Moody chart or;

$$\frac{1}{\sqrt{f}} = -2.0log\left(\frac{\frac{\varepsilon}{D}}{3.7} + \frac{2.51}{Re\sqrt{f}}\right) \approx\ -1.8log\left[\frac{6.9}{Re} + \left(\frac{\varepsilon/D}{3.7}\right)^{1.11}\right] \tag{15}$$

The average height of the surface imperfections on the pipe surface is known as the absolute roughness. Roughness in the pipe restricts fluid flow. The symbol (ε) represents the absolute roughness and has length dimensions. Its values are displayed for various materials and are often given in (mm or inches). Using the following formula, one can then estimate the relative roughness of a pipe (DiPippo, 2016):

$$\varepsilon = \frac{absolute\ roughness}{pipe\ diameter\ D} \tag{16}$$

Depending on whether the flow is laminar or turbulent, the fanning friction factor could be determined once relative roughness and Reynolds numbers have been calculated (DiPippo, 2016). The resistance to flow causes a pressure decrease when fluid passes through a pipe. Additionally, a change in level between the pipe's start and end may result in a pressure gain or loss. Many of the characteristics are connected to this overall pressure differential across the pipe:

- friction that exists between the liquid and the pipe wall
- Friction inside the fluid itself between adjacent layers
- Friction loss as the fluid goes through any bends, valves, pipe fittings, or other parts
- Pressure loss because of the fluid's height changing (if the pipe is not horizontal)
- Pressure increases because of whatever extra fluid head a pump adds.

2.2.7 Performance Evaluation Criteria (PEC)

Webb RL (1994) is the first researcher to introduce the performance evaluation criterion (PEC). Several applications for single-phase heat exchangers use the performance assessment criteria covered in this chapter (Yin et al., 2023). The PEC formulas enable us to consider the thermal resistance of both fluid streams or make a straightforward surface performance comparison. The PEC analysis allows a designer to rapidly identify the most efficient surfaces or tube inserts. The designer can evaluate the effectiveness of practical heat exchangers by using the criterion equations, which consider external thermal resistances and variations in temperature differential along the flow route (Al-asadi, 2018). It is possible to create a performance evaluation criterion (PEC) index that considers changes in fluid flow impacts and heat transfer performance changes to assess the benefit reuse cost of a proposed cooling system improvement (Webb, 1981; Zhang et al., 2014). Nusselt number or thermal resistance could be used as the heat transfer term, while friction factor or pressure drops can be used as the fluid flow concept. The effectiveness of the system's overall improvement could be assessed using the performance evaluation technique.

Additionally, the formula, which is represented in the equation below, might be used to compare simple and sophisticated designs, including smooth and modified micro-channels, to assess the effectiveness of changing the geometry (M. A. Ahmed et al., 2014; Manca et al., 2012). If the value of PEC is greater than 1, the heat transfer improvement is higher than the friction factor and vice versa. If the PEC is more prominent than one, it reveals that the improvement in heat transfer is more significant than the effect of the friction factor (Hilo et al., 2020a).

$$PEC = \frac{(Nu/Nu_p)}{(f/f_p)^{1/3}} \tag{17}$$

2.3 Fundamental of Computational Fluid Dynamics

2.3.1 Overview

CFD is a numerical technique using computer simulations to address fluid problems (Laurens et al., 2023). CFD is a type of numerical analysis, an abbreviation for computational fluid dynamics, and it is used to study all kinds of fluids and gases. A distribution of the velocity vector field can be obtained from the solution. Different characteristics of the fluid can be analysed. For example, the distribution of the velocity in the system through which it passes and the difference in the distribution of speeds. Another property that can be studied using the CFD analysis approach is the distribution of associated pressure.

Moreover, the temperature distribution characteristics within any system can be analysed using CFD. Also, CFD simulation can be used to study the interactions between the solid body and the fluid, such as the interaction of ship propellers inside the water. The gases and the compressible or incompressible liquids can be investigated using CFD simulation. The study of systems involving fluid flow, heat transport, and related variables, including chemical reactions using computer simulation, is known as computational fluid dynamics (CFD) (A. Sharma, 2021). The method is efficient and has many industrial and non-industrial uses, including in power, electrical, cars, aerospace, defence and civil engineering (Hermansen, 2021). The current chapter aims to provide a detailed literature review on the impact of lobed swirl generators under different influential parameters on heat transfer and fluid flow. Therefore, the literature review focuses on the most important influential factors, such as the Reynolds number, friction factor and Nusselt number. The effectiveness of geometrical cross-section parameters such as Lobed number, twisted angle, and twisted length has also been presented in detail.

2.3.2 Governing Equations of Fluid Dynamics

The governing equations for fluid flow in computational fluid dynamics (CFD) are obtained by applying the basic principles of mechanics to a fluid flow, including turbulent ones. These equations serve as mathematical expressions for the conservation laws of physics (Mani & Dorgan, 2023). The dynamical equation "Navier-Stokes " is a descriptive term attributed to the formulas determining fluid flow. The continuity equation, momentum equation, and energy equation are the partial differential equations that represent the three fundamental concepts (Kausar et al., 2023).

2.3.3 Advantages of Numerical Analysis Over Experimental

The computational fluid dynamics (CFD) approach has several features compared with an experimental method, such as saving time, reducing design costs and offering the capacity to investigate systems where performing controlled experiments is impossible or difficult to achieve (Li et al., 2019). There are several benefits of the CFD over the experimental approach: (1) the ability to visualize things that an experiment study cannot, (2) Risk-free analysis of hazardous configurations, such as a combustion chamber or nuclear reactor, etc., (3) CFD approach is less costly compared with an experimental method and (4) Design optimisation potential (automated parametric research). In general, the CFD approach and experimental are complementary to each other. The most crucial advantage of CFD over experimental study is that the solver can present the solution in parallel (Lange et al., 2021), while in the case of the experimental approach, it goes sequentially. Finally, the traditional solution is challenging to apply when conducting any design or physical study and writing the related equations. Therefore, the numerical analysis technique is considered to overcome this problem as an optimal alternative (Moin, 2016).

2.3.4 Mathematical Model

The correct steps toward the CFD simulation procedure are significant in obtaining acceptable results (Q. Chen & Ph, 2002). Therefore, the first step is to build the mathematical model, which is defined as a set of differential equations that represent the characteristics of the physical model and boundary condition of the system that we want to study known solvers (Vasta, 2014). The flow would be investigated under different assumptions such as compressible or incompressible, inviscid or viscous, turbulent or laminar, and the model is 3-D or 2-D.

2.3.5 Discretization Method

Discretization translates continuous equations, models, variables, and functions into discrete equivalents in practical mathematics. Usually, this procedure is used as a preliminary step to prepare them for numerical analysis and digital computer application (Yuan & Zhu, 2023). It can divide the discretization method into discretizing the mathematical model and the geometry.

2.3.5.1 Discretizing the Mathematical Model

It means converting the mathematical model into a language that the computer can understand and deal with. In other words, converting partial differential equations into algebraic equations that a computer can handle. For performing this method, there are several methods Finite Difference Method (FDM), Finite Volume Method (FVM), Finite element Method (FEM), Spectral method, Boundary element method (BEM) and Discrete Particle Method (DPM). FDM, FVM and FEM, known as the big three, are considered the three most important methods through which we can, in numerical analysis processes, transform the mathematical models PDEs that describe a specific physical state into a set of algebraic equations that the computer could be solved (Oz et al., 2023).

2.3.5.2 Discretizing the Geometry

The space in which the simulation (boundary condition) should be divided into many points (nodes), or in other words, a mesh should be constructed (Reza et al., 2023). Construct a mesh, grid, or particle system that specifies the shape and includes the critical fluid interactions you wish to investigate. The mesh we need to construct should be fine enough to solve the problem we must explore accurately. The solution should be obtained at each node of the mesh. In other words, every node in this mesh will provide a solution for a particular variable, such as temperature, pressure, or speed, which have all been defined beforehand.

2.3.6 Numerical Scheme Analysis

The control-volume-based method used in ANSYS FLUENT to solve the governing integral equations for the conservation of mass, momentum, energy, and other scalars like turbulence and chemical species involves the following steps (G. Li, 2016): (i) Employing a computational grid, divide the domain area to discreet control volumes, (ii) To create algebraic equations for the specific dependent variables such as velocities, pressure, temperature, the governing equations are integrated into each control volume and (iii) The structured equations are linearized. The consequent linear equation structure is solved to obtain new values for the dependent variables. For the numerical scheme to be acceptable, it should satisfy several conditions, including consistency, stability, convergence, and accuracy (Hirsch, 2007).

2.3.7 Solver

Pressure-based solvers or density-based solvers are the two main numerical methods available within Ansys Fluent that give the user a choice to solve a fluid flow. Typically, incompressible or slightly compressible flows have been solved using the pressure-based solution. Typically, incompressible or slightly compressible flows could be solved using the pressure-based solution. Over pressure-based solvers, density-based solvers presented better and more accurate results for the compressible flow at high speed.

In ANSYS FLUENT, the pressure-based solver has two algorithms: segregated and coupled. The governing equations in the segregated method are solved sequentially and separately (Aksoz et al., 2024). In contrast, the momentum and pressure-based continuity equations are solved simultaneously in a coupled manner. Compared with each other, the coupled algorithm considerably converges at a speed greater than a segregated algorithm. Nevertheless, the coupled algorithm requires more memory than the segregated approach, as seen in Figure 2.6.

A density-based solver can solve the governing and species transport equations simultaneously. The equations are modified to develop compressible and incompressible fluid flows. Time is a critical factor in density-based solvers, whether they are transient or steady state. Both time and spatial coordinates are used to distinguish between variables. Second-order iteration is used to solve the set of equations simultaneously. Density-based solvers are employed for incompressible flows (supersonic flows with much more significant than 1.5). Figure 2.7 depicts an algorithm for a density-based solver.

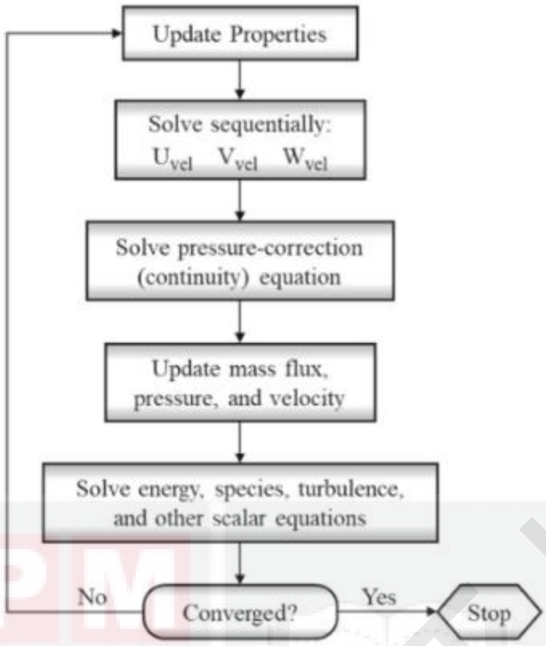

Figure 2.6: The general steps of a pressure-based solver (segregated algorithm) (Aksoz et al., 2024)

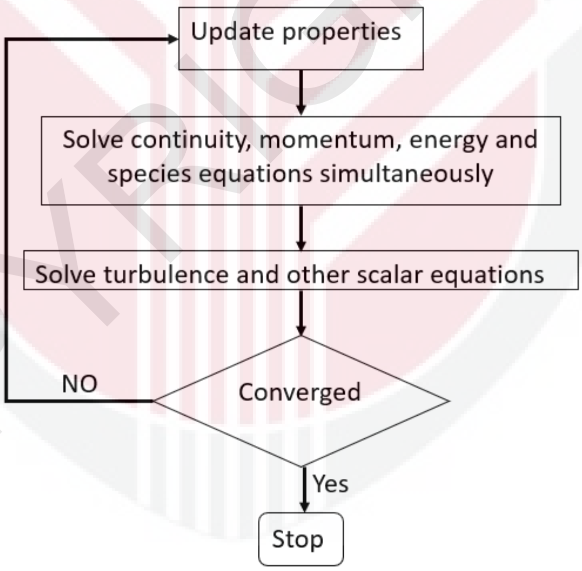

Figure 2.7: The general steps of a density-based solver (Karakoyun et al., 2021)

2.3.8 CFD Post-processing

Analysing and displaying the numerical data produced by the numerical simulation is known as CFD post-processing, and it is a crucial stage in the computational fluid dynamics (CFD) simulation process. Engineers and scientists could employ it to learn more about how fluid flows behave and use the simulation findings to guide their decisions. For CFD. Any method of interacting with and analysing the simulation findings is called "post-processing." FLUENT Post Processing tools and tools built within the FLUENT solver are the two methods available for post-processing CFD results from FLUENT. Both postprocessors include many tools for analysing CFD results, including surfaces, vector plots, contour plots (shaded and graded), streamlines and path lines, XY plotting and animation creation. With FLUENT's built-in tools, you can rapidly investigate your simulation. Since the solver still has access to all the data in memory, you can quickly analyze the findings and then make changes or carry out more computations without waiting for the file to be written or read to utilize another program.

2.4 Convective Heat Transfer in Swirl Flow

Numerous studies have examined convection heat transfer experimentally and numerically over turbulent and laminar flow domains with various boundary conditions, fluid characteristics, and geometrical cross-section parameters.

2.4.1 Convective Flow with a Propeller-type Swirl

The most common swirl generators widely employed to create swirling flow within straight tubes are propeller-type devices, including rotating axial turbine-type, helical-twisting shapes, twisting blades, guide vanes, curved conical coils, and spiral wires or blades placed at the pipe inlet. Hangi et al., (2022) installed an axial-turbine-type device in a circular tube to increase convective heat transmission. The swirl is free-rotating and fabricated with different blades. The result demonstrated that the axial-turbine-type swirl generators significantly improved convective heat transfer and thermal performance by about 75% and 1.4, respectively. The impact of the swirl generator induced by different radial guide vanes on heat transfer and friction factor was carried out by Yilmaz et al., (2003). The result showed that the swirl generator without reflection presented the highest heat transfer of 150% with the highest pressure drop.

Sun et al., (2018) studied numerically the effect of a swirl generator equipped with a circular tube on heat transfer and flow fields. The swirl was examined at the different angles (θ = 25º, 45º and 60º), the length (l = 0.005, 0.01, and 0.02 m) and the centre rod radius (1, 2, and 3 mm). The study is performed for various Reynolds numbers in the range of 300 – 1,500. The results concluded that the ideal swirl generator could be provided at the most significant angle of 60, the largest lobe radius of 3, and the shortest length of 0.005 m.

Bilen et al., (2022) investigated numerically and experimentally the effect of a swirl generator mounted at the entrance of a circular pipe on heat transfer and flow characteristics. The swirl examined at a different twisted angle of (θ = 0, 22.5º, 41ºand 50º), under constant heat flux, with the Reynolds number of 2,400 – 23,000. The outcome exhibited that the increase in twisted angle and Reynolds number led to increased heat transfer. Moreover, the result displayed an enhancement in Nusselt number around 1.1–1.41 times, while the friction factor was 2.3–6.76 times. An experimental investigation is conducted to inquire about the pressure drop and heat transfer properties of swirl flow through a horizontal pipe (Saraç & Bali, 2007). The swirl was studied at a different angle of (θ = 15º, 30º, 45º and 60º) position length of (x = 0, = L/4 and L/2) with a Reynolds number of 5,000 – 30,000. The Nusselt numbers were found to exhibit improvements in the range of 18.1% to 163% based on the position of the angle and number of vanes as well as the value of the Reynolds number.

2.4.2 Convective Flow with Tube Inserts

Chaurasia & Sarviya (2019) studied experimentally the impact of inserting double-strip helical screw tape inserts in a circular tube. The study considered the twist ratio (1.5, 2.5, and 3) with Reynolds numbers varying from 4,000 to 16,000 under uniform heat flux. The result proved that the increase in twisted ratio and Reynolds numbers led to increased heat transfer, friction factor and system thermal performance. Yongji Wang et al., (2022) investigated numerically the effect of thermal-hydraulic of a symmetrical wing longitudinal swirl generator inserted in the tube on heat transfer at laminar flow. The proposed device at different geometrical parameter effects of inclined angle, face angle, wing angle and pitch was performed. The outcome presented increased heat transfer ratio, friction factor ratio and thermal performance at 5.00 - 10.22, 4.05 - 14.20, and 0.71 - 1.35, respectively, compared with plane tubes.

Goh et al., (2021) proposed a rotating tubular insert technique to promote heat transfer within the heat exchanger tube. The result stated that the Nusselt number considerably increased by 360% and 240% in non-rotating (fixed blade) and free-rotating cases compared with plane tubes. The result also pointed out the significant increase in pressure drop associated with all cases studied. S. Kumar et al., (2019) studied the impact of helical tape insert via circular tube on the heat transfer and flow characteristics. The helical tape was evaluated at various width ratio (WR) and twist ratio (TR) cross-sections. The numerical analysis is carried out at a Reynolds number between 1,000 - 25,000. The result reported that the increase in width ratio with the twist ratio led to an increase in Nusselt number by 119% with a Reynolds number of 25,000. From the side of the friction factor, the study demonstrated that the friction factor is 133% higher than the plane tube.

D. Kumar et al., (2020) presented a novel experimental study on improved heat transfer and fluid flow over a circular tube by inserting a perforated ring with deflector-lanced holes. The study was carried out at many efficient parameters of the pitch to diameter (P/D = 3.33, 5 and 6.66), diameter ratio (d/D = 0.5, 0.545 and 0.6), number of lanced holes (n = 4,6 and 8) and air as the working fluid generated at different Reynolds number ranging from 10,000 - 37,754. The outcome pointed out that the highest heat transfer and friction factors were found to be at 4.1 and 72, respectively, associated with lanced hole number, pitch to diameter, and diameter ratio of 8, 0.5, and 3.33. It can be explained by the characteristics of the lanced holes, which led to the squeezing of the flow within the hole and creating a swirl flow pattern.

2.4.3 Convective Flow Over Curve Channel

The heat transfer and flow properties of twisted tubes under different cross-sections at Reynolds numbers ranging from 50 to 2000 are investigated numerically by Cheng et al., (2019). The test section is a twisted square tube examined under constant wall temperature. The result showed increased heat transfer and pressure drop with the twisted tube compared with the plane tube. Sahel et al., (2020) presented a numerical study on the effect of different shapes (circular, elliptic, oval tube RO, oval tube LO, and flat) on heat transfer over the heat exchanger. The domain is a turbulent external airflow with a Reynolds number of 3,000 to 20,000. The results indicate that the circular-shaped tube has the highest heat transmission rate compared to other options.

Nonetheless, the elliptical pipe has the lowest pressure losses compared to the different shapes. Compared to the flat tube, the circular, oval RO, oval LO, and elliptical tubes have a heat transmission coefficient of around 18, 12, 10, and 4%, respectively.

A comparison of the impact of the smooth and micro-fin of helical coil tubes on heat transfer and fluid flow characteristics has been reported by Kumar (2021). Moreover, the crucial effectual parameters of coil diameter (100 - 200 mm), coil pitch (25 - 45 mm) and Reynolds number from (10,000 - 25,000) are taken into consideration. The result revealed that the micro-fin helical coiled tube presented heat transfer and pressure drop of 51% and 36%, respectively, compared with the smooth helical coiled tube. The increase in surface area of the micro-fin helical coiled tube can explain this. Under the laminar and turbulent flow, a type of spiral coil has been scrutinized for its effect on heat transfer and fluid characteristics by Patil (2019). The investigation used several practical factors, such as curvature and pitch-to-diameter ratios. The result demonstrated that the increase in curvature ratio led to an increase in heat transfer while the pitch-to-diameter factor has the inverse proportional effect on heat transfer.

Alempour et al., (2020) evaluated numerically the impact of the aspect ratio (AR= 1.65 and 1.27) of an ellipse and the twisting pitch (λ = 0.1, 0.2, 0.3 and 0.4 m) on the heat transfer and fluid flow characteristics. The result indicated that the heat transfer increased by 5% with an elliptic ratio of 1.65 and a twisted pitch of 0.4, as seen in Figure 2.8. At the exact value of elliptic ratio but with a reduction of the twisted pitch to 0.2, the heat transfer increased by 20% compared with a plain tube. Further, decreasing the twisted pitch from 0.2 - 0.1 m increased the heat transfer to 30%. It is worth mentioning that the reduction in twisted pitch led to a considerable increase in friction factor by 128%. It is attributed to the rise in distortions within the tube, leading to significant recirculation of the swirl flow.

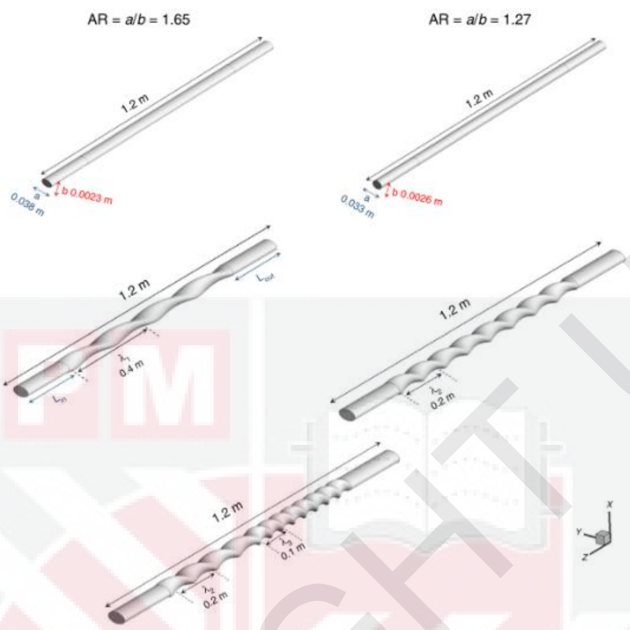

Figure 2.8: Twisted elliptic cross-section at different aspect ratios of 1.65 and 1.27 (Alempour et al., 2020)

2.4.4 Convective Flow Over Lobed Swirl

Jafari et al., (2017) examine experimentally and numerically the impact of the three-lobed swirl generator at twisted angles ranging from 90º to 360º and varied lengths ranging from 0.2 to 0.4 m on thermal performance, as shown in Figure 2.9. An inverse proportion exists between the twisted angle of θ = 90 and the increase in twisted length. The twisted length of ꞁ =1 with the twisted angle of θ =90 is indicated as the highest heat transfer. At the twisted angle of θ = 180, the better heat transfer rate is displayed at the twisted length of ꞁ = 2. In the case of a twisted angle of θ =270, the highest heat rate was recorded at the twisted length of ꞁ = 3. Among all the parameters investigated, a twisted angle at θ = 360 with a twisted length of θ = 4 presented the highest heat transfer rate. The outcome indicated that the heat transfer improved from 1.34 to 1.74, and the thermal performance increased from 1.25–1.55.

At a constant length of 0.4 m but with different twisted angles of (90º, 180º, 270º and 360º) Jafari et al., (2017b) investigated the effect of a four-lobe swirl generator on heat transfer and thermal performance, as seen in Figure 2.10. At the variety of Reynolds numbers range 6000–30,000, the Nusselt number ratio *Nu*/*Nup* and the friction factor ratio *f/fp* were studied to investigate the impact of swirl generator at different twisted angles. In all cases studied, the Nusselt number ratio and friction factor ratio indicated values of 1.4–1.9 and 1.22 and 1.48, respectively. The thermal performance of the system is 1.30 to 1.65. The numerical result proved the swirl generator's ability to create high circulation flow adjacent to the tube's wall and concentrate axial velocity at the centre. These findings have been described as the primary causes for improved thermal performance. Compared with the three-lobe, the result showed remarkable enhancement in heat transfer and thermal performance by the factor from (1.39 to1.87) and (1.30 to 1.65), respectively. At the same twisted angle and twisted length, the five-lobe swirl generator has been investigated by Jafari et al., (2017a). The result demonstrated that heat transfer and thermal performance improved from (1.37 to 1.84) and (1.24 to 1.60), respectively.

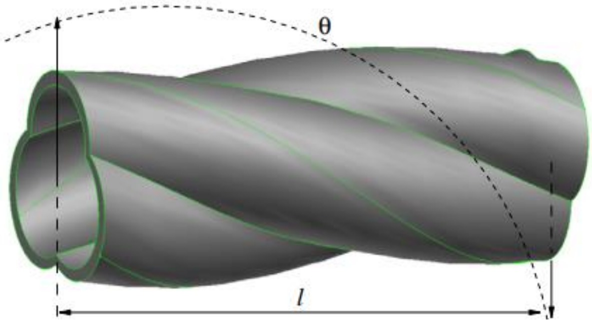

Figure 2.9: Three-lobed cross-section (Jafari, Dabiri, et al., 2017)

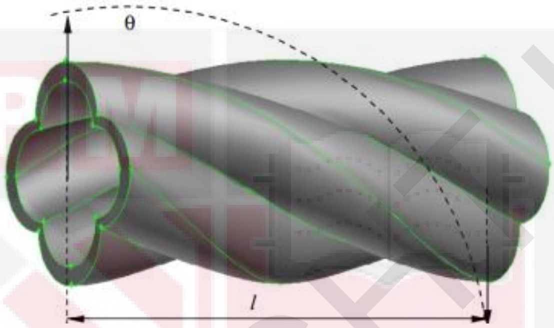

Figure 2.10: Four-lobed cross-section (Jafari et al., 2017b)

Omidi et al., (2018) presented a study on the impact of helical coil tubes formed with different lobed cross-sections on heat transfer and fluid flow characteristics. The water is a working fluid flowing in a laminar regime ranging from 1300 to 2500. The test section was subjected to constant temperature. Further, the study was undertaken under various geometrical parameters such as pitch, height, and coil diameter, as shown in Figure 2.11(a). The lobed number at (n = 3, 4, 5 and 6) as a crucial factor has been considered in this study, as shown in Figure 2.11(b).

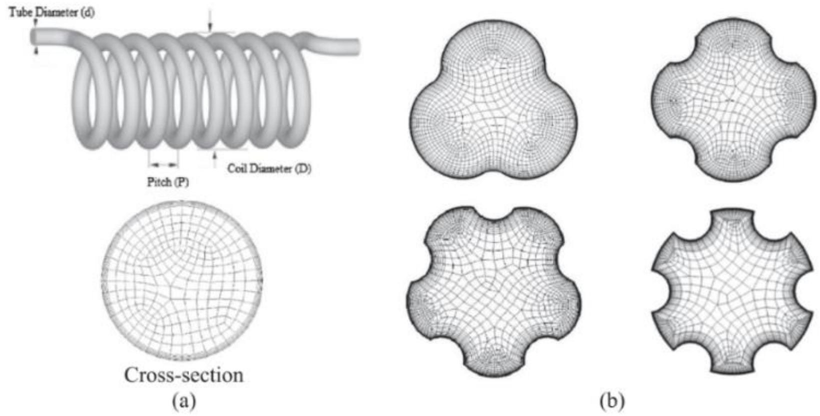

Figure 2.11: Helical coil tubes. (a) physical model and circular cross-section, (b) different lobed cross-sections (Omidi et al., 2018)

Regarding the effect of the lobed number, the result demonstrated that the increase in lobed number led to an increase in thermal performance. The lobed number of (n = 6) presented the highest PEC due to the reduction in pressure drop. In the case of the impact of coil height and the pitch, the result showed no change in flow characteristics because it fully developed. The result proved that the coil diameter has an inverse inverse-proportional relationship with the Nusselt number and friction factor.

A comparison between a twisted tri-lobed tube and a twisted oval tube on the impact of heat transfer and turbulent flow was experimentally and numerically conducted by Tang et al., (2015a). The geometric cross-sections investigated are smooth round tube, twisted oval tube and twisted tri-lobed tube, as seen in Figure 2.12. The study was appraised at a Reynolds number ranging from 8000 to 21000. The impact of different lobed cross-sections on heat transfer improvement has been studied. All cases have been examined under the effect of the factors of major (a) and minor(b) of elliptical parts of the tube and diameter of inscribed (D1) and out-scribed (D2) circle of the tube and the radius of arc part of the tube (r). Moreover, the other four cases were investigated based on the effect of pitch to diameter (Pt = P/D) of 2.5, 5.0,7.5 and 12.5.

Also, the study focused on the impact of twisted direction from the Right/Left (R-L) direction and vice versa. The result demonstrated that the twisted tri-lobed presented 5.4% and 8.4% enhancement of Nusselt number and friction factor, respectively, more than an oval tube. From the perspective of the effect of different shapes, the result proved that case three at smaller D1 and r presented the highest heat transfer and friction factor due to an increase in the swirl flow due to a decrease in the value of the arc part of the tube. The result confirmed that the reduction in pitch to diameter with the increase of Reynolds number led to a decrease in heat transfer. From the trend of PEC, the outcome revealed that the twisted tri-lobe of the three-lobed number has the highest thermal performance among all lobed numbers investigated. It is proved that the lobed swirl at the (n =3) has the highest turbulent intensity and induced swirl intensity around the internal tube's wall due to the swirl flow. Finally, the twisted direction in the case of R-L-R-L presented more outstanding heat transfer due to the recirculation of the flow as the twisted direction changed.

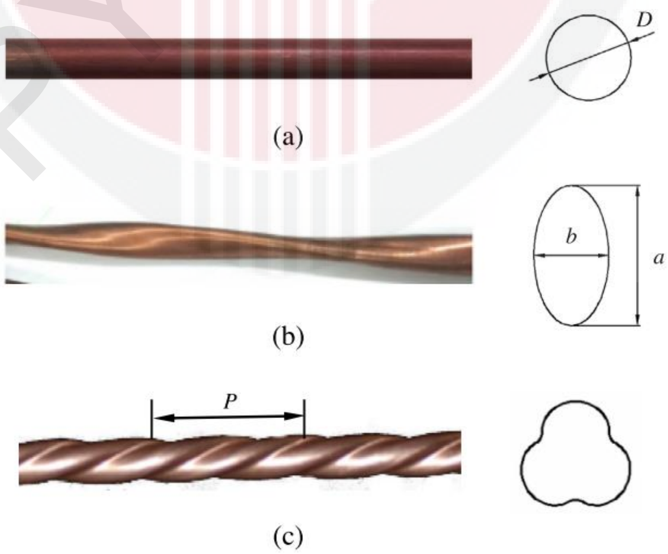

Figure 2.12: Effect of different tube's cross-sections on heat transfer (a) smooth channel, (b) oval tube and (c) twisted tri-lobe (Tang et al., 2015a)

A comparison between a twisted oval tube and a twisted three-lobed tube on the effect of heat transfer and pressure drop has been conducted by Indurain et al., (2020). The study was undertaken using several parameters of twist pitch, aspect ratio, and Reynolds number from 10,000 to 100,000. The result confirmed that the aspect ratio improves heat transfer and pressure drop. Therefore, the lower the aspect ratio, the higher the heat transfer and pressure drop. The result also disclosed that the twisted three-lobed tube presented more heat transfer at an aspect ratio of (c = 6) than the twisted oval tube. It can be explained by the intensity of flow generated by the twisted three-lobed.

2.4.5 The Hydrodynamic Approach of Lobed Swirl

The characteristics of swirl flow over lobed swirl generators have been investigated by Yan et al., (2020), who studied four-lobed swirl generators under different geometrical cross-sections, as seen in Figure 2.13. Several essential parameters have been investigated with detail, such as lobe numbers from (n = 3 to n = 10) as shown in Figure 2.14, pitch length ratios at (P/D = 4,6,8,10 and 12), pressure drop, decay rate, and Reynolds numbers ranging from (50,000 - to 125,000). The swirl effectiveness parameter has been adopted as the balance between the swirl intensity and the augmentation of pressure loss. Therefore, the effectiveness of the lobed swirl generator under different lobed numbers (n) versus different pitch-to-diameter (P/D) has been evaluated. In general, the result demonstrated a proportional relationship between the intensity of swirl flow and tube length downstream. Therefore, the increase in the tube length led to a decrease in the intensity of the flow.

Additionally, the study implies that the relationship between the swirl intensity and the growth in lobed number is inversely proportionate. According to the characteristics of the lobed swirl generator under the impact of both lobed number and pitch to diameter, the result confirmed that the lobed swirl generator at n = 4 and P/D = 8 presented the highest swirl effectiveness among all parameters investigated. Moreover, the result confirmed that the increase in Reynolds number led to a decrease in swirl decay by up to 27.9%.

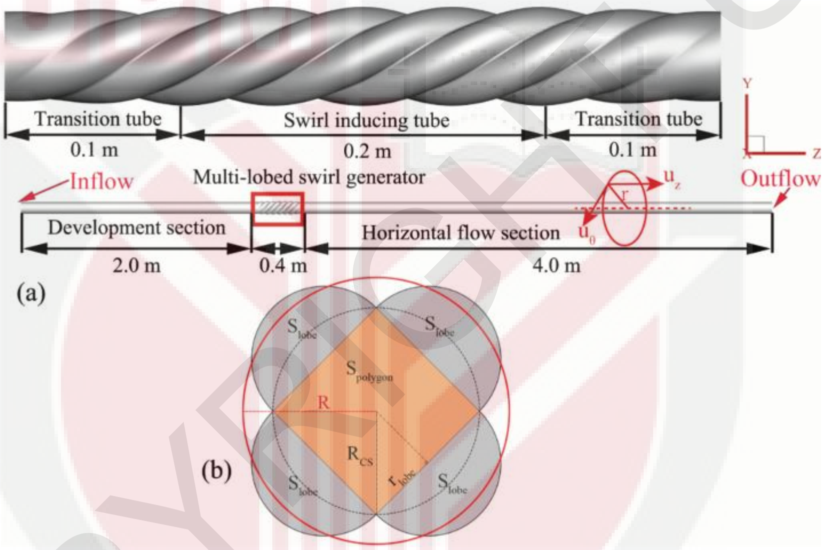

Figure 2.13: Four-lobed swirl generator (a) physical model, (b) geometrical cross-section (Yan et al., 2020)

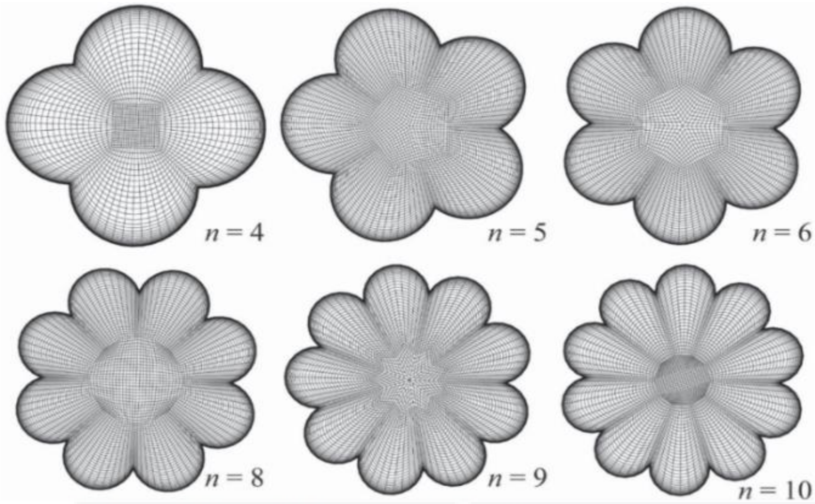

Figure 2.14: lobed swirl generator cross-section at different lobed numbers (Yan et al., 2020)

G. Li et al., (2015b) investigated four-lobed swirl generators under different twisted lengths. The length of transition parts before and after the swirl device was fixed at the value of 0.1 m, while the twisted device length itself was examined at different twisted lengths of 0.4 and 0.2 m, as seen in Figure 2.15. The result proved that increased swirl intensity led to a rise in tangential wall shear stress. Therefore, the short swirl pipe presented a high tangential wall shear stress compared with the twisted tube of 0.6 m due to the augmentation of swirl intensity associated with the short-twisted length. The effect of 0.6 m and 0.4 m swirl generators on pressure drop and total azimuthal velocity has been considered. The result confirmed that the pressure drop decreased with a decrease in twisted length due to the increase in contact area associated with a long-twisted length. At the same time, the result showed an increase in fluctuation flow linked with a short-twisted length.

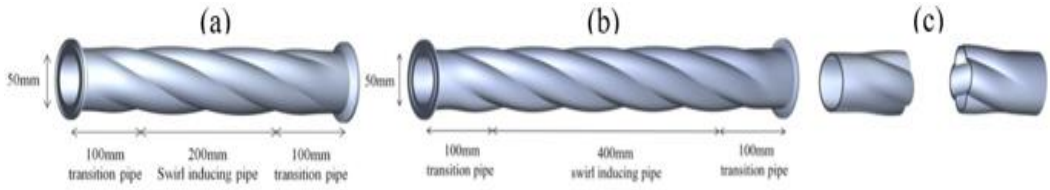

Figure 2.15: Four lobed swirl generator a) l = 0.4m, b) l = 0.6 and c) entry and exit transition parts cross-section (G. Li et al., 2015b)

Ariyaratne, C and Jones (2007) designed novel transition parts with considerable benefit before and after a lobed swirl. The study aimed to reduce the entry and exit pressure losses. The geometry is a four-lobe swirl generator with two transition parts designed at 100 mm in length and gradually changed from circular shape to lobe cross-section and vice versa, as illustrated in Figure 2.16. A comparison between alpha and beta transition at different transition multipliers of (n = 0.5, 1 and 2 mm) on lobed area development, as depicted in Figure 2.17, has been undertaken. The study also compared the impact of alpha-transition (α) and beta-transition (β) at the transition multiplier of (n =1) and the lobed swirl device itself (constant swirl pipe) on the swirl flow, Pressure drop, Swirl intensity and Swirl effectiveness. The study also compared the effect of the cylinder transition part and lobed transition part on azimuthal velocity, pressure drop and swirl effectiveness.

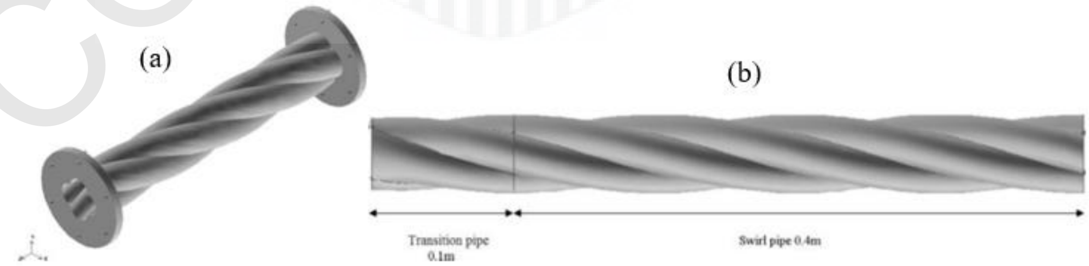

Figure 2.16: Four lobed swirl generator a) overall cross-section, b) lobed swirl with entry transition part (Ariyaratne, C and Jones, 2007)

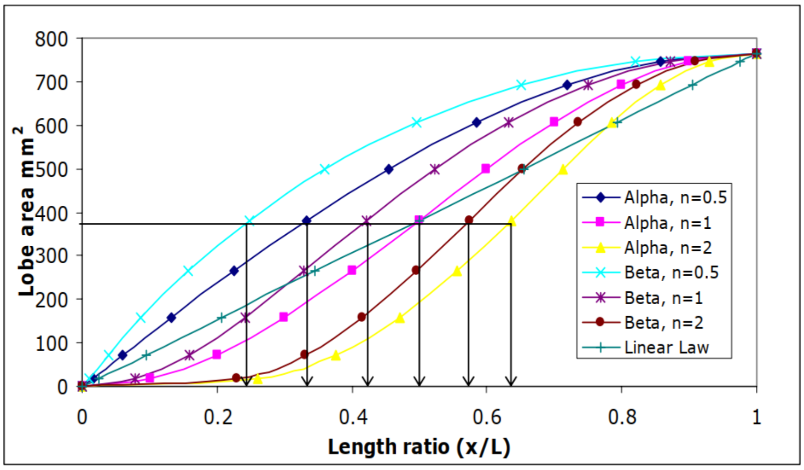

Figure 2.17: A comparison between alpha and beta transition under different transition multiplier values (Ariyaratne, C and Jones, 2007)

Considering the influence of transition multiplier n values, the result showed that decreasing n-value resulted in a higher tangential velocity and a higher-pressure loss. According to the swirl effectiveness parameter, the result also presented that the beta transition is 5% higher than the alpha transition. Also, the result proved that the swirl effectiveness obtained by the beta transition was higher than the lobed swirl device itself. The result presented higher swirl effectiveness associated with the lobed transition than the cylinder transition part. It can be attributed to the augmentation of pressure loss due to the sudden change in the cross-section between the cylinder transition part and the swirl device itself. On the other hand, the feature of the lobed transition part of a gradual change from a circle shape to a lobed cross-section and vice versa results in the reduction of pressure loss and increased swirl effectiveness.

The transition multiplier and variable helix are considered the most critical parameters that directly affect the characteristics of lobed transition parts. Therefore, these parameters were explored under different values addressed by many researchers (G. Li, 2016) (Chanchala Ariyaratne, 2005b). The studies were conducted over a 3-lobe and 4-lobe swirl generators, as depicted in Figure 2.18. The result pointed out that the transition multiplier n is a primary factor influencing the growth of the lobe area, particularly at the beginning and end of the transition section region. Therefore, 50% growth in the lobed area if n < 1 and vice versa, while at the n-value equal to 1, the lobed area development at the mid-length.

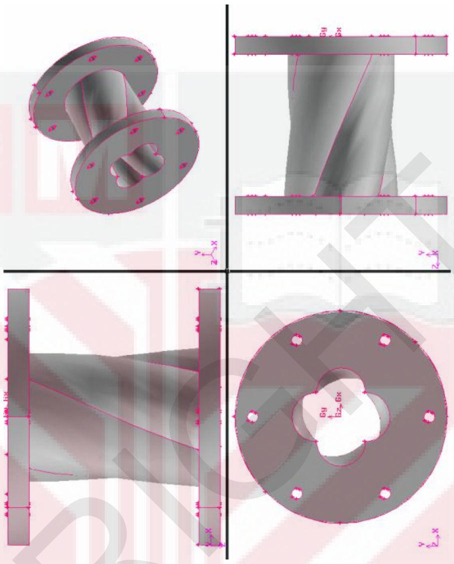

Figure 2.18: Transition part of Four lobed swirl generator (Chanchala Ariyaratne, 2005b)

Considering the variable helix (t), the study analysed the impact of the variable helix at different values of (t = 0.5, 1 and 2) on the configuration twisted cross-section of the transition parts, as shown in Figure 2.19. The result displayed that the twisted degree (helix shape) grew faster adjacent to the start of the t-value set less than one (t < 1) and developed quicker at the end of the t-value set greater than one (t >1). In the case of (t =1), the result demonstrated that the twisted helix of the transition part development constant is called (the geodesic helix) (Chanchala Ariyaratne, 2005b). The finding is that the transition multiplier and variable helix parameters are vital in controlling the intermediate area and the twisted degree of the transition part cross-section.

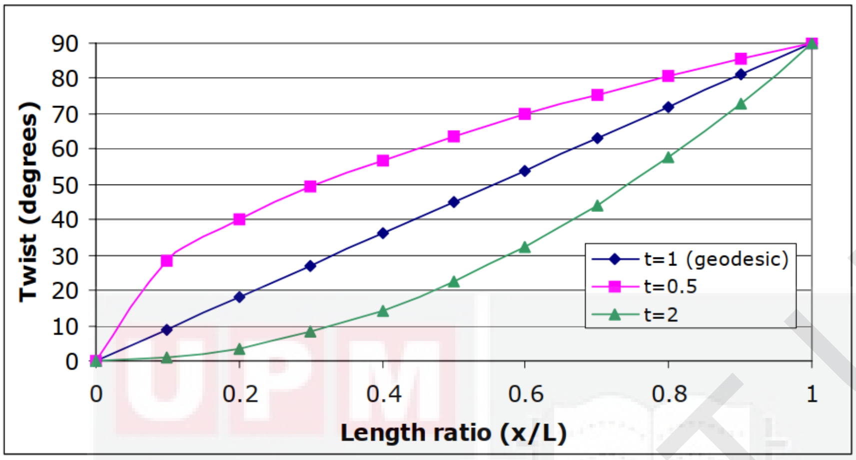

Figure 2.19: The behaviour of lobed transition length under different variable helix (Chanchala Ariyaratne, 2005b)

The result presented a superior benefit associated with lobed transition parts, which can be summarised as follows: (i) A reduction of pressure losses has been obtained at the entry and exit transition parts. (ii) According to swirl flow characteristics, the entry transition part increased the overall swirl intensity while the exit transition part reduced swirl decay.

2.5 Fundamental of Nanofluids

The low thermal conductivity of conventional water, oil, and ethylene fluids is the main challenge in thermal applications (Said et al., 2022). Nowadays, faster-speed devices are required in numerous thermal applications due to the tendency toward quicker speeds. As a result, the increase in speed leads to a rise in temperature. Therefore, improving heat transfer is highly required to keep up with this development. Consequently, finding a way to cool them down is the target outcome of many researchers (Habibishandiz & Saghir, 2022). Because of its high thermal conductivity, nanofluid can be considered a critical step in improving heat transfer as an alternative to traditional fluids (Awais et al., 2021).

Nanofluids, including nanoscale materials, such as carbon nanomaterials and metal & ceramic oxides, carbon nanotubes, and graphene oxide, have been widely used to enhance heat transfer (W. Ahmed et al., 2023). Numerous studies have been conducted in order to promote heat transfer and improve the thermal properties of the fluids by synthesising micrometre or millimetre nanoparticles in conventional fluids (Salman et al., 2020). Choi and Eastman (1995) introduced nanofluids as a novel form of working fluid for the first time. Over the past years, several studies have documented nanofluids' advantages in improving heat transfer rate (Bakthavatchalam et al., 2020; Gürdal et al., 2022; Mehta et al., 2022).

The type of conventional fluid, the concentration of nanoparticles, temperature value and surfactants utilized are considered the most critical parameters that directly impact the thermo-physical properties of nanofluid (Yurddas, 2022). Thermophysical properties of nanofluid, such as thermal conductivity, viscosity, density and specific heat, have been presented with favourable detail by Mehta et al., (2022). The size and shape of a nanoparticle seem to be significant factors for nanofluid properties (Maheshwary et al., 2017). A summary of previous studies related to metal oxide nanofluid has been listed in Table 2.1.

Table 2.1: A summary of previous studies of the impact of metal oxide nanofluids on thermal conductivity enhancement.

Ref.	metal oxide nanoparticles	Base fluid	Nanoparticles Diameter (nm)	Volume concentration (%)	Temperature range (ºC)	Thermal conductivity improvement
Kong & Lee (2020)	Al_2O_3	Water	30	0.38 -1.30 wt %	10–30 ºC	12% at a 1.3 vol.%
(M. S. Liu et al., (2006)	CuO	Ethylene glycol	23.6	1–5 wt %	Room temperature.	22.4 % at 5 vol.%
Tahani et al., (2016)	GO	Water	3.7-7	0.001-0.045 wt %	20-50 ºC	28.8 % at 0.45% vol.
Jamilpanah et al., (2016)	Fe_2O_3	Ethylene glycol	40-50	0–2 wt %	25-45 ºC	51.8 % at 2%vol. & 45ºC
(Arya et al., 2019)	MgO	Ethylene glycol	50	0.1-0.3 wt %	25-60 ºC	55.4 % at vol.0.3%
Rejvani et al., (2019)	SiO_2	Water	20-30	0.125 -.1.5 wt %	25-50 ºC	4 % at 1.2% vol.& 50ºC
(R. P. Singh et al., (2019)	TiO_2	Water	40-60	0.5-3.0 wt %	25-50 ºC	15.96 % at vol.3.0% & 50ºC
H. Li et al., (2015)	ZnO	Ethylene glycol	30	0.175 - .10.5 wt %	15-55 ºC	9.13 % at vol.7%
Kanti et al., (2022)	MWCNTs	Jatropha seed oil	N-A	0.2-0.8 wt%	25-65 ºC	2.29% to 6.76%
(Nadeem et al., (2020)	rGO	Ethylene glycol	N-A	0.02-0.05 wt%	25-70 ºC	11.3 % at vol.0.02%
Z. Chen et al., (2020)	NiO	Deionized water	20 to 80 nm	0.01-1 wt%	40-80 ºC	5.1 % at Temp. 80ºC

2.5.1 Hybrid Nanofluid

A hybrid nanofluid is a mixture of two or more nanoparticles dispersed in a base fluid. The relative surface area of hybrid nanoparticles is significantly higher than that of the base fluid, leading to a considerable increase in conveyance characteristics such as thermal conductivity and heat transfer coefficient, making the nanofluid attractive in many applications (Gupta et al., 2020). Numerous studies have proved that hybrid nanoparticles are required to enhance thermal performance (Adun et al., 2022; Khashi'ie et al., 2022; Malika & Sonawane, 2022). It has been reported that hybrid nanofluids might exhibit superior thermophysical properties than mono nanofluids (Babar & Ali, 2019).

Table 2.2: A summary of the impact of different hybrid nanofluid applications in thermal conductivity enhancement

Ref.	metal oxide nanoparticles	Base fluid	Nanoparticles Diameter (nm)	Volume concentration (%)	Temp. Range (ºC)	Thermal conductivity improvement
Tahmaseb et al., (2019)	Al_2O_3-Fe_2O_3 (50:50)	Engine oil 10 W40	Al_2O_3 (20), Fe_2O_3 (2-40)	0 - 4%	25-65 ºC	33% at 4vol.% &65ºC
Safaei et al., (2019)	$CoFe_2O_4$/SiO_2	Water -EG (60:40)	N-A	0.1–1.5%	25-50 ºC	37.7% at 15–65°C
Jin et al., (2021)	CNTs, Ag, Cu	Water & EG	CNTs (5), Ag (50), Cu (50)	0.01-0.05%	25-65 ºC	52.37% at 0.05 vol.% &65 ºC with Ag-CNT/water
Esfe, et al., (2018)	DWCNT–SiO_2	EG	DWCNT (2-4) – SiO_2 (30)	0.03 - 1.71%	30-50 ºC	38% at 1.71 vol.% &50 ºC
Wanatasanapan et al., (2020)	TiO_2-Al_2O_3 (20:80, 40:60,50:50, 60:40 and 80:20)	Water	TiO_2 (19.1) - Al_2O_3 (8.31)	0.2 - 0.8%	30-70 ºC	71% at 70ºC and (50: 50)
Pourrajab et al., (2021)	MWCNTs-COOH &Ag	Water	MWCNTs-COOH (20-30) &Ag (5-8)	0.004 - 0.16 %	20-50 ºC	47.4% at (0.04 vol.% Ag and 0.16 vol.% MWCNTs
Singh et al., (2020)	GO-CuO (20:80)	Distilled water	GO (1-4) - CuO (20)	0.03 - 0.3 %	30-60 ºC	51.6% at 0.3 vol.% with (GO-Dw)
Gulzar et al., (2021)	Al_2O_3–TiO_2(60:40)	Therminol-55	Al_2O_3 (–TiO_2 (20)	0.05 - 0.5 %	20-160 ºC	33.5% at 0.5 vol.% &65 ºC
Esfe et al., (2018)	MWCNT–MgO (20:80)	Water & EG (50:50)	MWCNT (3-15) –MgO (40)	0.015 - 0.96%	30–50 ºC	22% at 0.96 vol.% &50 ºC
Boroomandpour et al., , (2020)	MWCNT-ZnO- TiO_2	Water -EG (80:20)	MWCNT (5-10) -ZnO (10-30)-TiO_2(25-10)	0.1 - 0.4%	25-50 ºC	17.82% at 0.4 vol.% &50 ºC
Bakhtiari et al., (2021)	TiO_2-Graphene (70:30)	Water	TiO_2 (20-50) -Graphene (2-18)	0.005 - 0.5%	25-75 ºC	27.84% at 0.5 vol.% &75 ºC
Taherialekouhi et al., (2019)	GO- Al_2O_3 (50:50)	Water	GO (3.4-7) - Al_2O_3 (20)	0.1–1%	25-50 ºC	33.9% at 1 vol.% &50 ºC

The increase of Brownian motion phenomena combined with hybrid nanofluids more than single nanofluids is considered the feature of hybrid nanofluids in thermal application (Zakaria et al., 2022). A key objective of additive nanoparticles in a base fluid is to promote both the thermophysical characteristics of the nanoparticles as well as the base fluid's ability to transmit heat (R. Sharma et al., 2022). Incorporating two or more different nanoparticles can promote the thermal conductivity of single nanoparticles. These novel composite nanoparticles are called hybrid nanoparticles (Sajid & Ali, 2018). As listed in Table 2.2, several studies have reported on the impact of hybrid nanofluid applications on thermal conductivity.

2.5.2 The Characteristics of Thermal Conductivity Under Different Parameters

2.5.2.1 Impact of Volume Fraction and Temperature

The concentration of volume fraction and temperature generation during nanofluid preparation are considered the most critical parameters that profoundly affect nanofluids' characteristics. The thermal conductivity of nanofluid has a proportional relationship with the volume concentration of nanoparticles and temperature value (Sajid & Ali, 2018). Li et al., (2020) examined the effect of SiO_2 nanoparticles with several volume fractions of (0.005 to 5%) and a range of temperature from (5 to 65 ºC) on thermal conductivity. The result demonstrates that the increased volume concentration and temperature improved thermal conductivity.

Stalin et al., (2020) studied the impact of CeO2/water nanofluid under different solid volume fractions between (0.1-0.3%) and temperatures ranging between 20 - 60ºC on thermal conductivity improvement. The study revealed that the highest volume fraction and temperature caused a considerable increase in thermal conductivity by 35.97%. Tian et al., (2021) investigated the effect of TiO_2-Graphene/water at a different volume fraction and temperature on thermal conductivity enhancement. The study confirmed that the titanium dioxide-graphene/water nanofluid at the highest value of volume concentration of 0.5% and temperature of 75ºC presented an improvement in thermal conductivity at 27.84%. Kamel et al., (2020) studied the impact of mano-nanofluid of $Al2O_3$/water, CeO_2/water, and hybrid nanofluid of $Al2O_3$-CeO_2/water under different volume fractions and temperatures on thermal conductivity improvement. As stated in the study, the hybrid nanofluid demonstrated a high thermal conductivity of 8.8% as temperature and volume concentration increased.

2.5.2.2 Impact of Nanoparticle Size and Shape

It is worth mentioning that the type, the percentage concentration of volume fraction, the shape and the size of nanoparticles are considered the most critical parameters that might increase or decrease the thermal conductivity (Chopkar et al., 2008). (Hemmat & Seyfolah, 2015) studied the impact of MgO/water nanofluid under different particle diameters from 20, 30, 40, 50 and 60 nm and different volume concentrations from (0.5-2%) on thermal conductivity. The result demonstrated that the augmentation of volume fraction concentration and the reduction of nanoparticle diameter led to improved thermal conductivity. On the effect of improving thermal conductivity, multiple single nanofluids of Al_2O_3, TiO_2, CuO, and Cu under different size ranges of 20, 35, 40, and 50 nm have been evaluated by Ma et al.,(2020).

Among all case studies, Al_2O_3-nanofluid indicated the highest thermal conductivity linked with small nanoparticle size and increased volume concentration. It can be attributed to the improvement of Brownian motion caused by nanoparticle size reduction. Regarding nanoparticle shape, (Maheshwary et al., 2019) presented a study on the effect of spherical, cubic and rod of Al_2O_3, CuO, MgO and TiO_2 under different volume concentrations. The study revealed significant improvement in thermal conductivity combined with cubic- Al_2O_3/nanoparticle at the highest volume concentration of 2.5 wt.%.

A study on the thermal conductivity characteristics of GO was undertaken by Lin et al.,(2023) under different sizes and shapes of nanoparticles. The result also proved that the decrease in nanoparticle size led to increased thermal conductivity. It could be attributed to increased Brownian motion promoting the energy transfer between base fluid and graphene particles. Smaller nanoparticles often exhibit greater reactivity due to the rise in surface area-to-volume ratio. Nevertheless, bigger particles might have an additional promoting effect (Coetzee et al., 2020). Large particle sizes increased surface area, while small sizes resulted in more stability, avoided agglomeration and sedimentation, and improved the Brownian motion phenomena.

2.5.3 Application of Nanofluid

2.5.3.1 Nanofluid over Lobed Swirl Generator

Many researchers have recently focused on the characteristics of nanofluids and the transmission of convective heat through lobed swirl devices. Due to technological advancements and the need for energy conservation, this sector has been highlighted dramatically in many studies. The additive nanoparticles in conventional fluids lead to remarkable thermal conductivity improvements, but increased hydraulic power is required due to the augmentation in viscosity (Taheran & Javaherdeh, 2019). Therefore, the fluctuation between swirl flow, turbulent flow and nanofluid is expected to increase heat transfer and pressure losses.

Omidi et al., (2018) studied the impact of the helical coil under varying lobe numbers on heat transfer and fluid flow characteristics numerically. According to the lobe cross-section, the study outcome can be divided into four points: (i) the increase in lobe number caused an augmentation in swirl flow and led to a uniform distribution in the temperature situation, (ii) the higher Nusselt number and lower friction factor are noticeable with a more lobed number, (iii) in comparison with twisted tapes and other techniques, the lobed number has a significant impact on heat transfer but little effect on pressure drop, and (iv) from the side of the nanofluid implications, the result deduced that the heat transfer improved to 28% with applicable pressure drop compared with water as a working fluid.

The impact of corrugated coil tubes under different lobed cross-sections on heat transfer and turbulent nanofluid flow has been analyzed by Zaboli et al., (2021). The study was performed under other geometrical effective parameters of lobed numbers three, four, and five and nanofluids of Al_2O_3, CuO, and SiO_2 at several volume concentrations with a turbulent flow ranging from 14,500 to 23,500. The result indicates a 4.8% and 3.7% increase in heat transfer and pressure drop associated with the five-lobe number due to the augmentation of swirl flow. Regarding thermal performance improvement, the three-lobe cross section presented the highest value compared to all the cases investigated. It is attributed to the reduction in friction factor compared with the five lobes.

Omidi et al.,(2019) evaluated the effect of a three-lobe twisted tube linked with a Y-tape insert technique on the application of heat transfer and the characteristics of turbulent flow over the heat exchanger. The metal nanoparticle adopted is Al_2O_3 dispersed in water at different volume concentrations from 0.01 to 0.03% generated at various Reynolds numbers ranging from 5,000 to 20,000. It can summarize the finding as follows: (i) the empty three-lobe twisted tube can produce swirl flow and growth of the temperature gradient adjacent to the wall, (ii) according to the Y-table technique, the outcome shows an augmentation in heat transfer to 43% more than the plain tube. Still, it has an insignificant impact on thermal performance enhancement due to the dramatic increase in friction factor to 2.8 times more than a plain tube, and (iii) regarding the application of nanofluid, the result revealed an augmentation in friction factor in terms of a twisted tube with insert. Furthermore, the system's applicability is more effective with the empty, twisted tube of three-lobe under a low Reynolds number.

2.6 Summary

The literature mentioned that the improvement of thermal performance in many swirl applications depended on the accuracy of the design and the relation between the thermal flow field and hydrodynamics. Regarding this theory, comprehensive studies have been presented on fluid flow characteristics and heat transfer over swirl flow devices. The literature review introduced sufficient knowledge and background on the lobed swirl generator under different effective parameters such as lobed number (n), twisted length (l), twisted angle (θ) and pitch-to-diameter (P/D). Based on the use of lobed transition parts before and after, the lobed swirl itself under effective parameters such as transition multiplier (n) and variable helix (t) was investigated (G. Li, 2016). The literature proved that the transition part is an appealing innovation that enhances swirl effectiveness, reduces pressure loss, increases the overall swirl intensity, and reduces swirl decay (Ariyaratne, C and Jones, 2007). It is worth mentioning that the lobed swirl generator with its transition parts is usually used in the field of fluid flow, especially in the area of improved transportation of Particle-Laden Liquids (Tonkin, 2005) and swirl pipe Clean-In-Place procedures (G. Li et al., 2015a). Also, the literature presented a significant assessment of the impact of nanofluid on thermal applications. Due to its high thermal conductivity, nanofluid is considered a vital step in the thermal application area. However, nanofluid includes high thermal conductivity of conventional liquids, and the sedimentation and agglomeration of this technique are limited to use in many thermal systems (Awais et al., 2021).

Although many swirl flow techniques have been innovated to improve heat transfer by developing heat exchanger surface area, the smooth channel is still vital for heat exchangers. The induced swirl flow using corrugated channels led to increased heat transfer associated with augmentation of pressure loss. Therefore, creating swirl flow inside the smooth channel by mounted lobed swirl generator at the entrance of the pipe is the motivation behind this study. The advantage of a lobed swirl generator is represented in its ability to produce high swirl intensity and reduce pressure loss. Moreover, the capability of a lobed swirl generator makes the particles suspension during fluid flow, as well as the ability of nanofluid to improve heat transfer due to the contain of high thermal conductivity, is the motivation for the use of nanofluid and hybrid nanofluid in the present study. To the best of our knowledge and based on the research mentioned above, we can conclude the summary of the literature review as follows: (i) there is no study has been conducted regarding the impact of lobe swirl generators and their transition components in thermal application, (ii) also, the use of a lobe swirl generator with its transition part in the field of thermal application is rare. The behaviour of the swirl flow is not entirely understood (iii).

Moreover, the literature lacks a combination of the lobe swirl generator with its transition parts and nanofluid. Therefore, there is a need for numerical and experimental study on lobe swirl generators linked with single and hybrid nanofluid to fully explore and deeply understand the thermal performance improvement under different influential geometrical parameters (iv) due to the augmentation of pressure loss associated with the latest thermal techniques; new techniques are needed to maintain the pressure loss to an acceptable level. The transition parts' ability to reduce pressure loss and increase overall swirl intensity (Ariyaratne, C and Jones, 2007) can overcome this problem and present a beneficial future solution in thermal application. Therefore, exploring and applying this phenomenon numerically and experimentally is considered the motivation behind the current study, and (v) The literature also presented the ability of a lobed swirl generator to keep the particles in suspension due to the advantage of the transition part. At the same time, the sedimentation and agglutination of nanoparticles are still a big challenge in many applications. Therefore, the current study aimed to evaluate this phenomenon numerically and experimentally.

CHAPTER 3

METHODOLOGY

3.1 Overview

Better energy conservation could be obtained by considering the heat exchanger's optimum design. Developing beneficial heat transfer surfaces with less pressure loss is the key to improving heat exchangers' thermal performance (Shi et al., 2021). The lobed swirl generator produces tangential velocity adjacent to the wall and axial velocity concentrated in the core, which is the reason for generating centrifugal forces, leading to the development of swirl flow through the pipe (Tang et al., 2015a). Creating secondary flow and breaking the thermal conductivity (disturbing the thermal boundary layer) is the benefit of the swirl flow induced by the lobe swirl device(C et al., 2022).

The swirling flow could significantly increase heat transfer rates by about 20% over the heat transfer enhancement area and uniformize the heat transfer distribution compared to impingement cooling (Liu et al., 2019). If heat transfer is the targeted outcome, the turbulent flow is considered due to its ability to produce swirl flow, promoting the thermal characteristics and heat transfer between the flow and the surface (Xie et al., 2017). It can attribute swirl flow in heat transfer enhancement to several points, such as (i) the swirl generator produces turbulence flow while expanding the total flow length in the pipe (Bilen et al., 2022). (ii) a strong swirl flow promotes heat transmission by reducing the thermal boundary layer adjacent to the wall (Bali & Sarac, 2014). (iii) expanding the heat exchanger's surface area and changing the direction of fluid flow are the results of swirl flow, which is considered the main reason for improved heat transfer (Tomar & Kumar, 2020). (iv) compared to the others, it was determined that the flow typically is not mixed adequately when the tubes are smooth (Omidi & Farhadi, 2018). The overall methodology process flow chart adopted in the current study is depicted in Figure 3.1. The overall flow chart shows that the methodology of the current study was carried out using numerical and experimental approaches.

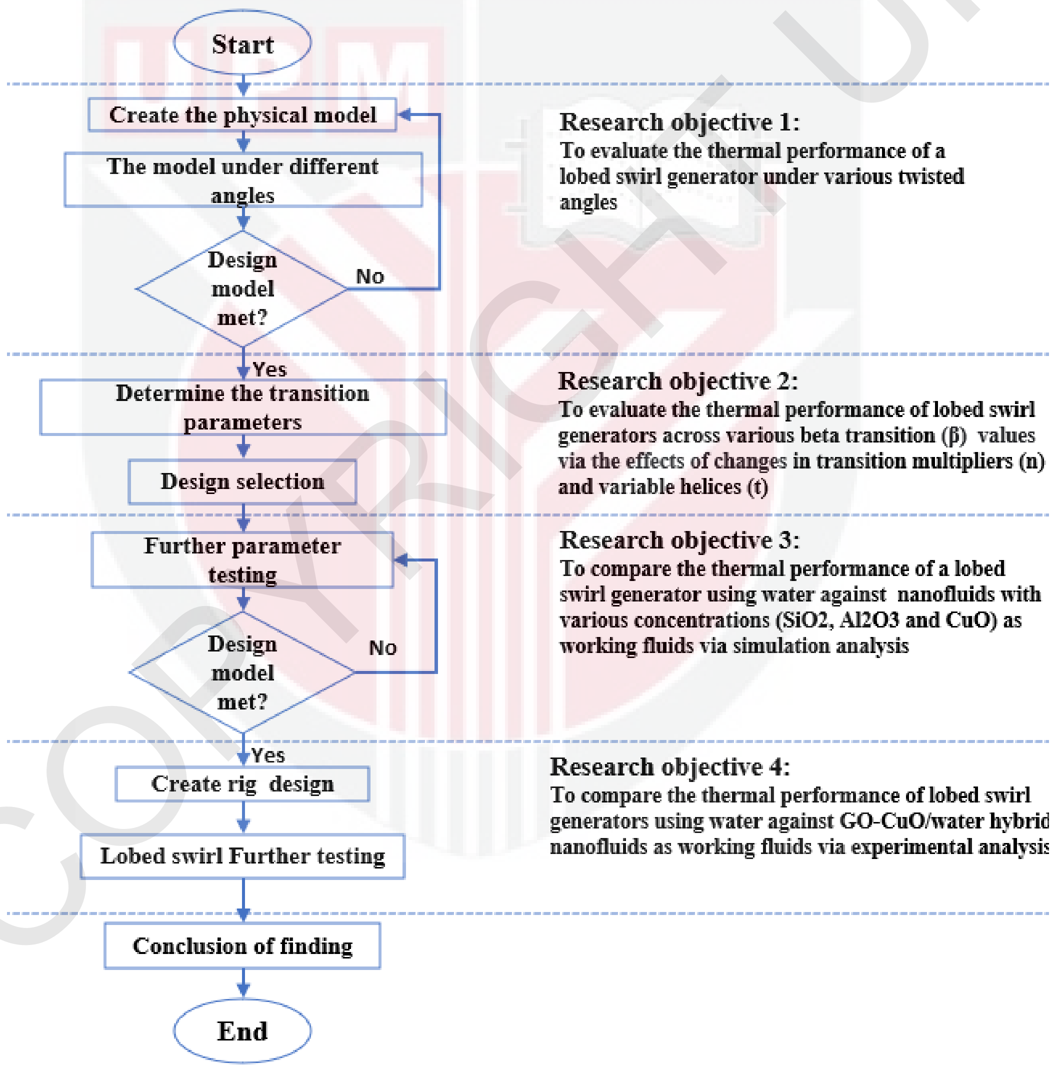

Figure 3.1: Methodology overall flow chart

The numerical method has been performed using Integrated Computer Engineering and Manufacturing (ICEM-CFD) Ansys for mesh generation and Ansys Fluent for numerical setup. The validation of the numerical method and the grid-independent test are presented in this chapter. The four-lobe swirl generator's impacts on the rate of heat transfer and pressure drop inside the test tube are specifically examined in the experimental approach of the present investigation. According to the physical model in the experimental approach, the researcher employed a rapid prototyping process to create the devices that were used utilizing ABS material. The working fluids are water, nanofluid, and hybrid nanofluids, which are investigated using the relative formula and related instruments numerically and experimentally.

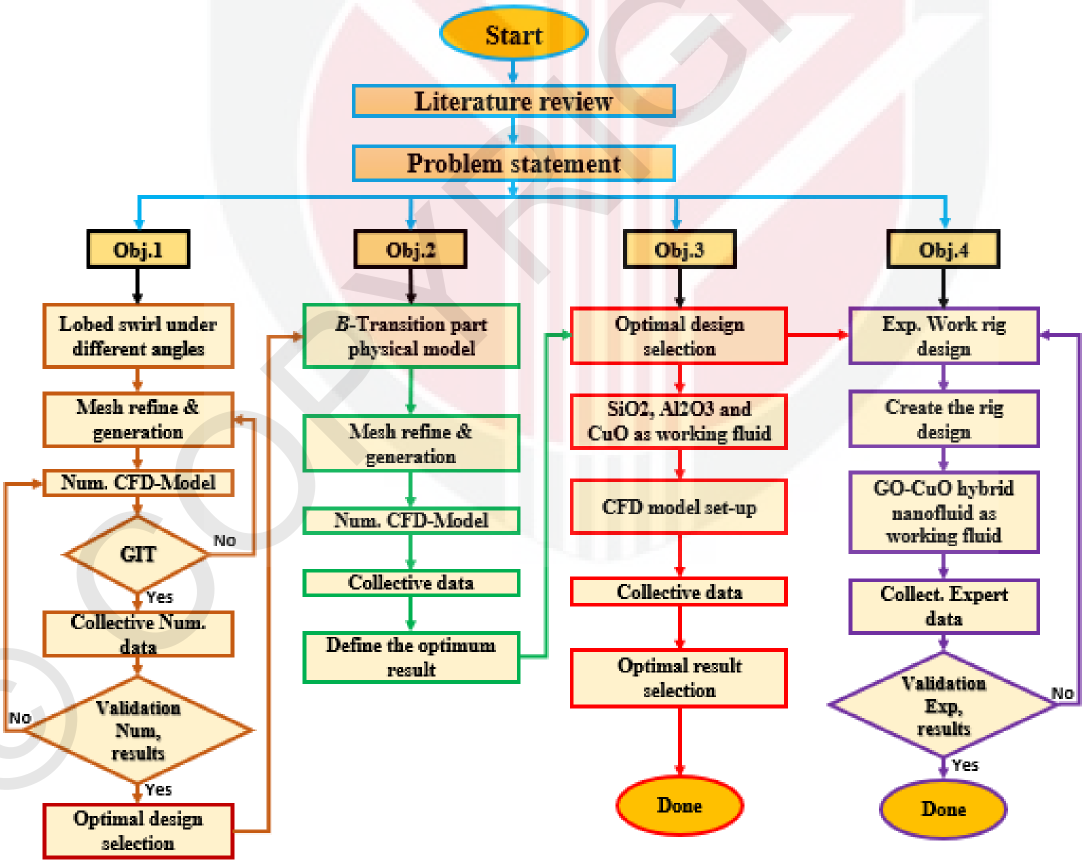

Figure 3.2: Flow chart of research work

3.2 Physical Model

The physical model adopted in the current study is a four-lobed swirl generator, which is equipped with a plain tube to improve the flow within a smooth channel and, as a result, improve heat transfer due to the change in the flow characteristics from straight to swirl. The lobed swirl generator is examined under different twisted angles. The lobed swirl generator has two essential parts known as transition components. Also has been investigated under different transition multipliers (n) and variable helix (t). The test section of stainless steel is studied under constant heat flux. The entry suction was extended enough to ensure the entry flow at a fully developed.

3.2.1 Four-lobe Swirl Device

The geometrical cross-section in the current study was plotted using the Reference Geometry Plane approaches and the Left Boss/Base feature utilizing SolidWorks software. The lobe swirl generator over a length of 0.4 m and the pitch-to-diameter ratio of (P/D = 8) was chosen as the optimal design (C. Ariyaratne & Jones, 2007). To plot the swirl device, three essential radii of tube radius (R), lobe radius (rlobe) and the radius of the polygon area (Rsc) are taken into consideration, as shown in Figure 3.2. The equations (18) & (19) are considered to determine the lobe radii (Yan et al., 2020).

$$r_{lobe} = \sqrt{\frac{2\pi tan\left(\frac{360}{8}\right) R^2}{8 + 4\pi + tan\left(\frac{360}{8}\right)}} \tag{18}$$

$$R_{cs} = \frac{r_{lobe}}{sin\left(\frac{360}{8}\right)} \tag{19}$$

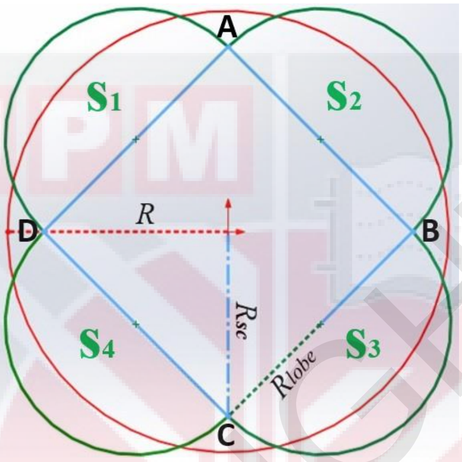

Figure 3.3: Main radii of lobe swirl device

As shown in Figure 3.3, the lobe swirl device was constructed by splitting and establishing multiple parallel planes. The lobe swirl device with 21 planes was developed constantly with the same distance at 10 mm (X/L = 0.05) to ensure a constant helix along the tube and avoid the steeper. Therefore, the space between each plane is 4.5º, 9º, 13.5º, and 18º and 13.5º based on the twisted degree adopted of (θ = 90º, 180º, 270º, 360º and 450º), respectively See Appendix A. Table (A1 -A5). The length of the lobe device twisted tube is 0.2 m with an equivalent diameter of 0.05 m. The four-lobe cross-section's surface area and perimeter are assessed as follows:

The four lobes area (A4L) = the polygon area at the centre (Ap) (ABCD) + the area of four segments on the sides (A4s) (S1-S4). Therefore,

$$A_{4L} = \frac{r_{lobe}^2}{tan\left(\frac{360}{2}\right)} \times n + \frac{\pi r_{lobe}^2}{2} \times n \quad (20)$$

$$P_{4L} = n \times \frac{2\pi r_{lobe}}{2} \quad (21)$$

$$D_{h4L} = \frac{4A_{4L}}{P_{4L}} \quad (22)$$

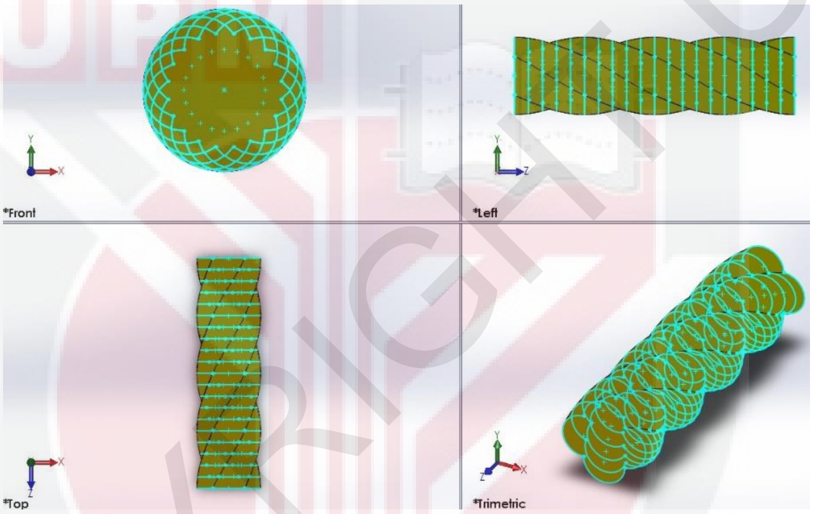

Figure 3.4: Lobe swirl device under 21 planes from different sides at (θ = 360º)

3.2.2 Transition Parts

The benefit of transition parts is represented in their capability to improve the overall swirl intensity and reduce pressure loss; therefore, it is expected to enhance the thermal performance of the heat exchanger. (C. Ariyaratne & Jones, 2007) studied the transition parts at different geometrical cross-sections of circular and lobe shapes. The result proved that the sudden change in the transition from circular shape to lobe increases pressure losses and decreases swirl effectiveness compared with the lobe transition part. According to the lobe shape, the transition part required a different way of development since it required a gradual change from lobe form to circle and vice versa. The Reference Geometry Plane and Lofted Boss/Base options of the SolidWork-2015 program were utilized to construct the cross-section of the transition parts.

The steps involved in creating the transition part are listed below:

- According to the equivalent diameter (de) and pitch to diameter (P: D), the twisted transition part was evaluated using equation (23). As a result, the length of the transition part can be determined using equation (24).
- The transition part was created gradually from a circle shape (no lobe) at 45º
- to fully develop at 90º to avoid unnecessary pressure loss.
- Two key variables of (f&f1) were introduced using equations (25) & (26).
- Based on variables (f&f1), the core radius (R) was calculated using equation (27).
- The variable (y) was introduced using equation (28) to maintain steady lobe area development at each step.
- The intermediate area at each step (LAi) and the fully developed area (LAFD) were calculated using equations (29) and (30), respectively.
- Equation (31) was used to adopt the cosine function to prevent discontinuities in the area throughout the growth of the transition phase, particularly at the beginning and end (C. Ariyaratne & Jones, 2007).

$$twist\ (degree/m) = \frac{360}{(P{:}D_{ratio}) \times de} \quad (23)$$

$$L_t = \frac{1000\ mm}{Twisted(degree/m)} \times 90° \quad (24)$$

$$f = \left(\gamma - \frac{1}{2}sin2\gamma\right) \quad (25)$$

$$f_1 = \frac{1}{2}\left[1 - \frac{1}{1 - tan\gamma}\right] \quad (26)$$

$$R = R_1\sqrt{\frac{\pi}{4f + 4ff_1^2 - 4\sqrt{2}ff_1 + 2}} \quad (27)$$

$$y = f_1 \times R \quad (28)$$

$$LA_i = 4r_{lobe}^2 - R^2(\pi - 2) \quad (29)$$

$$LA_{FD} = 4r_{lobe}^2 - R^2(\pi - 2) \quad (30)$$

$$\frac{x}{L} = \frac{Cos^{-1}(1 - 2(\alpha\ or\ \beta)}{\pi} \quad (31)$$

3.2.2.1 Alpha and Beta Transition

Alpha (α) and beta (β) transition techniques are the crucial parameters directly impacting the intermediate lobe area development. As illustrated in equation (32), Alpha transition is defined as the ratio between the area at an intermediate stage (LAi) to the area at a fully developed pattern (LAFD). On the other hand, the beta transition is defined as the ratio between the area at an intermediate stage to the difference between the area at the core region and the area at a fully developed as depicted in equation (33). A comparison between the effect of beta and alpha transitions on the swirl effectiveness was investigated by C. Ariyaratne & Jones (2007). The outcome indicated an increase in swirl effectiveness by 5%, which was linked with a beta transition greater than that of the Alpha.

$$\alpha = \frac{LA_i}{LA_{FD}} \tag{32}$$

$$\beta = \frac{\frac{LA_i}{\pi R^2 - LA_i}}{\frac{LA_{FD}}{\pi R^2 - LA_{FD}}} \tag{33}$$

3.2.2.2 Transition Multiplier

The transition multiplier (n) is the parameter used to control the intermediate area of the transition section in each step as desired. The development in the lobe area is mainly influenced by the n-values given, particularly at the beginning and the end of the transition portion region. (Chanchala Ariyaratne, 2005a) evaluated the lobed area growth pattern under alpha (α) and beta (β) transitions at various values. The investigation showed that the beta transition exhibited a 50% point near the beginning more than the Alpha transition. To create the transition part area at different values of the transition multiplier (n), equations (34) & (35) are considered.

$$\alpha = \left[\frac{AL_i}{AL_{FD}}\right]^n \tag{34}$$

$$\beta = \left[\frac{\frac{LA_i}{\pi R^2 - LA_i}}{\frac{LA_{FD}}{\pi R^2 - LA_{FD}}}\right]^n \tag{35}$$

3.2.2.3 Variable Hhelix

The variable helix (t) is defined as the essential factor that significantly impacts the twisting shape during the development of the transition section. The growth of the twisted shape of the transition tube can be divided into two essential types based on the t-value given. Suppose the power law is maintained at (t =1). In that case, the twisted cross section will be development constant (geodesic) (Chanchala Ariyaratne, 2005a). In contrast, in terms of setting the power law at more incredible or less than one, the twisted growth will be formed by brachistochrone, as suggested by Raylor (1998). The helix shape of the transition tube developed faster at the exit in the case of a set (t > 1), while the twisted helix of the transition tube grew faster at the start if (t < 1). Equation (36) controls the twisting of the transition tube concerning the length as required by adjusting the t-value.

$$Twist[0{,}90°] = \left(\frac{x}{L}\right)^t \times 90° \times twisted\ diraction \tag{36}$$

The values of transition parts at different parameters are listed in (Appendix A Table A6); the final shape of the transition part cross-section with 18 planes is shown in Figure 3.4.

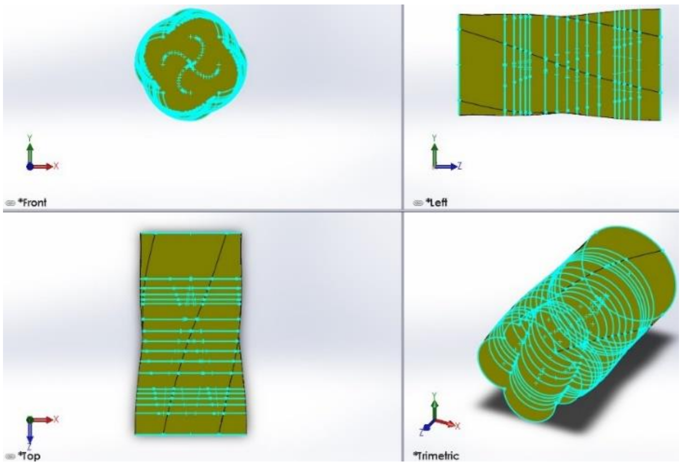

Figure 3.5: Transition part under 18 planes from different sides at (θ =360º)

3.2.3 Computational Domain

The 3-D cross-section of the solid domain has been created utilising SolidWork-2015 software. It could subdivide the solid domain into several fundamental parts, as shown in Figure 3.5. The entrance section was sufficiently extended at 0.8 m based on the diameter of 0.05 m and the given Reynolds number value to ensure the turbulent flow at a fully developed pattern. The entry section has been calculated according to equation (37). The lengths of both transitions' parts at 0.1m and the lobe swirl device at 0.2 m were adopted as crucial parameters. The wall of the test section was subjected to constant heat flux. A lobed swirl generator was studied under different lobe angles of (θ = 90º, 180º, 270º, 360º and 450º) using water as working fluid under a different Reynolds number Ranging from (30,000 – 55,000). (ii) in a second attempt, the lobed swirl generator was fixed at the angle of (θ = 360º). At the same time, the working fluid adopted is different nanofluids of SiO_2, Al_2O_3, and CuO-water volume concentrations of (1 to 5%) under various Reynolds numbers (Re) from 15,000 to 35,000.

$$L_e = 4.4D(Re)^{1/6} \quad (37)$$

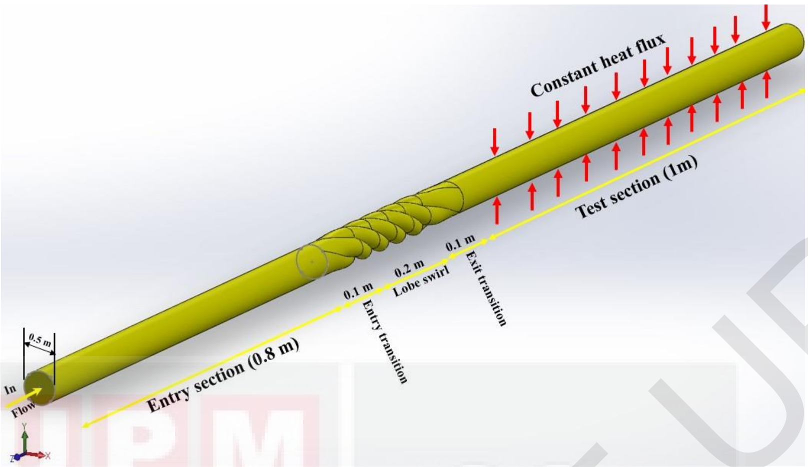

Figure 3.6: The lobed swirl generator in 3-D mode as a solid domain

3.2.4 Meshing

Hexahedral cells were used to mesh the geometry using the Integrated Computer Engineering and Manufacturing (ICEM-CFD) Ansys, 2020 R2 software. The hexahedral cells together with structured mesh, were considered to enable the solver to run faster and minimize the numerical diffusion (Vinchurkar & Longest, 2008). The structured mesh is more effective than the unstructured mesh when dealing with complicated geometry, such as the lobed swirl, since it makes mesh refinement easier (G. Li, 2016). The four-lobe swirl generator's geometrical cross-section has excessively sharp angles, making the application quite complex. Therefore, with its advantage of top-down blocking, ICEM CFD has been considered to create an efficient mesh model without subdividing the geometry (Sica et al., 2021). The steps for generating the mesh using ICEM CFD software are listed below:

- The (centre of 3 points/Arc) option establishes the centre point at plane corners.
- Selecting the entities feature can generate the parts of the boundary condition, while the location option is used to create the fluid body.
- Select all the appropriate visible objectives to build a block, then subdivide the block utilizing the recommended point and edge selections.
- Selecting both the block and faces options can construct an O-grid block.
- Select all the vertices, centre points, rotational angles, and vectors, and then choose the rotate vertices technique to change the position.
- By considering the twisted angles, the block can be subdivided into several parts, and then the rotate option can be selected to create the O-grid blocks, as depicted in Figure 3.6 (a-c).
- Choose the blocking association method and join the vertex to the point and the edge to the curve.
- Apply the Pri-Mesh Parms option to generate the mesh.
- Ensure the angle is more than 18º and check the mesh quality using the Pre-mesh quality histogram's function.
- If necessary, smooth the mesh
- Specify the output mesh, then determine the solver.

The surface mesh created around the related block at various lobed swirl angles is shown in Figure 3.7(a–c).

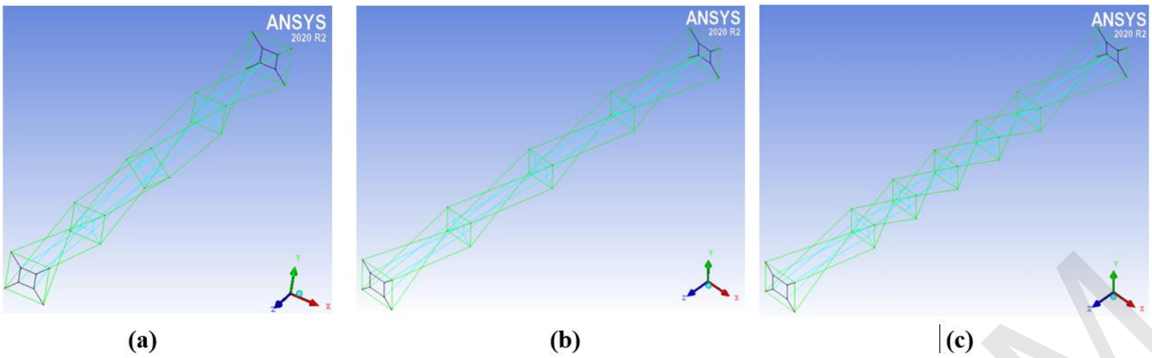

Figure 3.7: Create an O-grid feature over different lobed swirl angles of (a) 90º (b) 180º (c) 360º

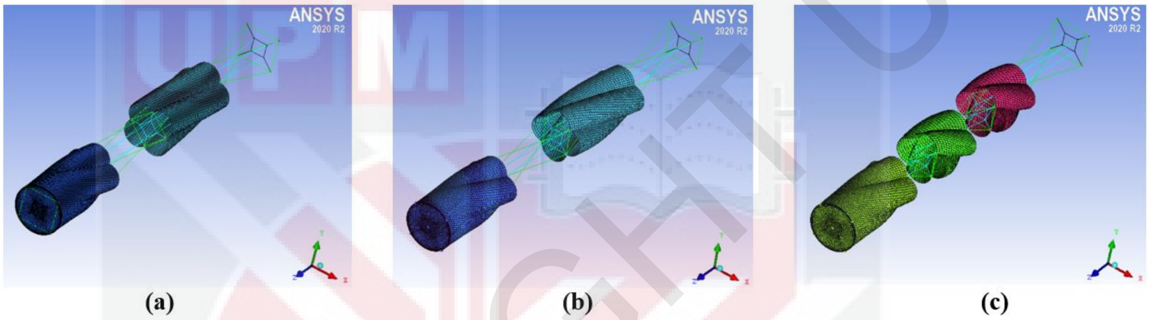

Figure 3.8: Generated surface mesh around the associated block at different lobed swirl angles (a) 90º (b) 180º (c) 360º

3.2.5 Modelling

Modal analysis offers substantial insight into a structure's dynamic properties. It may be used to give engineers information on how the design will react to various kinds of dynamic loads.

3.2.5.1 The Shear-stress Transport (SST) k-ω Turbulence

Menter (1993) proposed a novel (SST) k-ω (shear stress transfer) model. It has substantial advantages over k-ε models. (SST) k-ω model presented a considerable improvement in the solution compared with k-ω models (Hellsten, 1997). From the perspective of a wide range of flow, (Tang et al., 2015b) proved that the (SST) k-ω has a considerably demonstrated performance compared with other models. Six types of two-equation models were examined for a confined swirl flow at multiple swirl values (Engdar & Klingmann, 2002).

The study confirmed that the reduction in swirl number led to disagreement between the models and the experimental research, except the (SST) k-ω model agreed with low and strong swirl cases. The benefit of the (SST) k-ω model is improved turbulent viscosity and adjusted asymmetric diffusion components to more accurately predict the fluid separation driven by an adverse pressure gradient (Shadab et al., 2022). Tang et al., (2015a) studied the reliability of different models such as (SST) k-ω, Standard k-ω, Reliable k-ε, RNG k-ε and RSM to predict the flow over Twisted tri-lobed and oval tubes geometrical cross-section. The experimental and numerical data have been agreed with the (SST) k-ω model among all models investigated. The cell size adjacent to the wall resembles the dimensionless distance wall Y+. It should be less than 4 in order to verify the meshed of the viscous sublayer during the utilized (SST) k-ω model (Oneissi et al., 2016). According to the different attractive studies performed on the prediction of using the (SST) K-ω model and its agreement between the numerical and experimental study at low and strong swirl flow, the current work applies the (SST) K-ω on the flow induced by lobed swirl generator as a unique study.

3.2.6 Governing Equation

Numerous studies have shown how the (SST) k-ω model considerably improves predictability for complex turbulent flows with a substantial swirling intensity (You et al., 2020). The swirl flow produces different types of vortices (large and small eddies), leading to adverse flow separation and adverse pressure gradients, making the flow extremely complex to predict. Therefore (SST) k-ω model was adopted due to its capability to overcome this problem (Shadab et al., 2022). The flow is assumed to be turbulent, steady state, incompressible, one-phase, and three-dimensional (to create realistic effects). The governing equations have been evaluated as follows (Oneissi et al., 2016).

Continuity equation:

$$\frac{\partial}{\partial x_i}(u_i) = 0 \tag{38}$$

Momentum equation:

$$\frac{\partial(\rho u_i u_j)}{\partial x_i} = -\frac{\partial p}{\partial x_i} + \frac{\partial}{\partial x_i}\left[u\left(\frac{\partial u_i}{\partial x_i} + \frac{\partial u_i}{\partial x_i} - \frac{2}{3}\,\delta_{ij}\frac{\partial u_i}{\partial x_j}\right)\right] + \frac{\partial}{\partial x_j}\left(-\rho\overline{\acute{u}_i\acute{u}_j}\right) \tag{39}$$

Energy equation:

$$\frac{\partial}{\partial x_i}\left(u_i(E\rho + P)\right) = \frac{\partial}{\partial x_j}\left[\left(\lambda + \frac{Cp\mu_t}{pr_t}\right)\frac{\partial T}{\partial x_j} + u_i(\tau_{ij})_{eff}\right] = 0 \tag{40}$$

Where E is the overall energy and (τij)eff is the deviation of the stress tensor, which are evaluated as follows:

$$E = CpT - (P/\rho) + \frac{u^2}{2} \tag{41}$$

$$\tau_{eff} = \left[\mu_{eff}\left(\frac{\partial u_i}{\partial x_j} + \frac{\partial u_i}{\partial x_j}\right) - \frac{2}{3}u_{eff}\frac{\partial u_i}{\partial x_j}\delta_{ij}\right] \tag{42}$$

The following equations are considered to calculate the turbulence of kinetic energy (K) and frequency (ω):

$$\frac{\partial}{\partial x_i}(Ku_i) = \frac{1}{\rho}\left(\frac{\partial}{\partial x_j}\left(\Gamma_k \frac{\partial k}{\partial x_j}\right) + \hat{G}_k - Y_k + S_k\right) \tag{43}$$

$$\frac{\partial}{\partial x_i} = \left(\rho\omega u_j\right) = \frac{1}{\rho}\left(\frac{\partial}{\partial x_j}\left(\Gamma_\omega \frac{\partial \omega}{\partial x_j}\right) + \hat{G}_w - Y_\omega + D_\omega + S\_\omega\right) \tag{44}$$

Where Gk and Gω are, respectively, the generation of (k) and (ω), Yk and Yω are, respectively, the dissipation of kinetic energy and (ω) due to the turbulence. Γk is the effective diffusivity of K, and Γω the effective diffusivity of (ω). The value of Γk is evaluated as follows:

$$\Gamma_k = \mu + \frac{\mu_t}{\sigma_k} \tag{45}$$

$$\Gamma_\omega = \mu + \frac{\mu_t}{\sigma_\omega} \tag{46}$$

3.2.7 Boundary Condition

At the inlet section, the boundary conditions:

$$\frac{\partial u}{\partial z} = \frac{\partial v}{\partial z} = \frac{\partial w}{\partial z} = \frac{\partial T}{\partial z} = 0 \tag{47}$$

The downstream wall:

$$Wall(no\ slip)u = v = w = 0, T = T_w, q_w = 1000w/m^2 \tag{48}$$

At the outlet section

$$\frac{\partial u}{\partial z} = \frac{\partial v}{\partial z} = \frac{\partial w}{z} = 0, \frac{\partial T}{\partial z} = 0 \tag{49}$$

Mean velocity and mean temperature

$$\frac{\partial u}{\partial z} u = u = u_{min}, v = w = 0, T = T_{min} = 298k \tag{50}$$

3.2.7.1 Thermophysical Properties of Water

It is worth mentioning that the numerical study was conducted on two types of working fluids. The first was water as a base fluid to study the influence of different twisted angles on heat transfer and thermal performance. The Physical properties of water at various temperatures (SI units) have been measured by Tombs (2014). The thermal physical properties of water in the current at 25ºC listed in Table 3.1.

Table 3.1: Thermophysical properties for base fluid (Tombs, 2014)

Properties	Water
Density (kg/m3)	998.2
Viscosity (N.s/m2)	0.001003
Specific heat (J/kg.K)	4182
Thermal conductivity (W/m.K)	0.6

3.2.7.2 Thermophysical Properties of Nanofluids

The second numerical study was performed on a lobed swirl generator at the fixed twisted angle at 360º and different SiO_2, Al_2O_3, and CuO-water nanofluids as the working fluid at different volume concentrations of 1, 2, 3, 4 and 5%. A comparison between the first numerical study and the second numerical study is seen in Table 3.4. The nanoparticles incorporated in the simulations by only change of properties in the fluid (density, viscosity, thermal conductivity, and viscosity) and the turbulent intensity were set at 5%, which is a good default value in most CFD engineers, and 5% is enough to consider the turbulent flow fully developed (Bari & Saad, 2013). The flow is set as single-phase, which can model the base fluid and nanoparticles at the same temperature and velocity field (Göktepe et al., 2014). According to the impact of nanofluid on turbulent parameters, the Kω-SST turbulence model can estimate the turbulence energy and determine the turbulence scale, which seems to be the preferable choice of turbulence model (Wróblewski & Fraczek, 2014).

3.2.7.2.1 The Thermal Conductivity (***Keff***)

The empirical correlation and Brownian motion of nanoparticles in a circular tube have been utilized to assess the effective thermal conductivity (Hasan et al., 2022)

$$K_{eff} = K_{static} + K_{Brawnian} \quad (51)$$

$$K_{static} = \left[\frac{(K_{np} + 2K_f) - 2\Phi(K_f - K_{np})}{(K_{np} + 2K_f) + \Phi(K_f + K_{np})}\right] \quad (52)$$

$$K_{Brwnian} = 5 * 10^4 \beta\phi\rho_f Cp_f \sqrt{\frac{KT}{2}} f(T,\phi) \quad (53)$$

$$Where \quad k = 1.3807 * 10^{-23} \quad J/K \quad (54)$$

$$Boltzmanconstant: k = 1.3807 * 10^{-23} J/K \quad (55)$$

Shamani et al., (2015) demonstrated the β-value correlation of SiO_2, Al_2O_3, CuO, and ZnO nanoparticles at temperatures ranging from 298 to 363 K and volume concentrations ranging from 1 to 10%. The value of the correlation β of the nanoparticles adopted in the current study has been listed in Table 3.2.

Table 3.2: The correlation β-value for different nanoparticles (Al-Shamani et al., 2015)

Nanoparticle type	**β**	**Concentration (%)**	**Temerature (K)**
SiO_2	1.9526 (100φ)- 1.4594	1% ≤ φ ≤ 10%	298 K ≤ T ≤ 363 K
Al_2O_3	8.4407(100φ)- 1.07304	1% ≤ φ ≤ 10%	298 K ≤ T ≤ 363 K
CuO	9.881(100φ)- 0.9446	1% ≤ φ ≤ 6%	298 K ≤ T ≤ 363 K

The modelling (T, ϕ) can be calculated as follows.

$$(T,\phi) = (2.827 * 10^{-2}\phi + 3.917 * 10^{-3})\left(\frac{T}{T_0}\right) + (-3.0669 * 10^{-2}\phi - 3.3991123 * 10^{3})1\% For \leq \phi \geq 4\% \; and \; 300K \leq T \geq 325K \quad (56)$$

3.2.7.2.2 Viscosity (*μeff*)

The effectiveness of viscosity may be calculated using the following correlation (Alawi et al., 2018):

$$\mu_{eff} = \mu * \left(\frac{1}{1 - 34.87\left(\frac{d_p}{d_f}\right)^{-0.3} * \phi^{1.03}} \right) \quad (57)$$

$$Where \quad d_f = \left[\frac{6M}{N\pi\rho_{f0}}\right]^{1/3} \quad (58)$$

Where N is the Avogadro number = 6.022x1023 mol-1, M is the molecular weight of the base fluid, and ρfo is the density of the based fluid measured at temperature To=273K.

3.2.7.2.3 The Density (*ρeff*)

The following equation may be used to determine the density of nanofluid (Mohammed et al., 2013)

$$\rho_{nf} = (1-\phi)\rho_f + \phi\rho_{nf} \tag{59}$$

Where ρ_{nf} and ρ_f are the solid nanoparticle density and the based fluid's density, respectively.

3.2.7.2.4 The Heat Capacity (*Cpeff*)

The effectual heat capacity of nanofluid can be determined by the following correlation (Ghasemi & Aminossadati, 2010)

$$(\rho_{cp}) = (1-\phi)(\rho_{cp})_f + (\phi\rho_{cp})_{np} \tag{60}$$

Where (ρcpnf) and (ρcp) are the heat capacities of the solid nanoparticles and based fluid, respectively.

The values of all thermophysical properties of SiO_2, Al_2O_3, and CuO-water nanofluids under different volume concentrations of (1-5%) and nanoparticles diameter of dp = 30 nm are depicted in Tables (3.3, 3.4 and 3.5) respectively.

Table 3.3: Thermophysical properties measured of SiO_2/water

Properties	**SiO_2**				
Volume concentrations	1%	2%	3%	4%	5%
Density (Kg/m3)	1009.03	1021.06	1033.09	1045.12	1057.15
Viscosity (Ns/m²)	1.09E-03	1.21E-03	1.35E-03	1.53E-03	1.76E-03
Specific heat (J/kg K)	4106.147	4032.081	3959.740	3889.065	3819.998
Thermal conductivity (W/m. K)	0.6045	0.618362	0.621398	0.625068	0.629049

Table 3.4: Thermophysical properties measured of Al_2O_3/water

Properties	**Al_2O_3**				
Volume concentrations	1%	2%	3%	4%	5%
Density (Kg/m3)	1023.030	1049.060	1075.090	1101.120	1127.150
Viscosity (Ns/m²)	1.09E-03	1.21E-03	1.35E-03	1.53E-03	1.76E-03
Specific heat (J/kg K)	4061.757	3947.481	3838.739	3735.138	3636.322
Thermal conductivity (W/m. K)	0.6602	0.676078	0.693175	0.710985	0.729350

Table 3.5: Thermophysical properties measured of CuO/water

Properties	**CuO**				
Volume concentrations	1%	2%	3%	4%	5%
Density (Kg/m3)	1052.03	1107.06	1162.09	1217.12	1272.15
Viscosity (Ns/m²)	1.09E-03	1.21E-03	1.35E-03	1.53E-03	1.76E-03
Specific heat (J/kg K)	3956.706	3753.81	3570.130	3403.059	3250.443
Thermal conductivity (W/m. K)	0.654035	0.67276	0.691245	0.709812	0.728584

3.2.8 Grid Independence Test

A grid independence test was conducted under multiple hexahedral components to confirm the quality of the result under the balance of mesh size, computation cost, and the need for Y+. After generation of the mesh, it is observed that the cell size at 748,720, 909,160, and 1,195,950 indicated, respectively, 126.1712, 127.1013, and 127.8551 of Nusselt numbers by comparing the independent test inquiry result, demonstrating that the variation between the outcomes is not significant See Table 3.6. The domain of the mesh generation is depicted in Figure 3.8, as well as the Y+ value at different geometrical cross sections and the inlet velocity value of 0.75 m/s, illustrated in Table 3.7. The error percentage is estimated as follows;

$$e\% = \frac{Q - Q_{n-1}}{Q_{n-1}} \quad (61)$$

Table 3.6: Grid independent test

Grid No.	Grid nodes	*Nu*	e %	u (m s-1)	e %
1	748,720	126.1712	-	0.2675	-
2	909,160	127.1013	0.73717	0.2681	0.2243
3	1.195,950	127.8551	0.59307	0.2688	0.2611

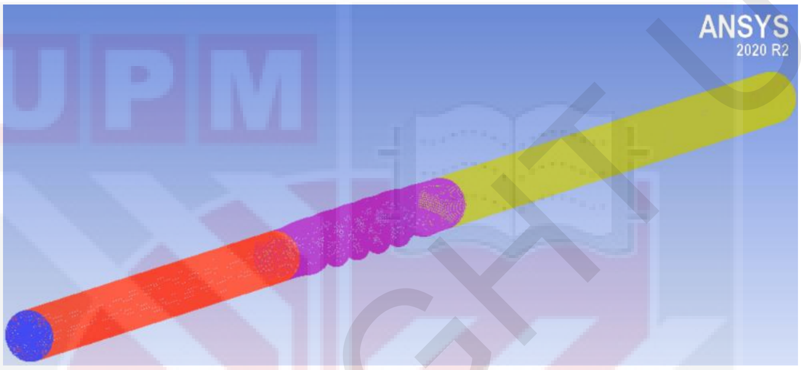

Figure 3.9: The domain of mesh generation at a twisted angle of θ = 360

Table 3.7: The value of Y+ at different geometrical cross sections and inlet velocity value of 0.75 m/s

Twisted angle (degree)	Y+ value		
	Entry section	Lobe swirl	Test section
90	4.14	4.15	3.98
180	3.66	3.69	3.48
270	4.24	4.31	4.04
360	3.67	3.99	4.04
450	4.32	4.42	4.22

3.2.9 Validation of Numerical Study

The primary objective of the current study was to improve the thermal performance of a plain tube. The constant heat flux was subjected to the smooth channel as a test section. Therefore, the validation of the current study used plain tube as the targeted outcome. According to swirl flow, the present study used lobed swirl to generate swirl flow within a smooth channel. The characteristics of swirl flow, heat transfer and PEC resulting from implemented lobed swirl have been investigated inside smooth channels. The friction factor and Nusselt number were compared with the experimental investigation by Jafari et al. (2017b), and many associated correlations were used to validate the current numerical analysis. Therefore, the Nusselt number values were compared with Dittus-Boelter equation (62) and Sieder-Tate equation (63) correlations, while friction factors values were compared with Blasius equation (64), Pertukhov equation (65) and Vatankhah equation (66) correlations. Figure 3.9 shows that the current numerical study result is considered reliable at a relative deviation, respectively 2.47%, 2.6% and 7.6%, with Jafari et al., (2017b) experimental work, Sieder-Tate and Dittus-Boelter. Regarding the friction factor, the numerical result presented a good agreement with the deviation of 3.35%, 8.63%, 8.8% and 3.06%, respectively, compared with Jafari et al., (2017b) experimental work, Blasius, Petukhov and Vatankhah in friction factor.

$$Nu = 0.023 Re_b^{4/5} Pr_b^{0.4} for\ 0.6 \le Pr \le 160\ and\ 10^4 \le Re \qquad (62)$$

$$Nu = 0.027 Re_b^{4/5} Pr_b^{1/3} \left(\frac{\mu}{\mu_s}\right)^{0.14} \qquad (63)$$

Where μ and μs refer to the fluid viscosity at the bulk temperature and the wall surface. The correlation related to the friction factor adopted as the following:

$$f = 0.316 Re_b^{-1/4} \qquad (64)$$

$$f = (0.079\ln(Re) - 1.64)^{-2} \tag{65}$$

$$\frac{1}{\sqrt{f}} = 0.868ln\left(\frac{0.4587Re}{(s-0.31)^{\frac{0.4587Re}{s+0.9633}}}\right) where\ s \tag{66}$$

$$= 0.21Re\frac{\varepsilon}{D} + \ln\,(0.4587Re)$$

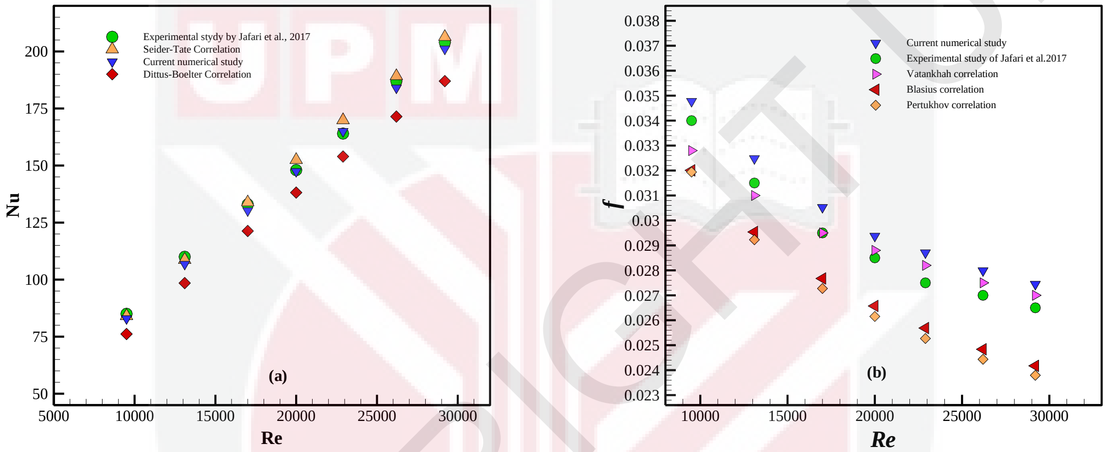

Figure 3.10: Comparison between experimental correlations and current numerical results for a plane tube at (a) Nusselt number and (b) friction facto

3.3 Comparison Between Current Numerical Studies

The motivation behind the present study is to create swirl flow within a smooth channel by placing a 4-lobed swirl generator. Therefore, different numerical studies have been conducted to investigate the impact of a 4-lobe swirl generator on thermal performance. A comparison between the first and the second numerical study is depicted in Table 3.8. It is worth mentioning that the parameters considered in the first numerical study according to the literature. The parameters used in the second numerical study are adopted based on the result of the first numerical study. Due to the high thermal conductivity of nanofluids compared with conventional liquids, SiO_2,

Al_2O_3, and CuO, with volume concentrations ranging from 1% to 5% in water, are used.

Table 3.8: A comparison between the parameters used in current numerical studies

Method of study	First numerical study	Second numerical study
Lobed number	4-lobed swirl generators	4-lobed swirl generators
Twisted angle	θ = 90º, 180º, 270º, 360º and 450º	θ = 360º
Transition part type	β-transition	β-transition
Transition multiplier value	n = 0.25, 0.50 and 0.75 mm	n = 0.25 mm
Variable helix	t = 0.5, 1and 1.5 mm	t = 1 mm (geodesic)
Working fluid	water	SiO_2, Al_2O_3, and CuO/water nanofluid
Reynolds number	30,000 to 55,000	15,000 to 35,000

3.4 Experimental Work

In the current study, there are two experimental works; one is related to the preparation of nanofluid and the other is related to examining a lobed swirl generator at the optimum design that concluded from numerical study

3.4.1 Hybrid Nanofluid Preparation

The current study considers the two-step procedure to create a hybrid nanofluid by dissolving a known quantity of base fluids. This technique was considered because of its low cost and ability to deal efficiently with nanoparticle oxide, which also can be manufactured on a large scale. The current experiment utilised graphene oxide (GO) and copper oxide (CuO) nanoparticles with average diameters of 3.9 nm and 40 nm, respectively. Figure 3.10 demonstrates a scanning electron microscope (SEM) picture of GO and CuO nanoparticles. It is worth mentioning that the estimated particle size before the nanofluid preparation is essential due to the remarkable effect of nanoparticle size on thermal conductivity and heat transfer. Scanning electron microscopy (SEM) is the technique that has been used to evaluate particle size. The signal name is the secondary electron (SE), the most common imaging approach in scanning electron microscopy (SEM). The working distance is 8700 um, which refers to the distance between the top of the scanning electron microscopy device's column and the top of the sample. The nanoparticle size was determined at a maximum magnification of 5000. The GO image clearly shows the particle size distributions measured using the field emission of the SEM machine. According to the CuO image, it can be easy to estimate the particle size using ImageJ software, allowing the user to approximate it with high resolution.

CuO GO

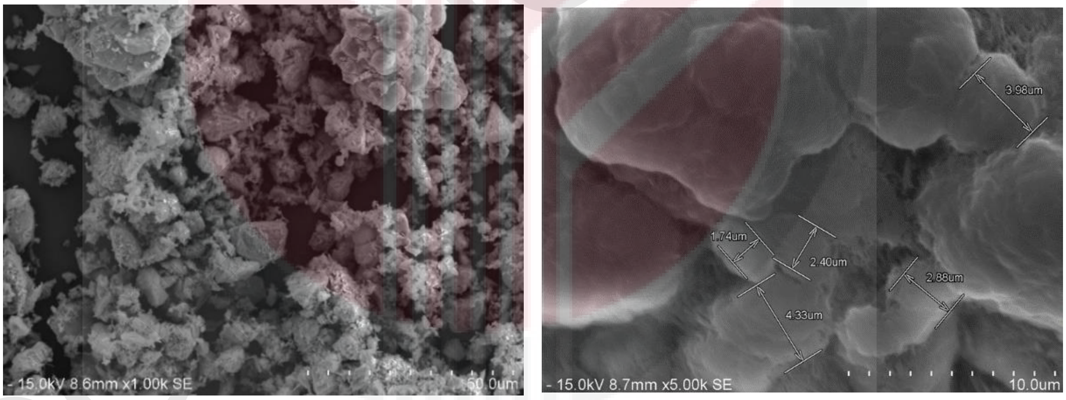

Figure 3.11: SEM image of CuO and GO nanoparticles

The distillate water was considered the base fluid for synthesising GO-CuO nanoparticles. A sensitive balance (Sartorius, M-pact AX224) is used to weigh the nanoparticles with a precision of 0.001g, as shown in Appendix B9. The measurement has been repeated using a calibrated Electronic Balance, as depicted in Appendix B10. Based on different volume concentrations of 0.15, 0.30, 0.45, 0.60 and 0.75% of 80

CuO and 20% GO nanoparticles, the weight of the samples as the first step should be conducted depending on equation (67).

$$\varphi = \frac{\left(\frac{m}{\rho}\right)_{GO} + \left(\frac{m}{\rho}\right)_{CuO}}{\left(\frac{m}{\rho}\right)_{GO} + \left(\frac{m}{\rho}\right)_{CuO} + \left(\frac{m}{\rho}\right)_{mixture}} \tag{67}$$

Where φ,m and ρ represent volume concentration, mass (kg) and density (kg/m3), respectively. At the volume of 100 ml, the measurement of the mass at different volume concentrations is implied in Table 3.9. After determining an adequate weight for the base fluid and nanoparticles, the water and nanoparticle combination is stirred on a magnetic hotplate for one hour, as seen in Appendix B11.

Table 3.9: The volume concentrations of nanoparticles used to make 100 ml of hybrid nanofluid

Volume concentration (%)	Mass [±0.001] (g)	
	GO	CuO
0.15	0.03	0.757
0.30	0.06	1.517
0.45	0.09	2.278
0.60	0.121	3.042
0.75	0.151	3.809

The suspension was treated for 10 hours in a hot bath sonication (Benchtop Ultrasonic Cleaner -SOO347181), as seen in Appendix B12, to avoid the accumulation and sedimentation of hybrid nanoparticles. Longer and stronger ultrasonication has been observed to yield further stable and dispersed nanofluids. Extending the ultrasonication duration and power also leads to increased thermal conductivity, improved heat transfer, reduced viscosity, and decreased pressure drop (Asadi et al., 2019).

3.4.1.1 The Measurement of Thermophysical Properties

The thermophysical properties of GO-CuO/water have been extracted experimentally at a variation of solid volume fraction of 0.15, 0.30, 0.45, 0.60, and 0.75%. Several related equipment have been adopted in this investigation. Density is the mass of the substance you can have in a volume. It simply calculates the density by dividing the well-known mass and volume. A vibro viscometer (AND SV-100-Japan) with a range (of 0.3 to 10,000 mPa.s) and an accuracy of 0.1% was used to evaluate the viscosity; the calibration certificate is shown in Appendix B13.

As indicated in Appendix B14, the KD2-pro device has been used to determine the thermal conductivity of the samples under various volume concentrations. The device works at a thermal conductivity range from 0.2-2 W/ m.K with a sensitive needle at the accuracy of ±5 % W/m k. The device can work from (-50 to +150ºC) according to temperature effects. The specific heat has been determined by applying differential scanning calorimetry (DSC) at temperatures ranging from -100 to +450 ºC. The average time value is considered to ensure the accuracy of the thermophysical characteristic measurement result. The thermophysical properties obtained have been listed in Table 3.10.

Table 3.10: Thermophysical properties measured of GO-CuO/water at a temperature value of 50 ºC

Properties	Water	GO-CuO/water 0.15 %	GO-CuO/water 0.30 %	GO-CuO/water 0.45 %	GO-CuO/water 0.60 %	GO-CuO/water 0.75 %
Density (kg/m3)	997.31	1005.25	1010.75	1024.51	1038.27	1052.03
Viscosity (Pa.S)	0.001003	0.001016	0.001032	0.001043	0.001054	0.001068
Thermal conductivity (W/m.K)	0.648246	0.7074	0.7148	0.7193	0.7235	0.7264
Specific heat (J/kg.K)	4182.61	4146.63	4123.37	4066.32	4010.76	3956.7

3.4.1.2 Measuring Technique of Thermal Conductivity

3.4.1.2.1 Validation of the KD2-Pro Measurement

Due to the importance of water as a working fluid in the current study, it was used as a calibrated fluid to validate the reliability of the KD2-Pro as the primary measurement of thermal conductivity, which is considered the crucial parameter for improving heat transfer. Therefore, a comparison between the water experimental data proposed by ASHRAE (2015) and the current measurement has been conducted as described in Figure 3.11. By comparing the average value between both experimental measurement data, the result presented a good agreement with a deviation percentage of 2.57%.

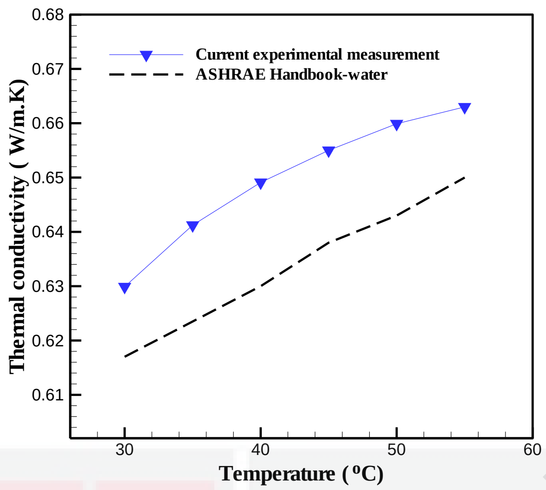

Figure 3.12: Comparison between current experimental measurement of water with the data proposed by ASHRAE Handbook-water (ASHRAE, 2015)

3.4.1.3 XRD-diffraction

X-ray diffraction analysis (XRD) determines a material's crystallographic structure in materials science. XRD first subjects the substance to incident X-rays to quantify the intensities and scattering angles of the X-rays. As seen in Figure 3.12, the X-axis refers to the variation of the angle (2θ), while the Y-axis illustrates the different intensities and the peak is not sharp; these peaks have some width. The limited size of the crystals causes the peaks in the XRD patterns to widen. The peaks in the XRD pattern will seem extremely sharp if the crystal is infinitely large, and peak broadening will rise as the crystal's size decreases. The unit cell's atomic distribution may be inferred from the peak relative intensities, while the XRD patterns reveal details on the size and defects of the particles. The material's crystal structure will be characterized by XRD pattern analysis and diffraction peak analysis.

3.4.1.3.1 Estimate GO &CuO Particle Size

Limiting nanoparticle accumulation and stability in the medium is a target required during the nanofluids' synthesis (Safiei et al., 2020). Consequently, the shape and the size of the nanoparticles are assessed using the analytical technique of X-ray diffraction (XRD). In materials science, X-ray diffraction analysis (XRD) is used to figure out a material's crystallographic structure. XRD first subjects the substance to incident X-rays to quantify the intensities and scattering angles of the X-rays. These peaks have higher intensities because there is more remarkable periodicity in some directions than in others.

As shown in Figure 3.12, the observation of X-ray diffraction (XRD-data) results under different peaks has been created using OriginLap software.

Lab software. It is worth mentioning that the relationship between the peak width and the crystallite size is inversely proportional (He et al., 2018). As a result, a decrease in crystallite size led to an increase in peak width and vice versa. To determine the particle size of GO and CuO, the well-known equation Debye-Scherrer has been considered, which can be written as follows;

$$D = \frac{K\lambda}{\beta cos\theta} \quad (68)$$

Where D is referred to crystallite size (nm), while k and λ are represented by the Scherrer constant of 0.9, X-ray wavelength = 0.15406(nm), the other parameters of β, which refers to full-width half maxima (FWHM) (radians) and θ, which relates to diffraction angle (radians) are evaluated using OriginLab software. The outcomes are illustrated in Table 3.11. In general, it can be proved that the GO and CuO have typical particle sizes of 3.19 and 45.91nm, respectively.

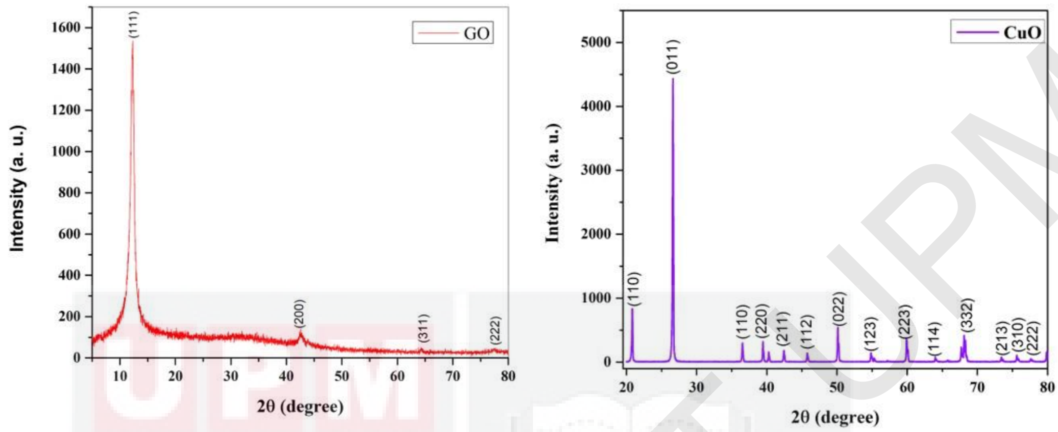

Figure 3.13: X-ray diffractometer result for the Graphene oxide and silicon dioxide nanoparticles

Table 3.11: Calculate the average particle size of the GO and CuO nanoparticles

K	λ	Peak position 2θ (°)		FWHM β (°)		D (nm)	
		GO	CuO	GO	CuO	GO	CuO
0.94	1.5406	12.22192	20.83919	0.99931	0.15438	8.35	54.65
0.94	1.5406	42.65294	26.63519	1.34478	0.15314	6.62	55.68
0.94	1.5406	62.2015	36.54554	60.52228	0.17557	0.16	49.77
0.94	1.5406	82.62507	39.47711	21.29759	0.1783	0.52	49.44
0.94	1.5406	-	40.29647	-	0.17051	-	51.83
0.94	1.5406	-	42.45653	-	0.1912	-	46.56
0.94	1.5406	-	45.80033	-	0.19495	-	46.20
0.94	1.5406	-	50.14921	-	0.21585	-	42.44
0.94	1.5406	-	54.87983	-	0.23509	-	39.77
0.94	1.5406	-	59.97459	-	0.25502	-	37.56
0.94	1.5406	-	64.01738	-	0.13125	-	74.55
0.94	1.5406	-	68.13315	-	0.62645	-	15.99
0.94	1.5406	-	73.47526	-	0.29279	-	35.36
0.94	1.5406	-	75.68483	-	0.31982	-	32.85

3.4.1.4 Experimental Rig Design

The experimental setup and the procedures required for successful set-up are presented in this section. The test section, as the most essential part and the experiment method utilized in this investigation are described in detail. A hybrid nanofluid of GO-CuO /water was employed as the working fluid in the current experimental study; its thermophysical properties and the instruments that were used have been discussed. Furthermore, the data reduction process and experiment measurement uncertainties are discussed. The experimental setup for examining the heat transfer and fluid flow over a lobed swirl generator and its entry and test section is depicted in Figure 3.13 and Figure 3.14. The overall parts and instruments used in this investigation are an electrical heater plate (electrical helical coil), insulator, thermocouples (Type-K); data logger, PC, test section, pressure gauge, multimeter; power regulator, chiller, water pump; valve, and flow meter.

3.4.1.4.1 The Entry Section and Test Section

The current study also performed experimentally the impact of a placed lobed swirl device and its transition parts before a stainless-steel tube on thermal performance and the flow field. The experimental study is based on the four-lobe device, which was fabricated at a length of 0.2 m, equivalent diameter of 0.05 m and twisted angle of 360°, while the transition part was manufactured at a length of 0.1m, equivalent diameter of 0.05 m and angle was progressively turned from (45º to 90º). All the parameters of the lobed swirl generators were adopted as optimal factors based on (the outcome of the current Numerical study and) the study of (G. Li et al., 2015b).

The entrance section was fabricated from PVC material with a 5 mm thickness and extended to 0.8 m to ensure the turbulent flow at a fully developed. The stainless-steel test section was formed with the following measurements: 1 m in length, 0.05 m in diameter, and 1 mm in thickness. An electrical helical coil around the test part linked to a multimeter and a power regulator was employed to maintain a constant heat flux. A digital multimeter (BK PRECISION, 2831E) was attached to the heater's electrical circuit, which was used to measure the voltage and current transmitted to the heater with an essential output power of DC with an accuracy of 0.03%. A 1260C ceramic fiber blanket insulator surrounds the test tube to avoid heat loss.

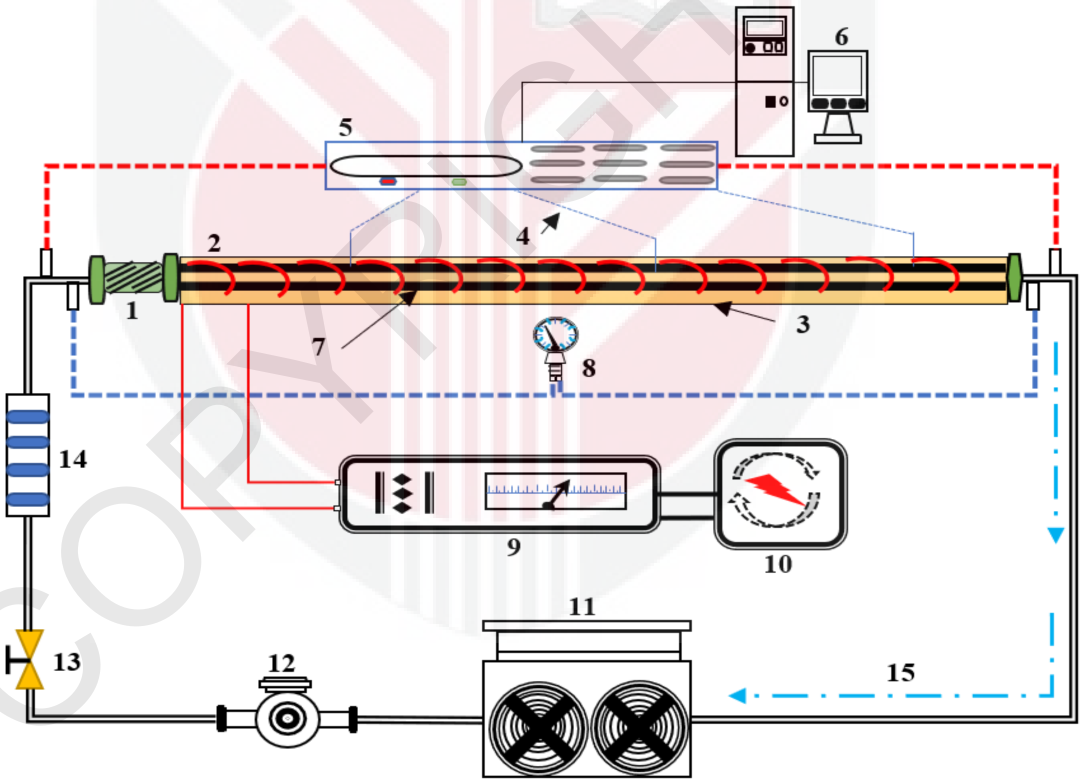

1- Lobe swirl generator; 2- electrical helical coil; 3- Insulator; 4- Thermocouples; 5- Data logger 6- PC; 7- Test section 8- Pressure gauge; 9- Multimeter; 10- Power regulator; 11- chiller 12- Water pump; 13- Valve; 14- Flow meter; 15- Flow direction

Figure 3.14: Schematic experimental setup

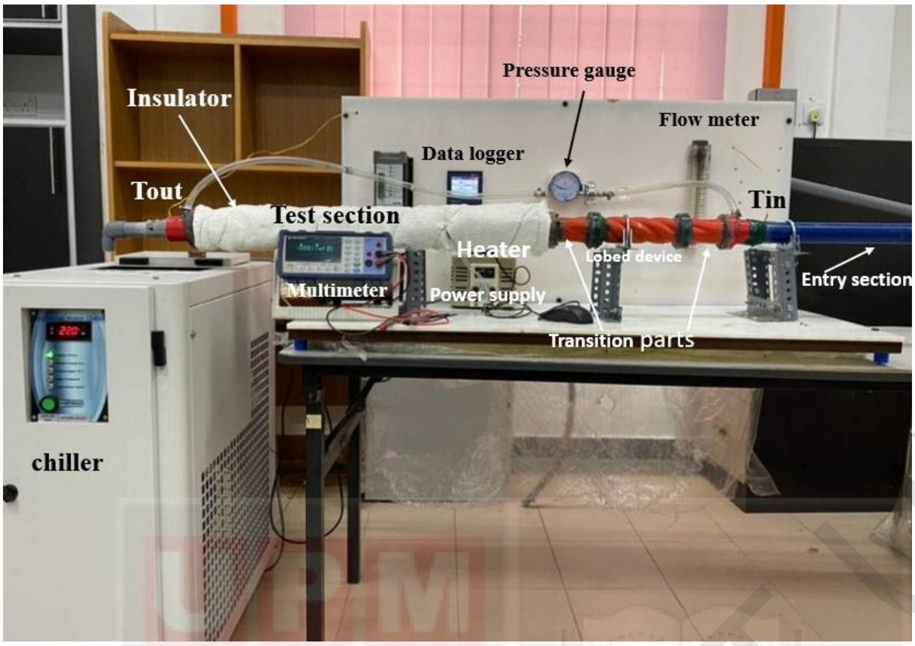

Figure 3.15: Photo representation of the experimental setup

3.4.1.4.2 Thermocouples

In the current study, several thermocouples (Type-K) are considered to measure the temperature of fluid flow and the surface of the test section, as illustrated in Figure 3.15. As the most essential device, all thermocouples are calibrated using a Temperature Calibrator Model (CL3512A); the device and the calibration certificate are depicted in Appendix B1. Fourteen calibrated K-type thermocouples were positioned around the test area at three locations to monitor the surface temperature. Twelve thermocouples clamped along the test section to determine the wall temperature surface.

Three places along the tube test section to insert thermocouples have been adopted. Four thermocouples were positioned in each place to investigate the characteristics of swirl flow. No thermocouples were immersed in the fluid to avoid the water being disturbed and to ensure an accurate result. Also, two calibrated thermocouples have been inserted at 1 mm depth at the inlet and the outlet of the system to measure the fluid temperature. The disturbance of the water at the inlet position is negligible due to the small depth of the thermocouple inserted and the turbulent flow that is fully developed. Each of the thermocouples that is being used has an identical 0.5 mm diameter. Once the reading of the measurements reached a steady state condition, the data were gathered. A steady state is achieved Whenever the pressure and temperature measurements are stable for at least five minutes. The average temperature of the fluid (bulk temperature) and the average surface temperature are taken into account to estimate convective heat transfer. To efficiently transfer heat from the tube surface through the thermocouple to the data logger device, high-temperature & conductive paste (OT-201-16-USA) was applied around each thermocouple. All thermocouples were attached to a data logger (SIMEX, CMC-99 MultiCon) to determine the temperature value at different places.

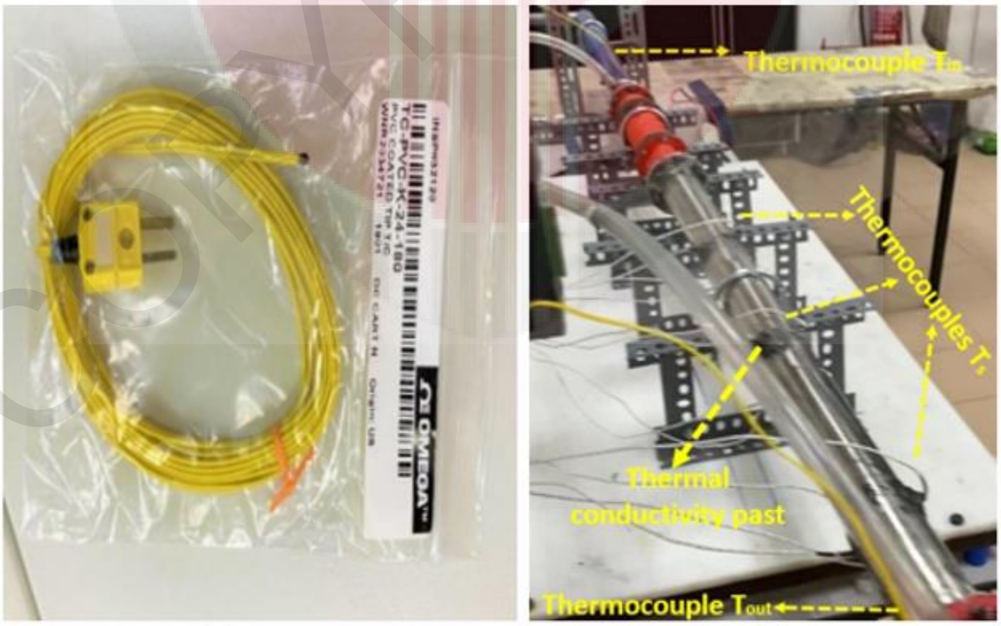

(a) (b)

Figure 3.16: a) thermocouples type-K, b) thermocouples fixation using high thermal conductive paste

3.4.1.4.3 Electrical Heater and Power Regulator

An electrical heater was built on the tube to generate a constant heat flux around the wall of the test section. The wires were linked to a power source to provide heat flux to the heater plate (electrical helical coil), as shown in Appendix B2. The power supply has a controller to provide the heater's current and voltage (0 to 272 V). The electrical circuit of the heater was linked to a digital multimeter (BK PRECISION, 2831E), as depicted in Appendix B3, to measure the voltage and current supplied to the heater with essential V dc precision up to 0.03%.

3.4.1.4.4 Water Chiller

An industrial water chiller (SPH20N with a Temperature Accuracy of 2°C), as seen in Appendix B4, has been used to control the working fluid's temperature at the desired value. The industrial water chiller consists of a fluid tank, a condenser, a helical cooling coil, a pump, and a compressor. From a tank of 20L capacity, a pump of 0.5 H pumps the working fluid toward the system. Due to the high Reynolds number, the pump was attached to another pump parallelly (to increase the flow rate). The flow rate of the pumping fluid was modified using a bypass line with a valve. The advantages of the chiller are its 2400 kcal/h cooling capacity and its ability to precisely regulate the working fluid temperature to the desired value with an (accuracy of ± 0.2°C). At the test section's inlet, the working fluid temperature was 19ºC.

3.4.1.4.5 Measurement Instrument

Several variables have been investigated in order to assess the lobed swirl generator's performance inside the test section, such as the temperature variation of the working fluid, the differential pressure, and the flow rate. As illustrated in Appendix B5, a differential pressure gauge is used to detect the differential pressure drop between the test section's inlet and exit with an accuracy of 0.5%. The pressure gauge can support an upper temperature of 65 °C and a working pressure of 160 mbar. To measure the variation in the temperature over the test section, fourteen thermocouple k-type (TC-PVC-K-24-180) with error ± (1.1ºC) or ± (0.4%) reading above (100 ºC) Appendix B6 were connected to a data logger (SIMEX, CMC-99 MultiCon). Appendix B7 depicts the data logger. DAQ manager software was connected to a data logger to simplify the process. This data logger is supported by a reading accuracy adjustments feature between one to four decimal places. Therefore, two decimals are considered in the current experimental work. A flow rate instrument was equipped between the chiller and the inlet section to monitor how much liquid is induced within the pipe (mass flow rate). The flow rate device adopted in this study is Tofco FC-SD85L-L200, with a 20-200 LPM measurement range and an accuracy of ± 0.5% FS, as shown in Appendix B8.

3.4.1.4.6 Experimental Procedure

Due to the importance of working fluid, the storage tank of the chiller was filled before turning on the chiller to pass the fluid within the system. The system remains operational for brief periods upon turning on the pump to attain stability. The flow rate is then controlled using the various available valves (bypass and control valves). A flow meter was implemented to measure the flow rate at a given Reynolds number value.

Next, the power supply is turned on to ensure heat flux around the test section of the tube. The electric current should be provided via a voltage stabilizer to heat the test section and maintain the wall under a constant heat flux using a digital multimeter. The inlet and outlet temperatures and all surface temperatures transmitted thermocouple k-type (TC-PVC-K-24-180) with a particular limit of error ± (1.1ºC) or ± (0.4%) reading above (100 ºC) are measured using a data logger. A differential pressure gauge monitors the pressure losses through the test section. The same procedure was repeated during each case, with the Reynolds number and working fluid changed. To make the nanoparticles homogenous and to avoid aggregation and sedimentation during experimental work, many techniques have been adopted, such as hot plate magnetic stirring and sonication bath for ten hours to decrease the cluster and the size of agglomerated particles (Hwang et al., 2008), also the particle size of GO is tiny (3.9 nm). The volume concentration amount adopted (0.0015 to 0.0075) results in stable suspension. Between each two-step of the experimental process, to avoid results bias, the tank is cleaned with pure water and switched on the system to expel the remaining nanoparticles in the pump and tubes to ensure proper nanoparticles are chosen for the following process. We avoid using the surfactant technique due to its negative effect on thermal conductivity improvement. Also, a two-step method was employed to make the synthesis suspension (Hilo et al., 2020b). The steady state was ensured after the temperature and pressure gauges were monitored and all experimental data were gathered.

3.4.1.4.7 Data Reduction

The constant heat flux generated by the electrical power via the plate heater can be calculated using the simplified steps as follows:

$$Q_e = V \times I \tag{69}$$

The heat transfer generated by the working fluid is defined as:

$$Q_f = \dot{m}Cp(T_{out} - T_{in}) \tag{70}$$

It can simply calculate the mass flow rate as a function of the Reynolds number, working fluid viscosity and the diameter of the geometrical cross-section using the following equation:

$$\dot{m} = \frac{Re\mu\pi D}{4} \tag{71}$$

It can calculate the volume flow rate using the following formula:

$$\forall = \frac{\dot{\boldsymbol{m}}}{\boldsymbol{\rho}} \tag{72}$$

Where ∀ is the volume flow rate (m3/s), $\dot{m}$ mass flow rate (kg/s) and ρ density (kg/m3)

$$Re = \frac{u_{ave} D_h}{v} \quad (73)$$

$$u_{ave} = \frac{\dot{m}}{\rho A_c} \quad (74)$$

$$A_c = \frac{\pi D^2}{4} \quad (75)$$

Where Ac represents the cross-sectional area through which the working fluid flows

$$D_h = \frac{4A}{P} \quad (76)$$

For more accuracy, Eq. (58) was used to determine the average value between the heat flux provided by electrical power (Qe) and the heat transfer generated by the working fluid (Qf) (Tang et al., 2015a).

$$Q = \frac{Q_e + Q_f}{2} \quad (77)$$

The heat transfer between the test section and the internal flow is considered by convection. Therefore, the following equation was adopted to determine the convection heat transfer coefficient:

$$Q = h_{ave} A_s (T_s - T_b) \quad (78)$$

Where Tw and Tb refer to the temperature of the wall and bulk temperature, respectively, the average temperature of the wall (Tw) and fluid (Tb) can be evaluated using Eqs. (62) & (63), respectively. The average of the four recorded temperatures at each axial location along the test section determines the temperature (Tw).

$$T_w = \frac{Sum\ of\ surface\ temperture\ observation}{Total\ number\ of\ observation} \tag{79}$$

All working fluid's properties were determined based on the bulk temperature, and bulk temperature can be evaluated as follows:

$$T_b = \frac{T_{in} + T_{out}}{2} \tag{80}$$

$$h_{ave} = \frac{q''}{(T_{s_{ave}} - T_{b_{ave}})} \tag{81}$$

Due to the wall being subjected to constant heat flux,

$$q'' = \frac{Q}{\pi DL} \tag{82}$$

$$Nu_{ave} = \frac{h_{ave} D_h}{k} \tag{83}$$

The friction factor can be obtained by measuring the pressure drop along the test section using the following formula:

$$f = \frac{\Delta P}{(L/D)\left(\frac{\rho u_i^2}{2}\right)} \tag{84}$$

To investigate the applicability of the system in terms of thermal performance, Performance Evaluation Criteria (PEC) take place in this study using the following formula:

$$PEC = \frac{Nu/Nu_p}{\left(f/f_p\right)^{1/3}} \tag{85}$$

Where Nu and Nup are the Nusselt numbers after enhancement and at the plane tube, respectively, while f and fp are the friction factor after enhancement and at the plane tube, respectively

3.4.1.4.8 Uncertainty Analysis

Experimental studies without an assessment of uncertainty are no longer sufficient. It is known that the uncertainty percentage of the parameters measured depends on the type of device used and the related equation of each variable. Consequently, the error was determined by utilizing the Kline and McClintock method (Kline & McClintock, 1953). Analyses are carried out to calculate the experimental uncertainties of the parameters that were obtained from the data reduction, such as Nusselt number (*Nu*), friction factor (*f*), and Reynolds number (Re) (Hilo et al., 2020a). The differential approximation approach was considered to determine the uncertainty level in a result Rs, which is a function of the independent parameters X1, X2, X3..., Xn. Therefore:

$$R = R(X_1, X_2, X_3, \dots \dots \dots \dots, X_n \tag{86}$$

Where X1, X2, …. Xn and R are independent and dependent parameters. As a result, the following formula can be used to determine the uncertainty (R):

$$W_R = \pm\sqrt{\left(\frac{\partial R}{\partial X_1} W_{X_1}\right)^2 + \left(\frac{\partial R}{\partial X_2} W_{X_2}\right)^2 +, \dots \dots \dots \dots \dots, \left(\frac{\partial R}{\partial X_n} W_{X_n}\right)^2} \tag{87}$$

The above technique assesses the experimental error value for several computed variables. The absolute values are considered to attain the highest level of absolute uncertainty in the WR result since the number of values in the equation above and the errors in the measurement parameters can be positive and negative. In Appendix B, the mathematical estimation of the uncertainty is displayed, and Table 3.12 provides an overview and presentation of the range of uncertainty of Reynolds number, heat flux, heat transfer coefficient, Nusselt number, and friction factor. In addition, all other parameters were found to be less than 5%, proving that the experimental work's reliability presented a precision level acceptable for the instruments in use.

Table 3.12: Summary of uncertainty analysis

No	Parameters	Uncertainty error (%)
1	Reynolds number, Re	2.030 (2.003)
2	Heat flux, q	2.003 (2.030)
3	Heat transfer coefficient, h	0.232
4	Nusselt number, *Nu*	7.787
5	Friction factor, f	2.441

3.4.1.5 Verification of Experimental Work

Correlations between the Nusselt number and the friction factor over the plane tube were carried out to assess the validity of the current experimental investigation. Regarding the Nusselt number, the Dittus-Boelter equation (34) and the Sieder-Tate equation (35) were considered. As shown in Figure 3.16 (a), there was a good agreement with a deviation of 3.63% and 9.83%, respectively, between the current experimental study and the correlations proposed by Dittus-Boelter and Sieder-Tate. Moreover, Figure 3.16 (b) demonstrates the reliability of the current experimental study in terms of the friction factor perspective. The working fluid is water, and thermophysical properties are calculated at a mean bulk temperature of 25ºC.

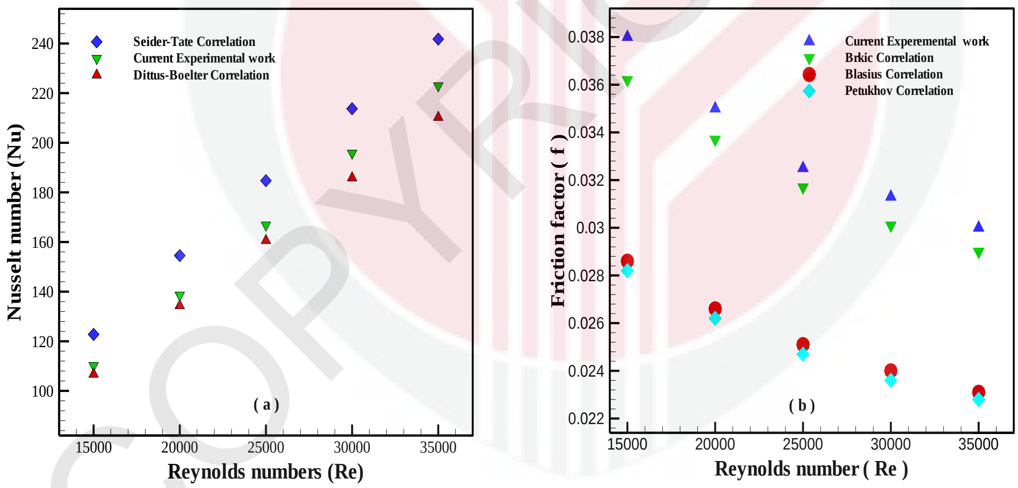

Figure 3.17: Experimental study of verifying current experimental work versus different correlations over the plane tube. (a) Nusselt number (b) Friction factor

The comparison between the present experimental approach and the correlations suggested by Brkic equation (88), Blasius equation (36) and Petukhov equation (38) presents a reliable result with acceptable precision of 2.46%, 22.12% and 24.12%, respectively. Consequently, it can be proved that the experimental friction factor and heat transfer observations were reliable.

$$\frac{1}{\sqrt{f}} = -2log\left(\frac{\varepsilon}{3.71D} + \frac{2.18S}{Re_b}\right) \; when \; S = ln\left(\frac{Re}{1.816\frac{1.1Re}{(1+1.1Re)}}\right) \tag{88}$$

CHAPTER 4

RESULTS AND DISCUSSION

4.1 Overview

In this chapter, the numerical and experimental results of the study have been discussed in detail. The target outcome of this study is to perform the impact of a four-lobe swirl generator equipped with a circular smooth tube as a test section on heat transfer and fluid flow. The effect of the four-lobe swirl device and its attractive transition part has been numerically investigated as follows:(i) the impact of the four-lobe swirl generator under different angles of (θ = 90º, 180º, 270º, 360º and 450º), (ii) the transition parts were studied under different effective parameters of multipliers factor (n= 0.25, 0.5, 0.75 mm) and the variable helix (t = 0.5, 1, 1.5 mm) and (iii) the working fluid adopted is water with a Reynolds number ranging between (30,000 – 55,000). The second numerical study was performed at the fixed twisted angle at 360º as the optimum case. At the same time, the working fluid used is different nanofluids of SiO_2, Al_2O_3, and CuO with volume concentrations of (1 to 5%) at a variation of Reynolds number Ranging between 15,000 to 35,000. Finally, the experimental work was also conducted at the fixed lobed swirl generator at (θ = 360º) and applied a GO-CuO/water hybrid nanofluid as a working fluid and a variation of volume concentration of (0.15 to 0.75%) at a Reynolds number of 15,000 to 35,000.

4.2 The Impact of Twisted Angles

The first numerical result is aimed at investigating the impact of a lobed swirl generator under different twisted angles (theta = 90, 180, 270, 360 and 450) and examining the transition partis at efficient parameters such as; transition multiplier (n

= 0.25, 0.5 and 0.75 mm) as well as transition variable helix at the parameters of (t = 00.5,1and 1.5 mm) on heat transfer and thermal performance. The working fluid adopted in the first numerical study is water.

4.2.1 The Effect of Twisted Angles on Thermal Performance

A smooth channel's flow pattern is mainly straight with slight flow fluctuation, which results in an ineffective transfer of heat. Therefore, the current study aimed to implant a lobed swirl generator before a straight, circular tube to induce swirl flow within the channel. This part of the study related to the first objective, which focused on the impact of a lobed swirl generator under different twisted angles of (θ= 90º, 180º, 270º, 360º and 450º) and the Reynolds number in the range of 30,000 to 55,000 using water as a working fluid on heat transfer and friction factor numerically (First numerical study). The Nusselt number, along with different twisted angles of 90º, 180º, 270º, 360º, and 450º compared with the plain tube (without lobe swirl generator) at various Reynolds numbers, is presented in Figure 4.2(a). For all cases investigated, heat transfer increases with an increase in twisted angle. Compared to a smooth channel, the result proved that the flow pattern is rotational, which is considered the main reason for improved heat transfer within the straight, circular tube (test section) under different lobed twisted angles. The result proved the capability of a lobed swirl generator in promoting heat transfer inside the circular, straight tube under different twisted angles.

A lobed swirl generator with a twisted angle 360º showed more outstanding heat transfer than all the lobes' twisted angles investigated. Nusselt number for the lobed swirl generator at 360º is higher by about 28.78% compared with a plain tube. It can explain the result by the ability of lobed swirl generator at the twisted angle of 360º and high Reynolds number to produce swirl flow intensive near the wall and improve the flow between axial flow at the core and tangential velocity adjacent to the wall. However, the lowest heat transfer associated with a twisted angle of 450º was found. The minimum values of the Nusselt number at $\theta = 450^{o}$ are due to the extreme drop-sharp of this twisted angle, which decreases the swirl flow area of the lobed swirl generator, lead poor vortex flow compared with other twisted angles examined. In other words, it can be attributed to the highly sharp slope at this angle that caused flow obstruction, leading to a reduction in swirl flow. The result also proved that, for each Reynolds number given, the Nusselt number declined with the decrease in the twisted angle, and the greater the twisted angle, the augmentation enhancement in heat transfer, unlike angle 450º. From the obtained result, it can be concluded that the heat transfer enhancement technique within a smooth channel is based on the value chosen for the twisted angles of lobed swirl generators and the range of the Reynold numbers.

As shown in Figure 4.2(b), the friction factor due to the lobed swirl generator at a twisted angle of 360º is higher by the value of 17.35 % than those in the lobed swirl generator under the twisted angles of 90º, 180º, 270º and 450º compared with a plain tube. The result proved that the increase in the Reynolds number led to a decrease in the friction factor, indicating that the Reynolds number and the twisted angle are the main factors affecting the flow rate. These combined effects of Reynolds numbers and the twisted angle of an extended test section (Circular tube) may be attributed to the changes in vortex intensity that we expected. An augmentation in the vortex intensity led to more intensive fluid and raised the pressure drop. An increase in the twisted angle caused a continuous increment in the shape circumference, leading to additional friction loss.

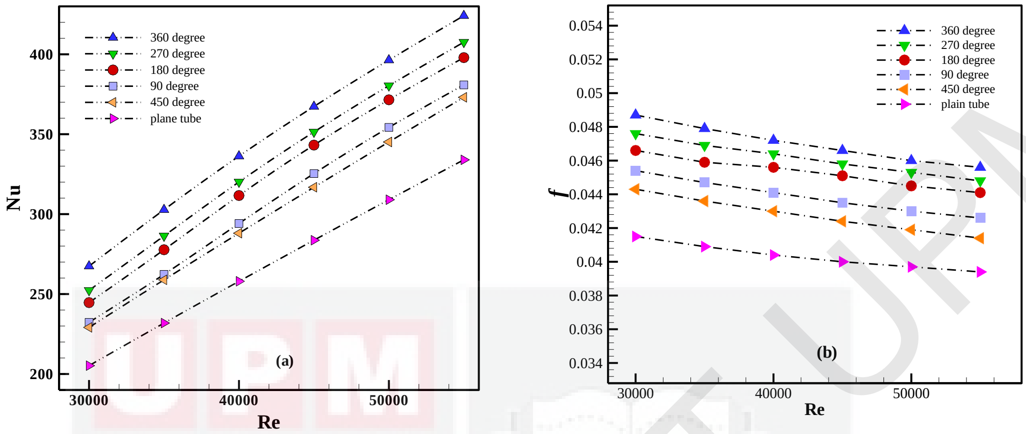

Figure 4.1: Numerical approach of the impact of several twisted angles on (a) heat transfer and (b) friction factor at a different range of Reynolds numbers using water as working fluid

The balance between the increase in Nusselt number and the increase in friction factor is considered to see how the different twisted angles and pressure drop affect heat transfer. Therefore, *Nu/Nup* and *f/fp* values are investigated at a different Reynolds number. According to the outcome, using swirl generators under different twisted angles caused an enhancement in heat transfer value *Nu/Nup* by a factor of about 1.12 to 1.332 when the minimum and maximum values of *f/fp* are 1.1 to 1.346 among all investigated case studies. Moreover, the result showed the highest heat transfer value with the twisted angle of (θ = 360º) and Re of 35,000. The result is highly consistent with Jafari et al.'s (2017b) observation.

The relation between the Nusselt number of the system after enhancement *Nu* to the Nusselt number of the plain tube *Nup* and the relation between the friction factor after enhancement f to the friction factor of the plain tube fp are essential factors that can help in determining the thermal performance of the system. As shown in Figure 4.3(a), the highest value of Nusselt number *Nu/Nup* was obtained at a low Reynolds number of 35,000, which proved the better swirl flow and good flow fluctuation between the core (cold water) to the wall (hot water) occurred at this value. The slight decline in heat transfer in high Reynolds numbers can be attributed to the decrease in a longitudinal vortex induced by the other twisted angles due to the gradual change of the exit transition part from a lobed shape to a circular cross-section. The other reason can be attributed to increased swirl decay due to decreased twisted angles as expected; the lobed swirl generator at the twisted angle of 360º, which refers to the pitch-to-diameter of 8 as the optimum design recommended by many researchers, led to an increase in overall swirl intensity and a decrease in the swirl decay (C. Ariyaratne & Jones, 2007). According to the result illustrated in Figure 4.3(b), the relation between the friction factor and the range of Reynolds numbers adopted is nonlinear. A slight increase in friction factors was obtained at the Reynolds numbers of 40,000 and 50,000 while the other value trend declined. It is worth mentioning this observation is consistent with the findings of (Jafari, Farhadi, et al., 2017b)

The performance evaluation criteria (PEC) technique is used to estimate the relative thermal performance when frictional losses are combined with heat transfer augmentation under the restriction of the same pumping power (Tanda & Satta, 2021). The system's performance in a thermal application is evaluated by considering the equilibrium between the friction factor and heat transfer values. Therefore, the performance evaluation criteria (PEC) technique is applied. If the value of PEC is greater than 1, the heat transfer improvement is higher than the friction factor and vice versa. If the PEC is more prominent than one, it reveals that the improvement in heat transfer is more significant than the effect of the friction factor (Hilo et al., 2020a). The increase in Re with the rise in twisted angle can limit the thermal performance due to the augmentation of the friction factor. Figure 4.4 depicts the thermal performance of the test section (straight, circular tube) equipped with lobed swirl generators under different twisted angles from (90º to 450º). The Reynolds number in the range of 30,000 to 55,000 uses water as a working fluid are considered. The result showed that the highest thermal performance of the system indicated at a Reynolds number of 35,000 is 1.21. The outcome showed a polynomial relation between the twisted angles and the given values of the Reynolds number. Also, the result is consistent with the findings of (Jafari, Farhadi, et al., 2017b).

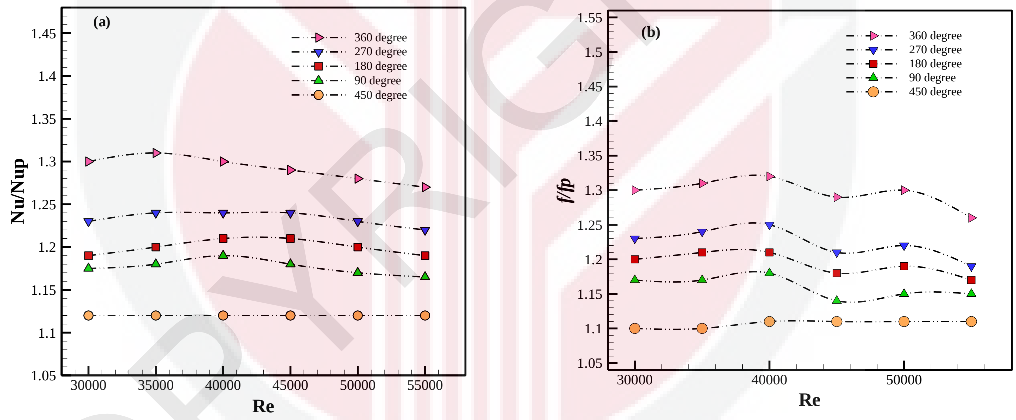

Figure 4.2: Numerical approach of the variation of Reynolds number versus (a) the ratio of Nusselt number *Nu/Nup* and (b) the ratio of friction factor *f/fp* using water as a working fluid

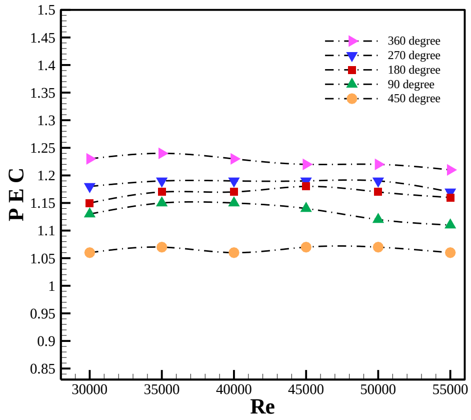

Figure 4.3: Numerical approach of thermal performance value at different twisted angles and Reynolds number using water as a working fluid

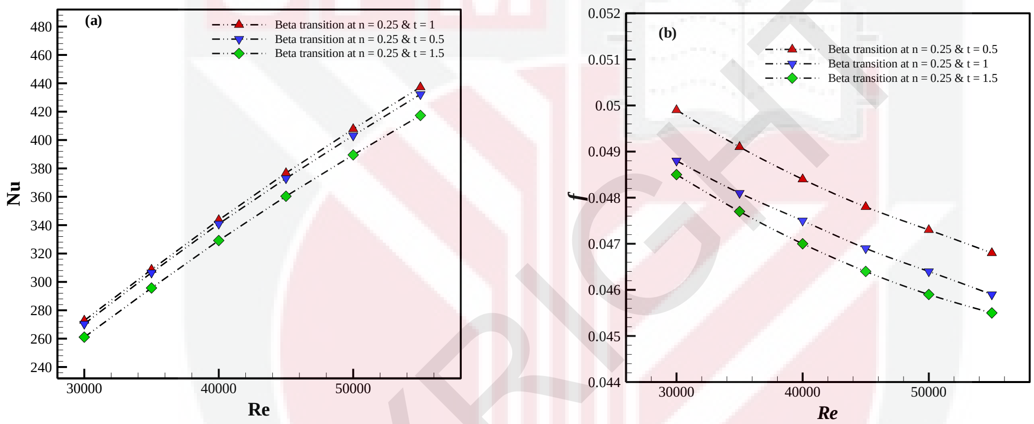

Figure 4.4: Numerical approach of the effect of Beta transition at multiplier (n = 0.25), lobed swirl angle (θ = 360o), and different Helix variable (t = 0.5, 1, 1.5) on (a) heat transfer (b) friction factor using water as a working fluid

4.2.2 Tangential and Axial Velocities Pattern

The lobed swirl device has a curvature cross-section leading to the centrifugal force generated toward the test tube downstream, causing a vigorous tangential velocity to form near the wall as well as an axial velocity concentrated at the core. The swirl circulation path line downstream of the swirl pipe is seen in Figure 4.8. Based on the contour, the swirling pipe created four vortical flow areas that were more pronounced at the twisted angle 360, where the flow rotated around the curved axis and had an inverse relationship with the distance of the test section. In other words, the swirl formed stronger at the beginning of the pipe and gradually faded at the end of the tube downstream. The contour proved the ability of the four-lobe swirl generator to produce azimuthal velocity noticeable around the wall under different twisted angles. The tangential velocity is zero at the tube centre, increasing as it gets closer to the wall and decreasing again to zero when it directly contacts the wall. The contours showed a precise quadrangular shape near the entrance of the lobe swirl. They gradually faded towards the test tube exit, representing a characteristic of a four-lobe swirl device. From the axial velocity perspective, the highest axial velocity is concentrated in the core and decreases as the tube distance increases for all twisted angles investigated. In comparison between the twisted angles, it is worth mentioning that the twisted shape is more pronounced with the angle of 360º instead of 90º for both velocities. Therefore, it produces more flow fluctuation and heat transfer enhancement. The contour showed the flow pattern inside a straight, circular tube (test section). The swirl flow created by mixing tangential and axial velocities is depicted inside a smooth channel, which is expected to improve convection heat transfer within the tubes of a heat exchanger. From the thermal performance perspective, better heat transfer occurred with a low axial velocity concentration in the tube's core line with well-dispersed flow (Jafari, Farhadi, et al., 2017b). The outcomes demonstrate how the four-lobe swirl generator produces a four-sided velocities field. Compared with a lobed swirl generator under a twisted angle of 90, the flow is more pronounced in the core in the case of a lobed swirl generator at 360 degrees, suggesting intense momentum transfer between the fluids at the lobed wall area and the core fluids. Meanwhile, the tangential velocity in LSG at a twisted angle of 360 is greater than that of LSG at 90 degrees, which can be attributed to the fact that the lobed swirl generator at θ =360 presents higher azimuthal velocity leading to an improved temperature gradient between the wall (hot region) and the core (cold region). The CFD outcome also proved that the four-lobed swirl generator has two distinctive types of flow. One is called lobed flow (tangential velocity), which is concentrated adjacent to the wall (green colour). The other flow, named core flow (axial velocity) which is concentrates at the centre (Red colour)

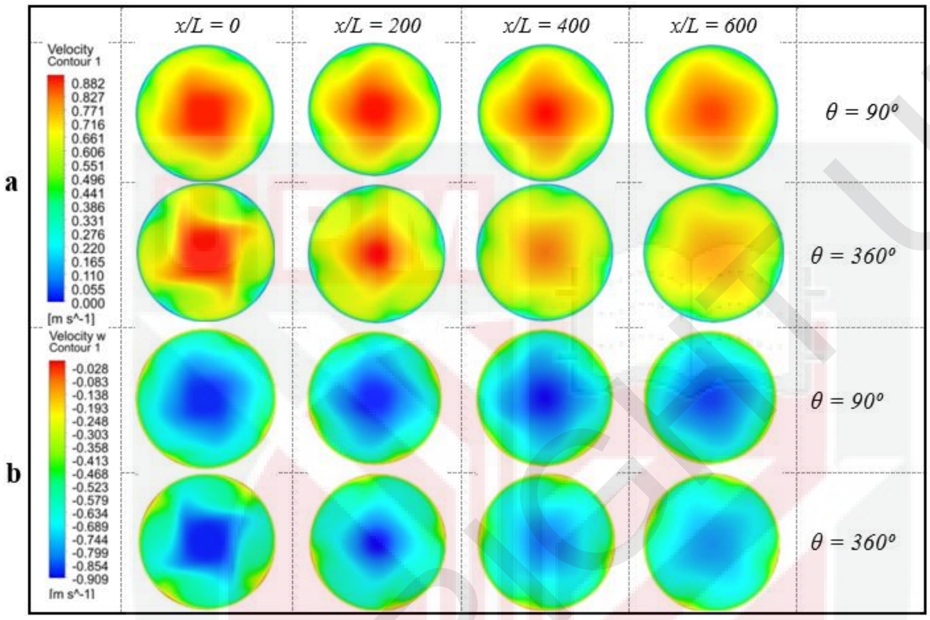

Figure 4.5: a) axial velocity and b) tangential velocity distribution at different twisted angles, and distance under Reynolds number of 35,000

4.2.3 Temperature Distribution

The variation in temperature distribution contour of the smooth channel (test section) at the impact of several twisted angles under Reynolds number 35,000 is analysed. Based on equation (28), the flow direction is the same as the direction of the helix, which is anticlockwise. It can be observed that the temperature at the surface region dramatically increases as the twisting angle increases. The contour also depicted the impact of the twisted angle on the wall (helically red area), which gradually faded with the rise of the test section distance. It can be attributed to the improvement in swirl intensity as the twisted angle increases, as shown in Figure 4.9 (c). The result exhibits a decrease in the temperature distribution with the reduction of twisted angle, as seen in Figures 4.9(a) and 4.9(d). It can be explained by more fluctuation flow associated with a twisted angle of 360º, which caused a thinner boundary layer. Therefore, it leads to better improvement in heat transfer. It is worth mentioning that the wall temperature distribution is highly dependent on the Reynolds number value given, the thermal conductivity of the material, and the twisted angle value. With the augmentation of the twisted angle, the convective heat transfer rises, and the wall temperature distribution displays several characteristics. The result demonstrates that the temperature distribution along the wall of the 360-degree case is more uniform than the other cases. It can be explained by secondary flow leading to swirl flow and generating a considerable heat transfer rate.

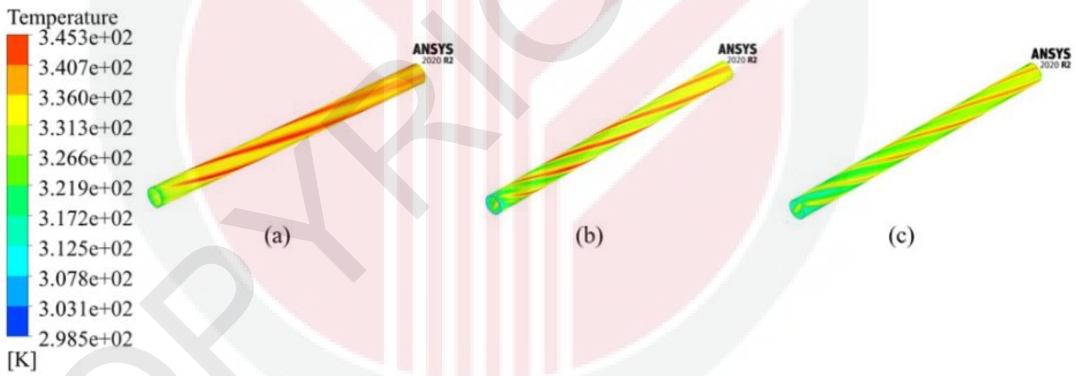

Figure 4.6: Surface temperature distribution of the lobe swirl under different angles (a) 90º, (b) 270º, and (c) 360º

4.2.4 Streamline

Streamline contour shows a swirl flow pattern inside the entry section, lobed swirl generator and circular tube (test section) at different twisted angles. It is worth saying that the direction of the helix is anticlockwise. The results showed a longitudinal vortices pattern formed along the circular tube due to the impact of different twisted angles. Due to the gradual change in the exit transition from a lobed shape to a circular cross-section, the swirl flow exhibits longitudinal vortices. The advantage of this type of vortices is represented in its ability to promote considerable heat transfer with less increase in friction factor (Yifan Wang et al., 2019). The main distinguishing characteristics of longitudinal vortices are their capability to reduce the thermal boundary layer, improve fluid fluctuation, promote the interaction between the temperature field and the fluid flow, and optimize heat transfer while reducing pressure loss and power consumption (Zheng et al., 2020).

Figure 4.10 (a-c) represented 3-D streamlined contours to illustrate the spiral swirl flow pattern from an isometric perspective, whereas Figure 4.10 (d-f) shows swirl flow behaviour in the front view. The outcome was performed at a different angle of 90º, 270º and 360º. The result was conducted at a Reynolds number of 55,000 and geometry contour points of 100 streamlines. The result demonstrates that the lobed swirl generator under different angles can create two essential types of swirling flow. Axial velocity is concentrated in the core and increased in the lobed cross-section region (red zone). The result also proved that the contact between the axial and tangential velocity is the main reason for creating different scale vortices between the core and the wall, as exhibited in Figure 4.10 (d-f).

The contour revealed that the increase in twisted angle led to increased scale vortices. The streamlined distribution confirms that the rise in twisted angle led to more fluctuation in flow. Consequently, it promotes the system's heat transfer and thermal performance. Although the current result performed at the same Reynolds number, the lobe swirl at the angle of 360º presented the superior velocity by the value of 6.87% compared with the angle of 90º. The longitudinal vortices induced by the lobed swirl generator at a twisted angle of 360 degrees are more insensitive, which in turn improves synergy between the velocities and the temperature gradient, causing better thermal performance. The result also confirmed the flow characteristics in smooth channels because of different twisted angles. It can be observed that the fluid adjacent to the wall swirls continuously and dramatically disturbs the boundary layer. It has improved the heat transfer rate due to mixing the fluid flow near the wall (hot water) and at the core (cold water).

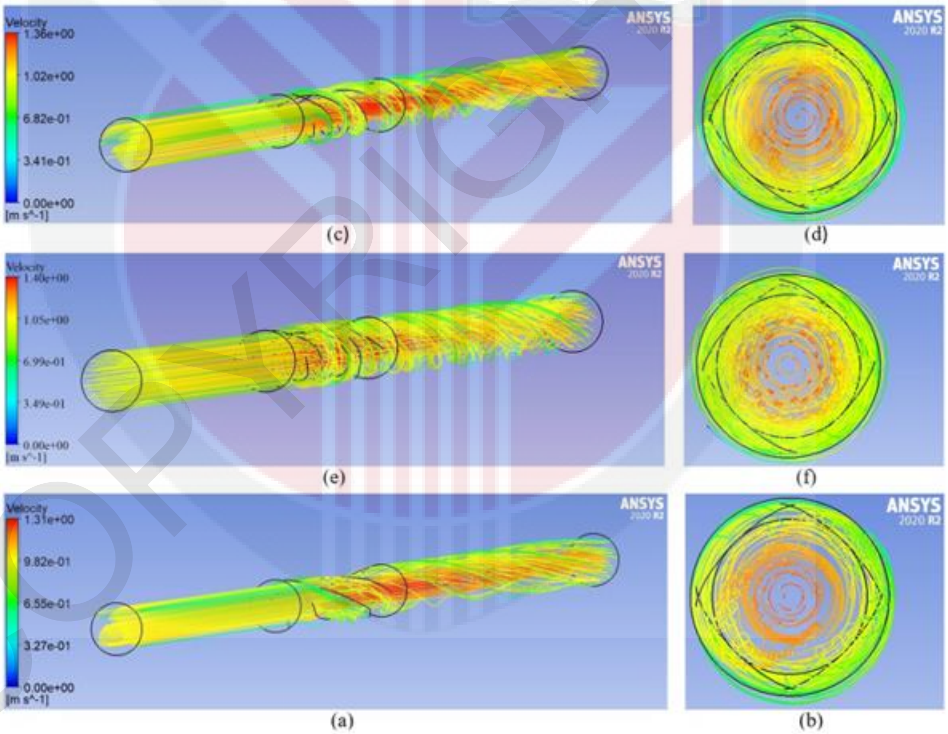

Figure 4.7: 3-D streamline contours of the four-lobed swirl generator under different angles (a) 90º, (b) 270º, and (c) 360º

4.3 The Effect of Beta Transition under Different Parameters on Thermal Performance

The effect of the variation of beta transition values on the transition part's area development is described in Figure 4.1(a). The result demonstrated that the area growth at the start and the end of the transition part at the beta transition value of (β = 0.25 mm) was almost the same. Furthermore, the area exhibits fast growth as the beta transition decreases. It can be attributed to the fact that a decrease in the transition multiplier led to an increase in the overall velocity at the pipe outlet due to a higher rate of swirl motion produced, which is highly consistent with the finding of (Chanchala Ariyaratne, 2005a). According to Figure 4.1(b), the twisting shape grows more quickly at the beginning and the end of the transition part at the values of (t < 1) and (t > 1), respectively. In terms of (t = 1), the twisting cross-section development is constant with respect to the length (geodesic).

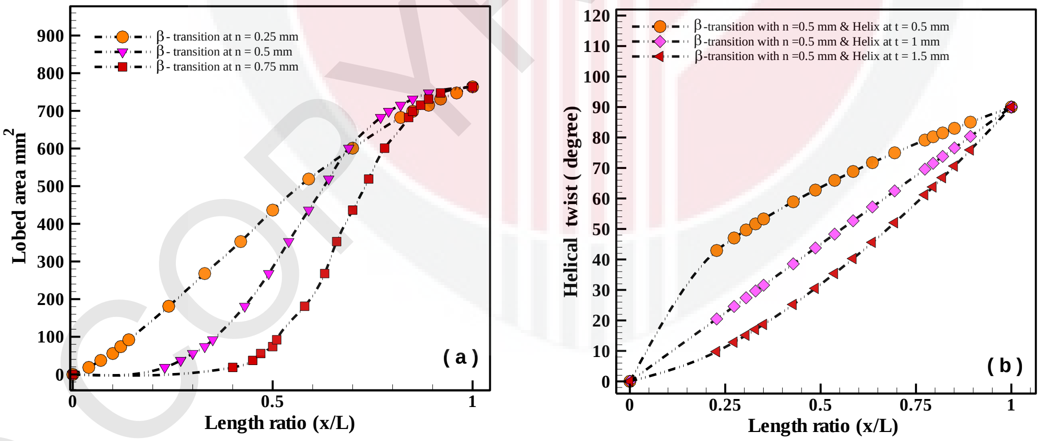

Figure 4.8: Numerical approach of the impact of (a) several transition multipliers on lobe area growth and (b) different values of a variable helix on twisting development

4.3.1 The Effect of Different Multipliers (*n*) on Heat Transfer

This section discusses the study's second objective, which presented a result of the impact of lobed transition parts under their influential parameters on heat transfer, friction factor and thermal performance. The parameters of the transition multiplier investigated in this section are (n = 0.25, 0.5, and 0.75 mm) at a twisted angle of θ = 360. According to the factor, the variable helix was fixed at the value of (t =1) geodesic as the optimum design suggested by Chanchala Ariyaratne (2005a), which revealed that the variable helix is better at (t =1). The transition multiplier factor (n) is vital in controlling the transition section's intermediate area in each step. The variation of the Nusselt number and friction factor with different transition multipliers are investigated.

Regarding the first numerical result of the impact of transition parts at different n, the value of the Nusselt number tends to increase with the augmentation of the Reynolds number and a reduction of the transition multiplier value n. As seen in Figure 4.5(a), the highest Nusselt number at 40.32% was obtained at the minimum value of the transition multiplier of n = 0.25 mm followed by n = 0.5 mm, which emphasizes that the reduction of the transition multiplier led to an increase in heat transfer. This can be attributed to the fact that the transition part n < 1 caused 50% lobed development at the start of the transition part, as proved by Chanchala Ariyaratne (2005a). The development in the intermediate area at the start of the transition components led to an increase in the amount of fluid in this region. As a result, the fluid flow pattern will be changed. In other speaking, the outcome demonstrated the advantage of reducing the transition multiplier value and revealed the capability of the transition multiplier at this value of enhanced heat transfer.

The variations of friction factor with different Reynolds numbers at different transition multipliers are shown in Figure 4.5(b). It can be observed from the Figure there is no significant change in the friction factor between the different values of transition multipliers. The result also showed a decrease in friction factor as the Reynolds number increased for all cases studied.

It can be concluded that at a transition multiplier of (n = 0.25 mm), heat transfer improved from 28.78% to 40.32%, while a slight change in pressure loss by the values 17.35% to 17.89 % compared with lobed swirl generator under twisted angle of 360º and transition multiplier of (n = 0.5 mm) that obtained from previous result. In other words, the decrease of the transition multiplier to the value of (n = 0.25 mm) caused an enhancement in heat transfer by the value of 11.54% with no significant change in pressure drop. The increase in heat transfer is attributed to the characteristics of transition parts under the reduction of transition multiplier factors, which led to the development of the start region of the transition part by the value of 50% (Chanchala Ariyaratne, 2005a). The slight change in pressure loss may be attributed to the feature of the transition part that is formed gradually from a circular shape to a lobed cross-section and vice versa, which was suggested by Ariyaratne, C and Jones (2007).

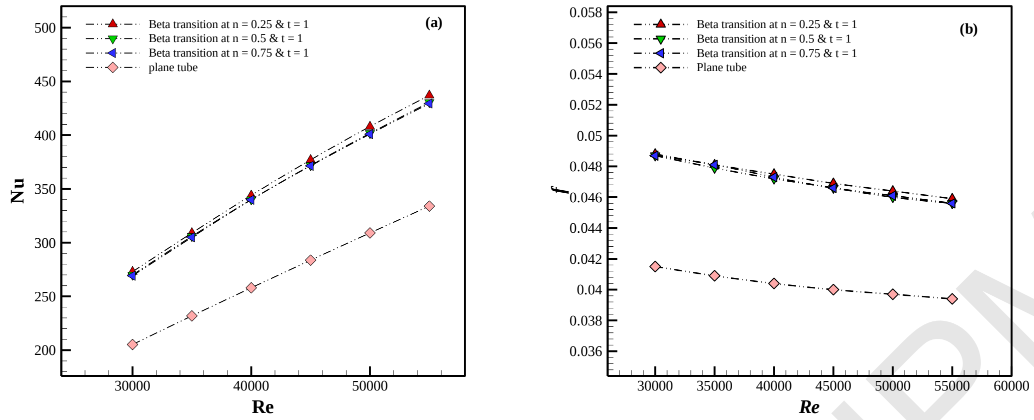

Figure 4.9: Numerical approach of the effect of different beta transition multipliers on (a) heat transfer and (b) friction factor at constant variable helix and twisted angle of 360o using water as a working fluid

Based on the improvement of heat transfer and a slight change in pressure drop from the results obtained by the reduction of transition multiplier values, the balance between the enhancement in heat transfer and the pressure loss should be considered. In other words, the thermal performance of the system should be investigated to prove the features of the parameters that have been studied and their impact on the system's behaviour. Therefore, the performance evaluation criteria (PEC) techniques are considered. A comparison analysis for transition components with various transition multiplier values of (n = 0.25, 0.5, and 0.75 mm) combined with a fixed value of variable helix factor at (t = 1) is carried out in order to investigate the effects of a lobed swirl generator on thermal performance.

The PEC of transition parts under different values of the transition multiplier is shown in Figure 4.6. The outcome proved that the highest thermal performance for all cases studied was obtained at a Reynolds number of 35000. Compared to the transition multipliers, it can be observed that the more extraordinary thermal performance of

1.26 is located at the transition multiplier value of 0.25 mm, which implies that the system's thermal efficiency increases with the reduction of transition multiplier values. It can be explained by the fact that the transition area grows fast as the transition multiplier value decreases. The result also revealed the relation between the transition multiplier and the range of the Reynolds number is nonlinear. It can explain the effectiveness of the transition multiplier at a low Reynolds number by the fact that the better turbulence intensity flow occurred in the smooth channel (test section) at the reduction of n especially at the value of (n = 0.25 mm), which proved that the improvement in the heat transfer between the fluid adjacent to the wall (tangential velocity) region and the fluid flow concentration at the tube central area (axial velocity), which is consistent with the findings of (Ariyaratne, C and Jones, 2007).

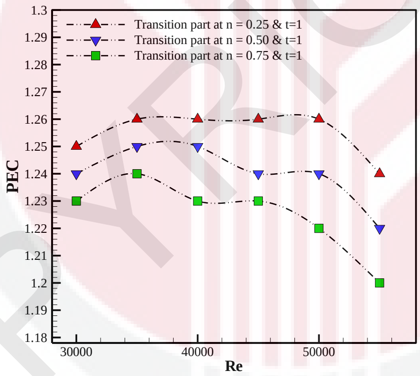

Figure 4.10: Numerical approach of thermal performance value at different transition multipliers and variable helix using water as a working fluid

4.3.2 The Effect of a Variable Helix (*t*)

The power law or variable helix (t) is essential for modifying the transition section's helical shape (G. Li, 2016). The variable helix is the parameter used to identify the helix shape of the transition part, which also caused an increase or decrease in the helix as desired. Therefore, the variable helix (t) with different values of (t = 0.5, 1, and 1.5) on heat transfer and friction factor were considered. These parameters were performed at a twisted angle of 360º and a transition multiplier of 0.25 mm. As shown in Figure 4.7(a-b), the variable helix at the value of (t =1) (geodesic) presented the highest heat transfer improvement with a slight friction factor increase. In other words, linear twisted growth is concerned with the transition length.

As expected, the transition part at constant twisted growth concerning distance (geodesic) results in the efficient swirling flow, which corresponds with the finding of (Chanchala Ariyaratne, 2005b). It can be explained by the increase in the swirl overall in the case of geodesic rather than the brachistochrone helix along the swirl pipe, which was investigated by Raylor (1998). Therefore, a variable helix at the value of (t = 1mm) was adopted as the optimum result.

4.4 Lobed Swirl Generator Thermal Characteristics Using Water Against Different Nanofluids

According to the result of the first numerical work, the second numerical study was carried out. The working fluids adopted in the present study are different nanofluids of SiO_2/water, Al_2O_3/water, and CuO/water, at varying volume concentrations of 1, 2, 3, 4, and 5%.

4.4.1 The Impact of Nanoparticles on (*f*) and (*Nu*)

Swirl flow is the targeted outcome for heat transfer improvement within the tubes of heat exchangers (Bezaatpour & Goharkhah, 2020). The current study aims to investigate the effect of a lobe swirl device under various types of nanoparticle volume concentration on thermal performance enhancement. Subsequently, the influence of

Nusselt number and friction factor were evaluated for several types of nanofluids, including SiO_2/water, Al_2O_3/water, and CuO/water, at varying volume concentrations of 1, 2, 3, 4, and 5%.

The deviation of the Nusselt number and friction factor of SiO_2/water nanofluid is shown in Figure 4.11(a). Regarding the observation, with the rise in nanoparticle's volume concentration, the Nusselt number and friction factor increase. The most remarkable improvement in heat transfer was obtained at 35,000 Reynolds number and volume concentration value of 5%. The highest value of the Nusselt number is 392.115. Compared with plain tube, this value is higher by 55.69%, while the friction factor is higher by 44.31%.

Figure 4.11(b) depicts the variation of Nusselt numbers and friction factor of Al_2O_3/water nanofluid versus different values of Reynolds number. The maximum Nusse number of 367.22 was obtained at a volume concentration of 5% and a Reynolds number of 35,000. It is almost 49.35% higher than the highest heat transfer of plain tube and 12.8% lower than the highest SiO_2/water nanofluid value. The friction factor of Al_2O_3 is 53.8% higher than when a plain tube is used. This result is lower by 17.63% than when employing SiO_2/water nanofluid as a working fluid. The highest friction factor was obtained at a low Reynolds number of 15,000 and a high-volume concentration of 5%. The friction factor decreases with the increase of Reynolds number.

Figure 4.11(c) shows the variation of Nusselt numbers and friction factor of CuO/water nanofluid versus different values of Reynolds number. The outcome presents an enhancement in heat transfer of 40.6% at a high Reynolds number of 35,000 and volume concentration of 5% compared with plain tube. This value is 23.15% and 39% lower than Al_2O_3/water nanofluid and SiO_2/water, respectively. The friction factor obtained with CuO/water nanofluid is 25.9% and 38.98% higher than Al_2O_3/water and SiO_2/water, respectively. It can be concluded that the different thermal properties of the several nanoparticles adopted substantially impact the outcome. For example, the silicon oxide's low density and high-velocity feature, compared to all other nanoparticles, caused better heat transfer.

4.4.2 The Effect on Thermal Performance

The heat transfer after enhancement (*Nu*) to the heat transfer produced by a plane tube (*Nup*) is known as the Nusselt number ratio. Figure 4.12(a-b), respectively, shows the assessment of the Nusselt number ratio (*Nu/Nup*) and friction factor (*f/fp*) at different types of working fluids of SiO_2/water, Al_2O_3/water, CuO/water, and water. The heat transfer and friction factor ratios were performed at a volume fraction of 5% with Reynolds number ranging from 15,000 to 35,000. If thermal performance improvement is targeted, the balance between the increase in heat transfer and the augmentation of friction factor should be considered.

The Nusselt number ratio with the Reynolds number for different types of Nanofluids at a constant volume concentration of 5% is shown in Figure 4.12(a). The heat transfer ratio SiO_2/water is the most prominent, followed by Al_2O_3 and CuO. At a Reynolds number of 15,000, the result presented heat transfer ratios of 1.906, 1.79, 1.719, and 1.332 of SiO_2/water, Al_2O_3/water, CuO/water, and water, respectively. The average increase in Nusselt number ratio up to 43.09%, 35.12%, and 43.09% of SiO_2/water, Al_2O_3/water, and CuO/water, respectively, compared with water as a working fluid.

Figure 4.12(b) displays the variation of friction factor ratio versus Reynolds number (Re) at SiO_2/water, Al_2O_3/water, and CuO/water at a volume concentration of 5% and water as working fluids. Raising the Reynolds number decreases the friction factor ratios for all cases investigated. For nanofluids, the result showed that the *f/fp* of CuO at a Reynolds number of 15000 is 29.9% greater than when using water as a working. Compared with Al_2O_3 and SiO_2 at the same Reynolds number, the *f/fp* of CuO is more significant up to 12.32 % and 19.87%, respectively. The result emphasizes that SiO2 has the lowest friction factor ratio of 8.32% among all nanofluids investigated and compared with water as a working fluid. The finding attributed to increased layer friction forces due to increased viscosity of CuO and Al_2O_3 more than SiO_2 nanoparticles.

Figure 4.12 (c) describes the effect of performance evaluation criteria (PEC) on the application at various nanoparticle volume concentrations and turbulent flow regimes. The outcome proved that the nanofluids significantly impact the performance of the swirl generator. The finding illustrates that, compared to all other nanofluids studied, SiO_2/water nanofluids had the most significant gain in thermal performance at a low Reynolds number. The augmentation in PEC was 39.33%, 28.09%, and 18.34% of SiO_2/water, Al_2O_3/water, and CuO/water, respectively, compared with lobed swirl flow generated underwater as a working fluid. The PEC enhancement of all nanofluids, even water as a working fluid, is more significant than one, emphasising that the augmentation of heat transfer is more than the increment in pressure loss.

Based on the findings, the lobed swirl generator with nanofluid can considerably enhance the heat exchanger's thermal performance, mainly because the working fluid's physical characteristics have improved.

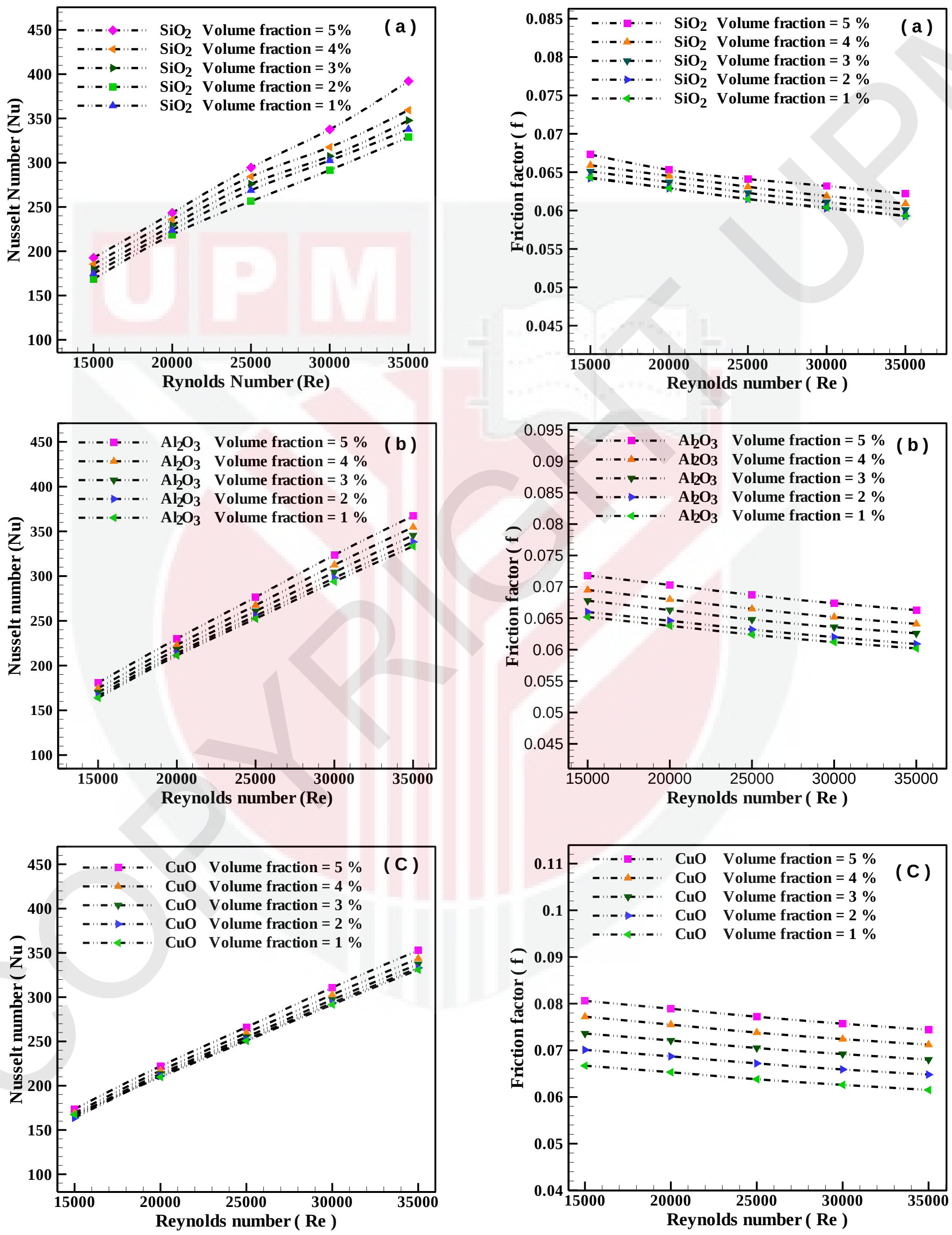

Figure 4.11: Numerical approach of the impact of (a) SiO_2/water, (b) Al_2O_3/water and (c) CuO/water on Nusselt number and friction factor at different Reynolds number

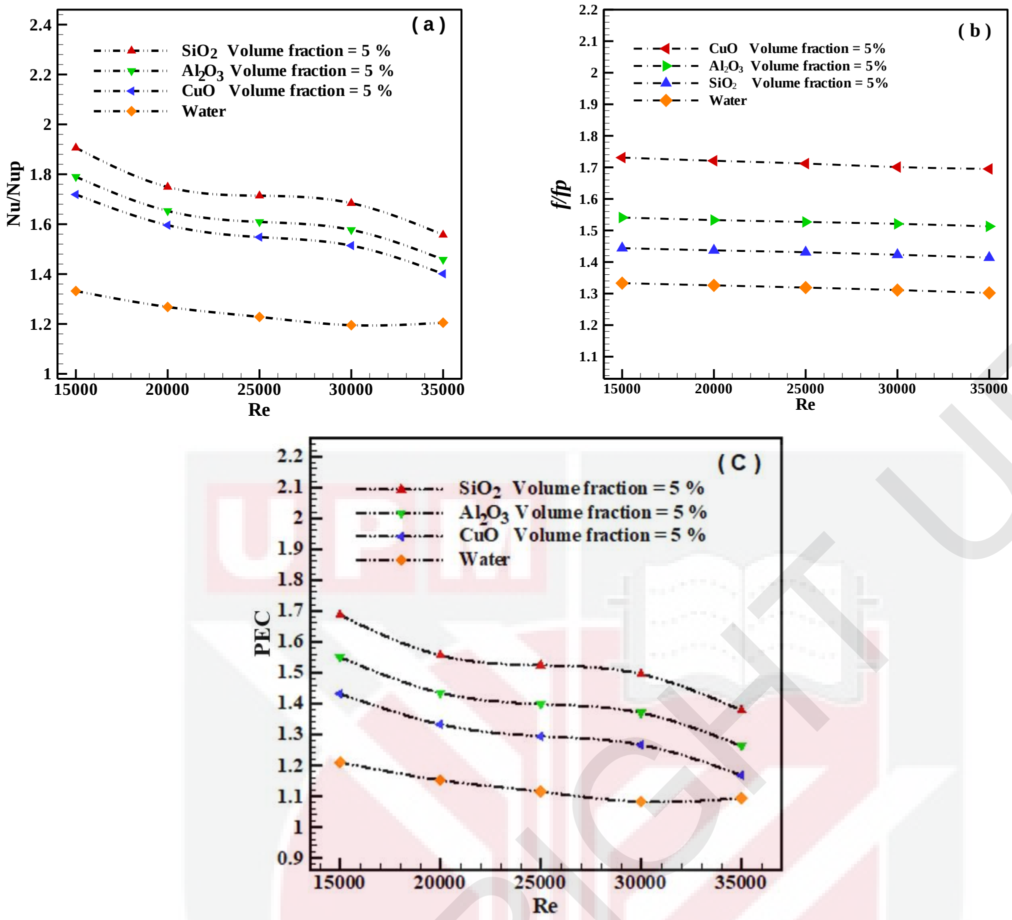

Figure 4.12: Numerical approach of the value of (a) *Nu/Nup*, (b) *f/fp* and (c) PEC at different nanofluids and Reynolds number

4.5 Lobed Swirl Generator Thermal Properties Using Water Against GO-Cuo/Hybrid Nanofluid

The findings of the preparation of the nanofluid experimental work are covered in the present section. There has been a discussion on the new correlational idea. Additionally, employing GO-CuO hybrid nanofluid as the working fluid, the heat transfer, friction factor, and performance evaluation criteria of the system under various effective variables.

4.5.1 Thermal Conductivity as a Function of (T) and (φ)

The hybrid nanofluid of GO-CuO was studied in the current experiment at various volume concentrations ranging from 0.15 to 0.75% and multiple temperatures ranging from 25 to 50 ºC. The thermal conductivity can be estimated using a relationship between the temperature and volume concentration of nanoparticles by modifying the variables (Kazemi et al., 2020). The improvement in thermal conductivity versus the different amounts of solid volume fraction and various temperatures is conducted. The outcome revealed that the increase in nanoparticle volume concentrations and temperatures considerably impacted thermal conductivity improvement. Figure 4.13(a) shows how thermal conductivity changes at different solid volume fractions while maintaining a constant temperature. Figure 4.13(b) shows how thermal conductivity improves to varying temperatures while maintaining a constant volume fraction. This phenomenon was studied at an important impact parameter (T& φ) to determine whether the variation in solid volume fraction or temperatures significantly impacts thermal conductivity improvement. For example, at the constant temperature of 25ºC and increasing the solid volume fraction from 0.15% to 0.75%, the thermal conductivity improved by 37.55%.

Furthermore, at the same condition but fixed the temperature at 50ºC, the thermal conductivity was enhanced by 39.68%, which implies that the improvement in thermal conductivity by increasing the temperature from 25ºC to 50ºC at different volume concentrations reached 5%. The results demonstrated that thermal conductivity is affected by the concentration of volume fraction more than in the case of temperature difference. It can be attributed to the augmentation of kinetic energy, the rate of collisions, and the Brownian motion phenomenon due to the nanoparticle's additive.

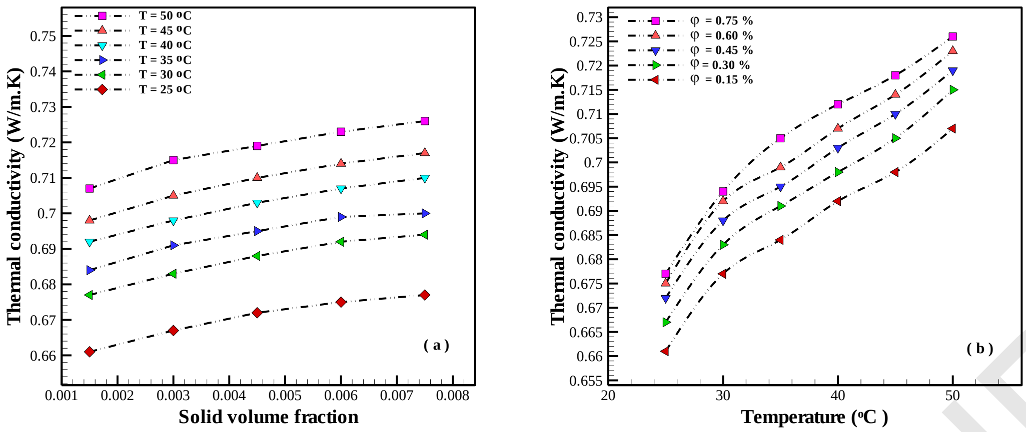

Figure 4.13: Experimental study of the variation of thermal conductivity by (a) a different temperature at the impact of solid volume fraction and (b) a different solid volume fraction at the impact of temperature

4.5.1.1 The Performance of Thermal Conductivity

The development of highly effective heat transfer fluids using nanofluids has the potential to decrease heat loss, improve heat transfer performances, and accelerate cooling speeds (Pavia et al., 2021). The ratio and improvement of thermal conductivity compared to base fluid are considered to evaluate the hybrid nanofluid's performance. The thermal conductivity ratio is defined as the thermal conductivity of the nanofluid (Knf) to the thermal conductivity of the base fluid (Kbf). The thermal conductivity ratio (TCR) and thermal conductivity enhancement (TCE) can be written as illustrated in Equations. (89) & (90) as follows:

$$Thermal\ conductivity\ ratio = \frac{K_{nf}}{K_{bf}} \tag{89}$$

$$Thermal\ conductivity\ enhancement\ (\%) = \frac{K_{nf} - K_{bf}}{K_{bf}} \tag{90}$$

The thermal conductivity ratio pattern at various volume concentrations and temperatures is considered. Figure 4.14(a) indicates the thermal conductivity ratio versus a solid volume fraction at the impact of different temperatures. In contrast, Figure 4.14(b) shows the thermal conductivity ratio versus a temperature at various nanoparticle volume concentrations. The outcome showed the various slope trends and a similar value for the thermal conductivity ratio. TCR increased from 1.062 at T = 25ºC and a volume concentration of 0.15% to 1.097 at T = 50ºC and a volume concentration of 0.75%. The result proved the effect of nanoparticle volume concentration and temperature on improving the relative thermal conductivity. The outcome showed that the thermal conductivity ratio grew with nanofluid solid volume fraction additive and the range of temperatures chosen. There is no comparable pattern slop for mass fractions and temperatures. For example, TCR for hybrid nanofluid was 0.15%, from 1.0625 at 25ºC up to 1.07 at 50C, which signifies a TCR increase of 0.943%. Thermal conductivity ratio for GO-CuO/water hybrid nanofluid at 0.75% volume fraction, from 1.081 at 25ºC up to 1.0965 at 50ºC, which indicates TCR improved by 1.53%. Increased suspension levels due to nanoparticle additives and the range of temperatures led to more nanoparticle interactions, which caused a rise in the surface-to-volume ratio.

According to thermal conductivity enhancement (TCE), the result is depicted in Figure 4.15. The outcome revealed the effect of various temperatures and volume concentrations on improving thermal conductivity. The highest enhancement thermal conductivity of 8.8% was found at the higher temperature and volume concentration of 50 ºC and 0.75%.

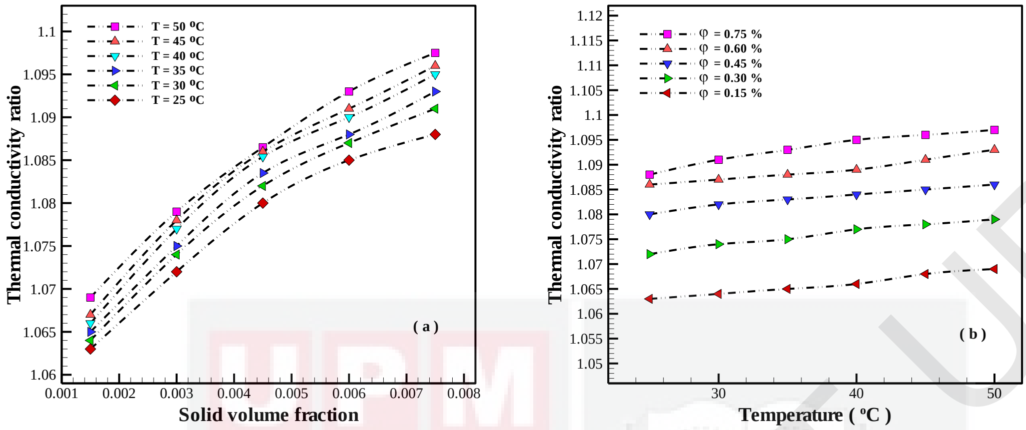

Figure 4.14: Experimental study of the variation of thermal conductivity ratio by (a) a different temperature at the impact of solid volume fraction and (b) a different solid volume fraction at the impact of temperature

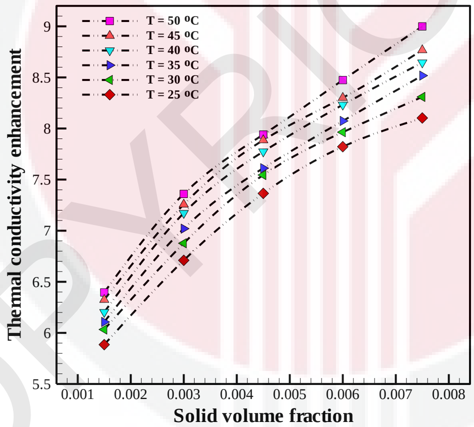

Figure 4.15: Experimental study of the variation of thermal conductivity enhancement by a different volume concentration at various temperatures

4.5.1.2 Proposed New Correlation

According to an investigation of the literature, thermophysical characteristics of the nanoparticles include their temperature, volume fraction, size of nanoparticles, etc. Due to the lack of a reliable, adequate connection for predicting GO-CuO's thermal conductivity, this section used the curve-fitting approach to propose an experimental relation. A novel correlation is proposed, considering empirical data from this work on the thermal conductivity of nanofluid with variations in volume fraction and temperature. GO-CuO/water hybrid-nanofluid at 25-50 ºC and 0.15 -0.75% volume concentration suggested a new correlation, as illustrated in equation (91).

$$\frac{K_{nf}}{K_{bf}} = 1 + 0.17372 \times \varphi^{0.21988} \times T^{0.11408} \tag{91}$$

As shown in Figure 4.16, the accuracy of this correlation is very high, with R2= 0.9951. As can be seen, most of the points are situated (located) on or close to the bisector (middle), which signifies that the suggested correlation is accurate enough. It can be noted that most points correspond between the experimental result and predicted data with a slight deviation of +0.094 -0.091, and the average deviation is 0.018%. A mean squared error (MSE) has been added to validate the regression model. It validates the difference between the experimental data and the predicted data. The mean square error rises exponentially with an increment of the error. A good model result should have a mean square error closer to zero. The MSE value obtained is 1.2E-06. The following equation has been used to estimate the MSE (Hemmat Esfe et al., 2015);

$$MSE = \frac{1}{n}\sum_{i=1}^{n}(P_i - m_i)^2 \tag{92}$$

Where n is the number of actual values (data values), pi is the experimental data, and mi is the predicted values. The R2 value of 0.9951, the MSE of 1.2E-06 (closer to zero), and the maximum error of +0.094 -0.091 confirmed that the correlation performance is considered satisfactory, implying that the experimental data and the proposed correlation can apply to the thermal conductivity of GO-CuO/water hybrid nanofluid.

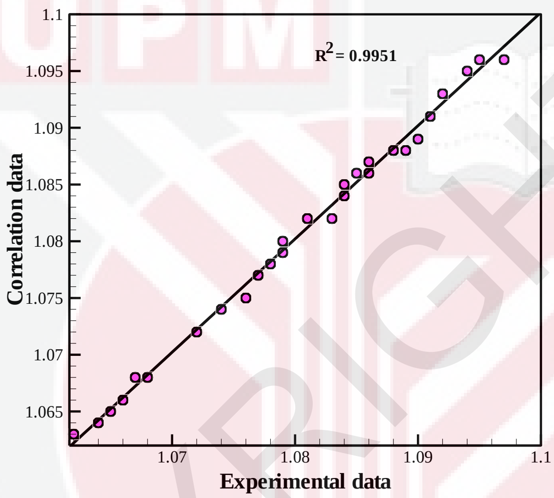

Figure 4.16: Experimental study of the comparison between correlation data outcome and the experimental data

4.5.1.3 Margin of Deviation

The margin of deviation method with respect to volume concentrations and various temperature changes has been conducted for more accuracy. The margin of deviation is evaluated using equation (93). The range of variation of margin deviation with respect to volume fraction from (0.15 to 0.75%) at various temperatures from (25 to 50 ºC) is shown in Figure 4.17. The outcome demonstrates considerable accuracy of less than 0.06% for all points investigated.

$$Deviation\ margin(\%) = \frac{\left(\frac{K_{nf}}{K_{bf}}\right)_{Exp} - \left(\frac{K_{nf}}{K_{bf}}\right)_{pred}}{\left(\frac{K_{nf}}{K_{bf}}\right)_{pred}} \quad (93)$$

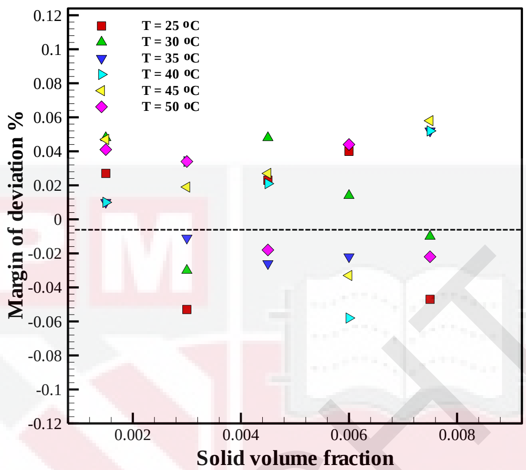

Figure 4.17: Experimental study of the Margin of deviation by GO-CuO/water hybrid nanofluid data concerning volume fraction and a given of several temperatures

4.5.2 Comparison Between the Experimental Data and Proposed Empirical Correlation

The thermal conductivity ratio of experimental results and the proposed correlation based on solid volume fraction at various temperatures are shown in Figure 4.18. Every point of the observed correlation and the experimental outcome are in good agreement.

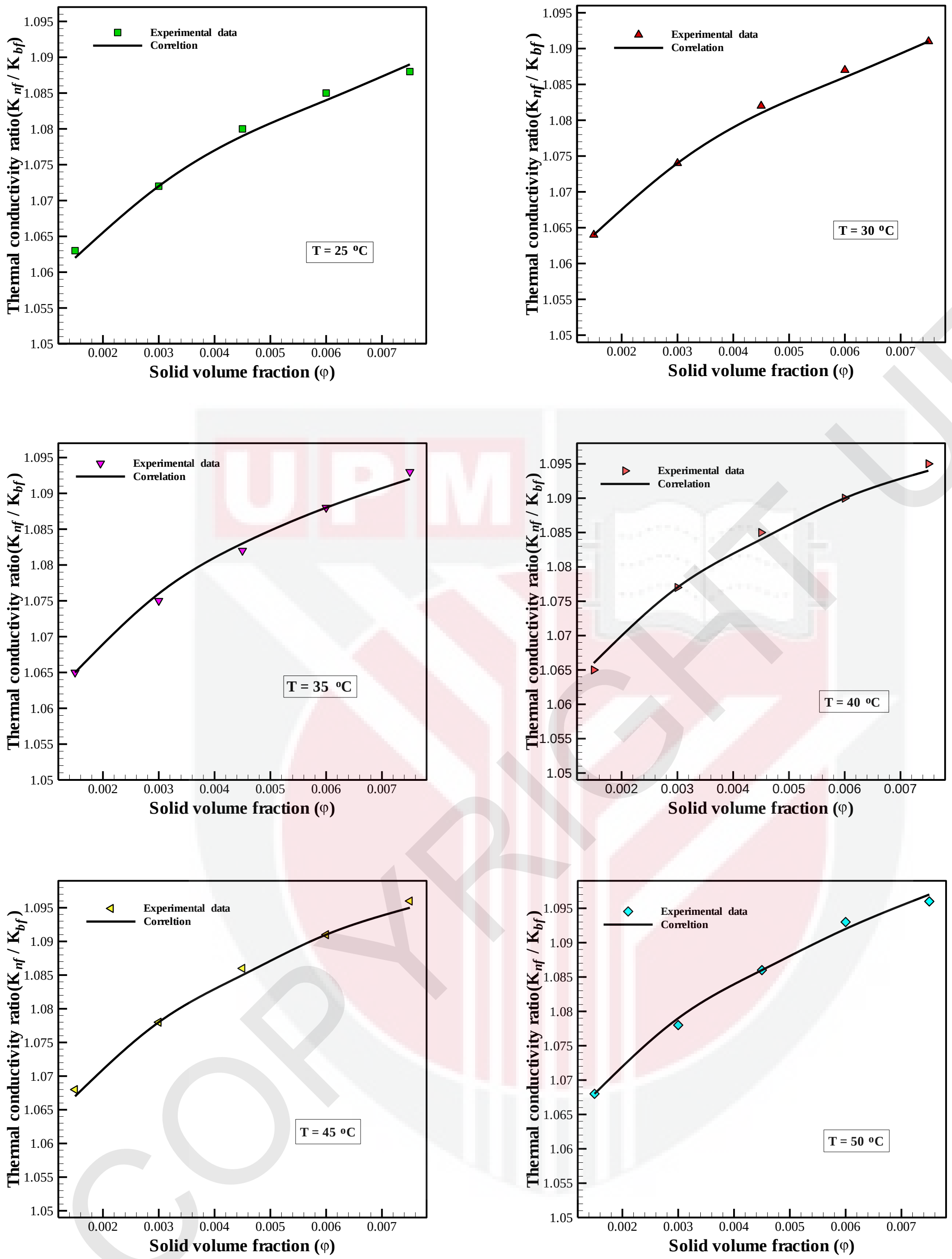

Figure 4.18: Experimental study of the relationship between experimental data and the suggested empirical correlation regarding thermal conductivity ratio.

4.5.3 Comparison Between an Experimental and Numerical Result

Figure 4.19 (a & b) compares the experimental and numerical results of the Nusselt number and friction factor at the Reynolds Number ranging from 15.000 to 35,000. The comparison was conducted at a Four-lobe swirl generator at an angle of 360º. The outcome showed that the maximum difference between the experimental and numerical results is 9.715% for the Nusselt number and 4.694% for the friction factor. The findings demonstrate that for the Nusselt number and friction factor, the percentage difference between numerical and experimental results is less than 10%, which is suitable for thermal engineering applications (M. Li et al., 2016). Therefore, a comparison between experimental and numerical outcomes is in agreement.

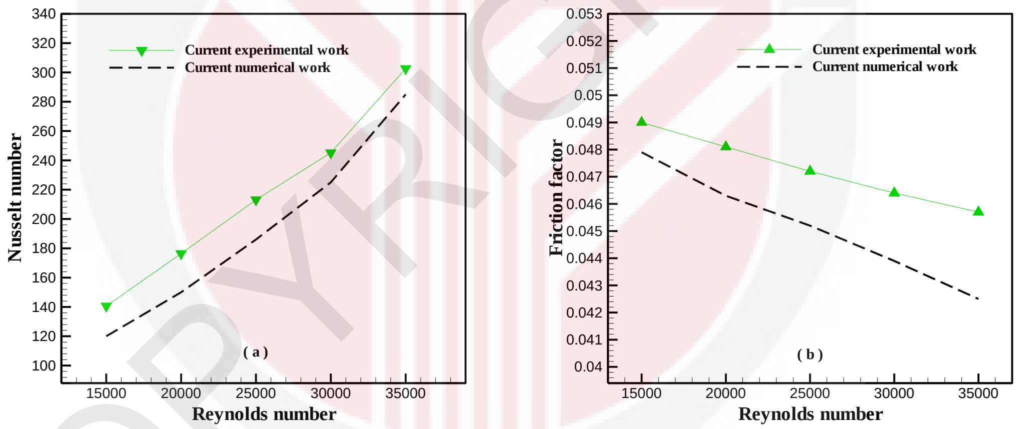

Figure 4.19: A comparison between the experimental and numerical result on the effect of lobed swirl number at 360º and water as working fluid on (a) Nusselt number and (b) Friction factor

4.5.4 Heat Transfer

The main target of the current experimental study is to examine the thermal performance of lobe swirl generators under different working fluids (water and graphene-CuO/water nanohybrid). The lobe swirl generator was performed at the optimal parameters of the twisted angle of (θ = 360º), twisted length of (l = 0.4 m), beta transition at a transition multiplier of (n = 0.25 mm) and variable helix of (t =1). It is expected that the benefit of the lobe swirl generator of induced azimuthal velocity near the wall and the enhanced thermal conductivity of working fluid by adding a hybrid nanofluid will considerably increase thermal performance. The effect of the lobe swirl generator at different working fluids under the variations of nanoparticle volume concentration and Reynolds numbers on heat transfer enhancement is shown in Figure 4.20(a).

In terms of nanofluid, the increase in hybrid nanoparticle volume concentration led to an increase in heat transfer. It can be attributed to the enhancement of thermal conductivity, which is the main feature of employed hybrid nanoparticles. Furthermore, at high Reynolds numbers, the character of the flow turbulence and the lobe swirl's circulation feature substantially influence avoiding nanoparticle accumulation, particularly at high-volume concentrations. Figure 4.20(b) shows the effect of the Nusselt number ratio at a different Reynolds number. The result presented an enhancement of heat transfer value by the factor of 1.76 at a Reynolds number of 25000. It can be explained by the significant effect of pressure loss at the high Reynolds number. In general, the result demonstrates the capability of a current application to improve heat transfer due to various vital factors of lobed swirl curvature and transition part beneficial, turbulent flow and additive hybrid nanofluid.

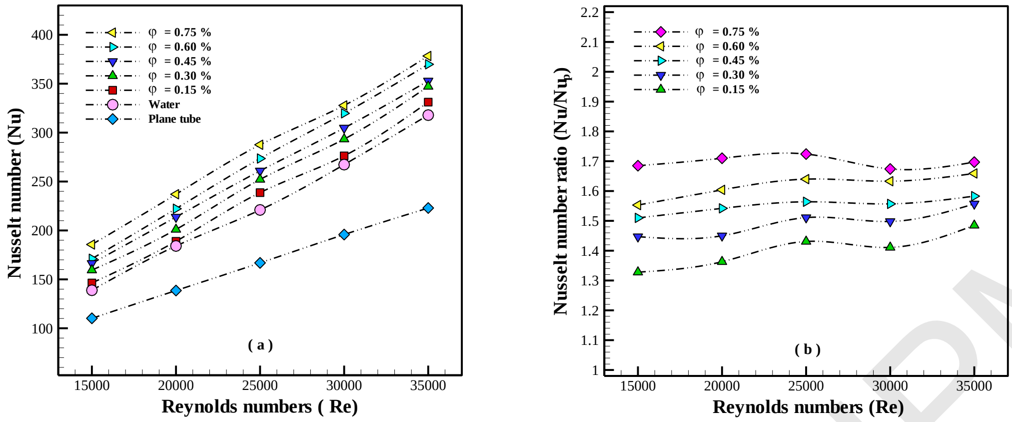

Figure 4.20: Experimental study of the effect of lobe swirl generator under different volume concentrations and Reynolds number on heat transfer (a) Nusselt number, (b) Nusselt number value

4.5.5 Friction Factor

The friction factor of the nanofluids at different volume fractions is shown in Figure 4.21(a) as a function of the Reynolds number. Equation (67) has been considered to evaluate the friction factor over the test section. It is expected the effectiveness of combining lobe swirl generator cross-section, nanoparticles additive and high Reynolds number led to increasing pressure loss. The overall trend shows that the friction factor decreases with an increase in Reynolds number and vice versa. Additionally, the friction factor gradually increases as the nanoparticle volume concentration increases, which can be explained by the perturbation (disturbance), flow blockage caused by the added hybrid nanoparticles, the centrifugal force of the lobe swirl, and turbulent flow fluctuations. The ratio between the friction factor at different volume concentrations and the friction factor at the plane tube is illustrated in Figure 4.21(b). The result indicated that the maximum difference in friction factor value is 1.53, which is associated with high volume fraction and Reynolds number.

The result revealed a proportional relationship between the friction factor and the increase of nanoparticle volume fraction and high Reynolds number.

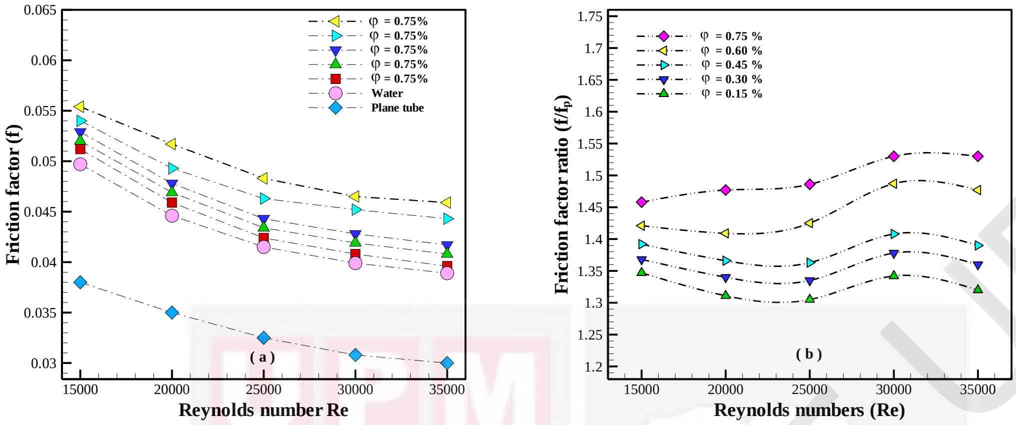

Figure 4.21: Experimental study of the effect of lobe swirl generator under different volume concentrations and Reynolds number on friction factor (a) Friction factor (b) Friction factor value

4.5.6 Performance Evaluation Criteria

Equation (68) evaluates the Performance Evaluation Criterion (PEC). According to the experimental data implied in Figure 4.22, the ability of a lobed swirl generator under a variation of volume concentrations and Reynolds numbers to improve thermal performance was evident. Based on all cases investigated, the outcome proved to be a superior improvement in PEC. The result revealed that the highest values of PEC recorded at the Reynolds number of 25,000 were 1.309, 1.372, 1.41, 1.457, and 1.511 at a volume concentration of 0.15%, 30%, 0.45%, 0.60%, and 0.75% respectively. Therefore, the improvement in this value of the low Reynolds number can be attributed to the dramatic increase in the friction factor at a high Reynolds number, in addition to the rough surface of the lobe swirl generator cross-section. To the best of our knowledge and based on the literature, the increase in nanoparticle volume concentration led to increased heat transfer due to the promotion of nanofluid's thermal conductivity. At the same time, an increase in the friction factor due to the increase in viscosity during the use of nanofluid in thermal application occurred. Therefore, the balance between the increase in heat transfer and the friction factor is taken into account.

Consequently, the ratio of the Nusselt number result (*Nu/Nup)* and the ratio of friction factor result (*f/fp*), as discussed in the previous result, is considered. Furthermore, the high cost of graphene oxide, which reaches 200 RM per gram, limits the use of large nanoparticle concentrations. In addition, the stability of the nanofluids associated with low volume concentration is also considered.

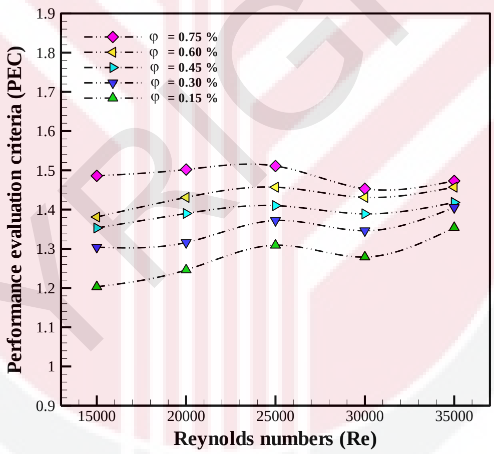

Figure 4.22: Experimental study of the effect of lobe swirl generator under different volume concentrations and Reynolds number on thermal performance

CHAPTER 5

CONCLUSION AND RECOMMENDATIONS FOR FUTURE WORK

5.1 Conclusion

In the present study, the effect of a four-lobed swirl device with its transition parts on thermal performance and fluid field has been carried out numerically and experimentally. The geometry related to the first numerical study can be divided into two main practical parts. (i) the lobed swirl device was performed under a fixed length of 0.2 m, with a beta transition at the multiplier of (n = 0.5 mm) and different twisted angles from (90o to 450o). (ii) the second vital section is the transition parts, which are 0.1 m long and equipped at the entry and exit lobed swirl device. This part was investigated at different transition multipliers (n = 0.25, 0.5 and 0.75 mm) and several variable helixes (t = 0.5, 1, 1.5 mm). The working fluid adopted is water at a Reynolds number varying between 30,000 to 55,000.

The second numerical study was conducted under a four-lobed swirl generator of 360º with the transition part's effective parameters of (*n*= 0.25) and (*t* =1). The working fluids adopted are different types of nanofluids of SiO_2/water, Al_2O_3/water, and CuO/water under different volume concentrations of 1, 2, 3, 4 and 5% generated at a Reynolds number ranging between 15,000 to 30,000. Finally, an experimental study was performed under the same conditions as a second numerical study, but the working fluid was a hybrid nanofluid of GO-CuO/water with a volume concentration ranging from 0.15% to 0.75%. After performing the numerical and experimental studies, the extracted outcome is listed below:

- The outcome demonstrated that the heat transfer was dramatically increased by increasing the twisted angle. Furthermore, the lobed swirl generator associated with the angle of (θ =360º) presented the highest heat transfer value up to 28.78 and thermal performance of PEC = 1.21.
- The result demonstrates a slight increase in thermal performance by the factor of 1.26, by reducing the transition part to the values of (n = 0.25 mm) and (t = 1)
- The finding also revealed that nanofluid with a lobed swirl generator can promote the lobed swirl generator's thermal performance. Therefore, an augmentation up 1.67 was observed with SiO_2/water at a volume concentration of 5%.
- The highest thermal performance obtained with GO-CuO/hybrid nanofluid was 1.511, respectively, at Reynolds number 15,000 and a volume fraction of 0.75%.

5.2 Recommendation for Future Work

- Future studies are suggested to optimize system parameters such as pipe length and corrugated channel, employ other types of lobed swirling with varied structures, and determine ways to perform rotation.
- The field of study might be extended to optimise the swirl flow by adding additional techniques, such as twisted tape inserts and using different types of corrugated channels.
- Future work is highly suggested to investigate the current nanofluid of SiO_2, Al_2O_3, and CuO to a minimum volume concentration experimentally.

- By modifying the length and developing the progressive angle from a circular shape to a lobe cross-section, future work may be made to promote the role of lobe transition regions.
- Many previous studies of particle-laden systems proved that the current lobe swirl generator is an optimal choice for preventing erosion of the pipe. Therefore, it is highly recommended for future work to study this phenomenon in the applications of heat transfer, especially when using a nanofluid technique
- The study could also be extended to examine the effect of transition parts under different lobed numbers, taking into consideration the related calculation based on the trigonometric functions.
- The augmentation of the twisted angle more than 360° can limit the system's improvement. The substantial increase in the angle curvature and the high turbulent flow led to increased pressure drop. Therefore, the current application with a 360° and below twisted angle is highly recommended.

REFERENCES

Adun, H., Adedeji, M., Dagbasi, M., & Babatunde, A. (2022). Amelioration of thermodynamic performance and environmental analysis of an integrated solar power generation system with storage capacities using optimized ternary hybrid nanofluids. Journal of Energy Storage, 51(April), 104531. https://doi.org/10.1016/j.est.2022.104531

Agarwal, S., Upadhyay, G., & Bhosale, Y. (2024). Density-contrast induced inertial forces on particles in oscillatory flows. Journal of Fluid Mechanics, 985(11-Febrouary), 1–26. https://doi.org/10.1017/jfm.2024.303

Ahmadi, N., Ashrafi, H., Rostami, S., & Vatankhah, R. (2022). Investigation of the effect of gradual change of the inner tube geometrical configuration on the thermal performance of the double-pipe heat exchanger. Iranian Journal of Chemistry and Chemical Engineering, 42(7), 2305–2317. https://ijcce.ac.ir/article_697969.html

Ahmed, M. A., Yusoff, M. Z., Ng, K. C., & Shuaib, N. H. (2014). Effect of corrugation profile on the thermal-hydraulic performance of corrugated channels using CuO-water nanofluid. Case Studies in Thermal Engineering, 4, 65–75. https://doi.org/10.1016/j.csite.2014.07.001

Ahmed, W., Zhan, Y., Zhang, H., Zhou, X., Shahid, M., Mudasar, F., & Khan, Q. U. (2023). Preparation, applications, stability and improved thermal characteristics of sonochemically synthesized nanosuspension using varying heat exchangers, a Review: Journal of Molecular Liquids, 387(March), 122665. https://doi.org/10.1016/j.molliq.2023.122665

Ajeel, R. K., Salim, W. S. I., Sopian, K., Yusoff, M. Z., Hasnan, K., Ibrahim, A., & Al-Waeli, A. H. A. (2019). Turbulent convective heat transfer of silica oxide nanofluid through corrugated channels: An experimental and numerical study. International Journal of Heat and Mass Transfer, 145, 118806. https://doi.org/10.1016/j.ijheatmasstransfer.2019.118806

Aksoz, Z. Y., Bogrekci, I., & Demircioglu, P. (2024). Thermo-hydraulic Investigation of a Heat Exchanger Tube Equipped with 3D-Printed Swirl Flow Generators. Arabian Journal for Science and Engineering. https://doi.org/10.1007/s13369-024-09080-9

Al-asadi, M. T. K. (2018). Heat transfer , fluid flow analysis and energy management of micro-channel heat sinks using vortex generators and nanofluids.

Al-Obaidi, A. R., & Sharif, A. (2021). Investigation of the three-dimensional structure, pressure drop, and heat transfer characteristics of the thermohydraulic flow in a circular pipe with different twisted-tape geometrical configurations. Journal of Thermal Analysis and Calorimetry, 143(5), 3533–3558. https://doi.org/10.1007/s10973-019-09244-y

Al-Shamani, A. N., Sopian, K., Mohammed, H. A., Mat, S., Ruslan, M. H., & Abed, A. M. (2015). Enhancement heat transfer characteristics in the channel with Trapezoidal rib-groove using nanofluids. Case Studies in Thermal Engineering, 5, 48–58. https://doi.org/10.1016/j.csite.2014.12.003

Alawi, O. A., Sidik, N. A. C., Xian, H. W., Kean, T. H., & Kazi, S. N. (2018). Thermal conductivity and viscosity models of metallic oxides nanofluids. International Journal of Heat and Mass Transfer, 116(29-September), 1314–1325. https://doi.org/10.1016/j.ijheatmasstransfer.2017.09.133

Alempour, S. M., Abbasian Arani, A. A., & Najafizadeh, M. M. (2020). Numerical investigation of nanofluid flow characteristics and heat transfer inside a twisted tube with elliptic cross section. Journal of Thermal Analysis and Calorimetry, 140(3), 1237–1257. https://doi.org/10.1007/s10973-020-09337-z

Alhakeem, M. R. H. (2022). Enhancing Thermal Conductivity and Heat Transfer using Graphene Nanofluid. International Journal of Multidisciplinary Sciences and Arts, 01(01), 95–103. https://doi.org/10.47709/ijmdsa.v1i1.1710

Ali, A. M., Rona, A., Kadhim, H. T., Angelino, M., & Gao, S. (2021). Thermo-hydraulic performance of a circular microchannel heat sink using swirl flow and nanofluid. Applied Thermal Engineering, 191(February), 116817. https://doi.org/10.1016/j.applthermaleng.2021.116817

Annaratone, D. (2010). Engineering heat transfer. In Engineering Heat Transfer. https://doi.org/10.1007/978-3-642-03932-4

Ariyaratne, C and Jones, T. (2007). Design and Optimization of Swirl Pipe Geometry for Particle-Laden Liquids. AIChE Journal, 59(4), 757--768. https://doi.org/10.1002/aic

Ariyaratne, C., & Jones, T. F. (2007). Design and optimization of swirl pipe geometry for particle-laden liquids. AIChE Journal, 53(4), 757–768. https://doi.org/10.1002/aic.11122

Ariyaratne, Chanchala. (2005a). Design and optimisation of swirl pipes and transition geometries for slurry. PhD Thesis [University of Nottingham]. In School of Chemical, Environmental and Mining EngineeringUniversity of Nottingham. http://eprints.nottingham.ac.uk/id/eprint/11570

Ariyaratne, Chanchala. (2005b). DESIGN AND OPTIMISATION OF SWIRL PIPES AND TRANSITION GEOMETRIES FOR SLURRY TRANSPO [University of Nottingham]. In Measurement Techniques (Issue August). http://eprints.nottingham.ac.uk/id/eprint/11570

Arya, H., Sarafraz, M. M., Pourmehran, O., & Arjomandi, M. (2019). Heat transfer and pressure drop characteristics of MgO nanofluid in a double pipe heat exchanger. Heat and Mass Transfer, 55(24-February), 1769--1781.

Asadi, A., Pourfattah, F., Miklós Szilágyi, I., Afrand, M., Żyła, G., Seon Ahn, H., Wongwises, S., Minh Nguyen, H., Arabkoohsar, A., & Mahian, O. (2019). Effect of sonication characteristics on stability, thermophysical properties, and heat transfer of nanofluids: A comprehensive review. Ultrasonics Sonochemistry, 58(17-July), 104701. https://doi.org/10.1016/j.ultsonch.2019.104701

ASHRAE. (2015). 2015 Ashrae Handbook.

Awais, M., Bhuiyan, A. A., Salehin, S., Ehsan, M. M., Khan, B., & Rahman, M. H. (2021). Synthesis, heat transport mechanisms and thermophysical properties of nanofluids: A critical overview. International Journal of Thermofluids, 10(26-March), 100086. https://doi.org/10.1016/j.ijft.2021.100086

Babar, H. (2019). Towards hybrid nano fl uids : Preparation , thermophysical properties , applications , and challenges. Journal of Molecular Liquids, 281(27-February), 598–633. https://doi.org/https://doi.org/10.1016/j.molliq.2019.02.102

Babar, H., & Ali, H. M. (2019). Towards hybrid nanofluids: Preparation, thermophysical properties, applications, and challenges. Journal of Molecular Liquids, 281, 598–633. https://doi.org/10.1016/j.molliq.2019.02.102

Bakhtiari, R., Kamkari, B., Afrand, M., & Abdollahi, A. (2021). Preparation of stable TiO_2-Graphene/Water hybrid nanofluids and development of a new correlation for thermal conductivity. Powder Technology, 385, 466–477. https://doi.org/10.1016/j.powtec.2021.03.010

Bakthavatchalam, B., Habib, K., Saidur, R., Saha, B. B., & Irshad, K. (2020). Comprehensive study on nanofluid and ionanofluid for heat transfer enhancement: A review on current and future perspective. Journal of Molecular Liquids, 305(5-March), 112787. https://doi.org/10.1016/j.molliq.2020.112787

Bali, T., & Sarac, B. A. (2014). Experimental investigation of decaying swirl flow through a circular pipe for binary combination of vortex generators. International Communications in Heat and Mass Transfer, 53, 174–179. https://doi.org/10.1016/j.icheatmasstransfer.2014.02.030

Bari, S., & Saad, I. (2013). CFD modelling of the effect of guide vane swirl and tumble device to generate better in-cylinder air flow in a CI engine fuelled by biodiesel. Computers and Fluids, 84(26-June), 262–269. https://doi.org/10.1016/j.compfluid.2013.06.011

Bérut, E., Lips, S., Lefèvre, F., & Sartre, V. (2022). Condensation regimes inside a vapor chamber with transparent hollow fins of circular , triangular or fluted cross section. International Journal of Thermal Sciences, 184, 1–25.

Bezaatpour, M., & Goharkhah, M. (2020). Convective heat transfer enhancement in a double pipe mini heat exchanger by magnetic fi eld induced swirling fl ow. Applied Thermal Engineering, 167(February 2019), 114801. https://doi.org/10.1016/j.applthermaleng.2019.114801

Biegger, C., Sotgiu, C., & Weigand, B. (2015). Numerical investigation of flow and heat transfer in a swirl tube. International Journal of Thermal Sciences, 96(13-January), 319–330. https://doi.org/10.1016/j.ijthermalsci.2014.12.001

Bilen, K., Tokgoz, N., Solmaz, İ., & Balta, T. (2022). Thermo-hydraulic performance of tube with decaying swirl flow generators. Applied Thermal Engineering, 200(August 2021), 117643. https://doi.org/10.1016/j.applthermaleng.2021.117643

Boroomandpour, A., Toghraie, D., & Hashemian, M. (2020). A comprehensive experimental investigation of thermal conductivity of a ternary hybrid nanofluid containing MWCNTs- titania-zinc oxide/water-ethylene glycol (80:20) as well as binary and mono nanofluids. Synthetic Metals, 268(July), 116501. https://doi.org/10.1016/j.synthmet.2020.116501

Borzuei, M., & Baniamerian, Z. (2020). Role of nanoparticles on critical heat flux in convective boiling of nanofluids : Nanoparticle sedimentation and Brownian motion. International Journal of Heat and Mass Transfer, 150(January), 119299. https://doi.org/10.1016/j.ijheatmasstransfer.2019.119299

C, R. B., Kumar, P., Roy, S., & Ganesan, R. (2022). A comprehensive review on compound heat transfer enhancement using passive techniques in a heat exchanger. Materials Today: Proceedings, 54(23-October), 428–436. https://doi.org/10.1016/j.matpr.2021.09.541

Çengel, Y. A., & Cimbala, J. M. (2010). Heat and mass transfre Fundamentals and Application. In Tata McGraw Hill Education Private Limited.

Chakraborty, S., & Panigrahi, P. K. (2020). Stability of nano fl uid : A review. Applied Thermal Engineering, 174(March), 115259. https://doi.org/10.1016/j.applthermaleng.2020.115259

Chaurasia, S. R., & Sarviya, R. M. (2019). Experimental thermal performance analysis of fluid flow in a heat exchanger pipe with novel double strip helical screw tape inserts for utilization of energy resources. Energy Sources, Part A: Recovery, Utilization and Environmental Effects, 00(2-July), 1–14. https://doi.org/10.1080/15567036.2019.1669741

Chen, Q., & Ph, D. (2002). A Procedure for Verification , Validation , and Reporting of Indoor Environment CFD Analyses. Hvac\&R Research, 8(2), 201–216.

Chen, Z., Liu, P., Zare, A., Karimipour, A., Abdollahi, A., & Tlili, I. (2020). Evaluation of thermal conductivity of deionized water containing SDS-coated NiO nanoparticles under the in fl uences ofconstant and alternative varied magnetic fi elds. Powder Technology, 367(21-March), 143–156. https://doi.org/10.1016/j.powtec.2020.03.044

Cheng, Junlin and Qian, Zuoqin and Wang, Qiang and Fei, Chunguang and Huang, W. (2019). Numerical study of heat transfer and flow characteristic of twisted tube with different cross section shapes. Heat and Mass Transfer, 55(08 March), 823--844.

Cheng, L., Xia, G., & Thome, J. R. (2021). Flow boiling heat transfer and two-phase flow phenomena of CO_2 in macro- and micro-channel evaporators: Fundamentals, applications and engineering design. Applied Thermal Engineering, 195, 117070. https://doi.org/10.1016/j.applthermaleng.2021.117070

Chopkar, I., Sudarshan, S., Das, P. K., & Manna, I. (2008). Effect of particle size on thermal conductivity of nanofluid. Metallurgical and Materials Transactions A: Physical Metallurgy and Materials Science, 39(7), 1535–1542. https://doi.org/10.1007/s11661-007-9444-7

Coetzee, D., Venkataraman, M., Militky, J., & Petru, M. (2020). Influence of nanoparticles on thermal and electrical conductivity of composites. Polymers, 12(4), 2625. https://doi.org/10.3390/POLYM12040742

Dang, W., & Wang, L. (2021). Convective heat transfer enhancement mechanisms in circular tube inserted with a type of twined coil. International Journal of Heat and Mass Transfer, 169(23-January), 120960. https://doi.org/10.1016/j.ijheatmasstransfer.2021.120960

DiPippo, R. (2016). Elements of thermodynamics, fluid mechanics, and heat transfer applied to geothermal energy conversion systems.

Eastman, Jeffery A and Choi, US and Li, Shaoping and Thompson, LJ and Lee, S. (1995). Thermal Conductivity of Fluids. Ethane. In MRS Online Proceedings Library (OPL) (Vol. 457, Issue October, p. 3).

Eiamsa-Ard, S., Somkleang, P., Nuntadusit, C., & Thianpong, C. (2013). Heat transfer enhancement in tube by inserting uniform/non-uniform twisted-tapes with alternate axes: Effect of rotated-axis length. Applied Thermal Engineering, 54(1), 289–309. https://doi.org/10.1016/j.applthermaleng.2013.01.041

Engdar, U., & Klingmann, J. (2002). Investigation of Two-Equation Turbulence Models Applied to a Confined Axis-Symmetric Swirling Flow. In American Society of Mechanical Engineers, Pressure Vessels and Piping Division (Publication) PVP (Vol. 448, Issue 2). https://doi.org/10.1115/PVP2002-1590

Feizabadi, A., Khoshvaght-aliabadi, M., & Rahimi, A. B. (2019). Experimental evaluation of thermal performance and entropy generation inside a twisted U-tube equipped with twisted-tape inserts. International Journal of Thermal Sciences, 145(August), 106051.

Ganeshalingam, J. (2002). Swirl-induction for improved solid-liquid flow in pipes. PhD Thesis. University of Nottingham.

George, D. D. (2008). Effects of 4-lobe swirl- inducing pipe on pressure drop . MSc(Res) thesis, University of Nottingham.

Ghasemi, B., & Aminossadati, S. M. (2010). Brownian motion of nanoparticles in a triangular enclosure with natural convection. International Journal of Thermal Sciences, 49(6), 931–940. https://doi.org/10.1016/j.ijthermalsci.2009.12.017

Ghobadi, M., & Muzychka, Y. S. (2016). A Review of Heat Transfer and Pressure Drop Correlations for Laminar Flow in Curved Circular Ducts. Heat Transfer Engineering, 37(10), 815–839. https://doi.org/10.1080/01457632.2015.1089735

Goh, L. H. K., Hung, Y. M., Chen, G. M., & Tso, C. P. (2021). Entropy generation analysis of turbulent convection in a heat exchanger with self-rotating turbulator inserts. International Journal of Thermal Sciences, 160(October 2020), 106652. https://doi.org/10.1016/j.ijthermalsci.2020.106652

Göktepe, S., Atalik, K., & Ertürk, H. (2014). Comparison of single and two-phase models for nanofluid convection at the entrance of a uniformly heated tube. International Journal of Thermal Sciences, 80(1), 83–92. https://doi.org/10.1016/j.ijthermalsci.2014.01.014

Gorelikov, E. U., Naumov, I. V., Tsoy, M. A., & Shtern, V. N. (2021). Heat transfer in a centrifugal vortex tube. Journal of Physics: Conference Series, 2119(1). https://doi.org/10.1088/1742-6596/2119/1/012065

Guangbin, Y., Dejun, G., Juhui, C., Bing, D., Di, L., Ye, S., & Xi, C. (2016). Experimental Research on Heat Transfer Characteristics of CuO Nanofluid in Adiabatic Condition. Journal of Nanomaterials, 2016(1), 3693249. https://doi.org/10.1155/2016/3693249

Gulzar, O., Qayoum, A., & Gupta, R. (2021). Experimental study on thermal conductivity of mono and hybrid Al_2O_3–TiO_2 nanofluids for concentrating solar collectors. International Journal of Energy Research, 45(3), 4370–4384. https://doi.org/10.1002/er.6105

Gupta, M., Singh, V., & Said, Z. (2020). Heat transfer analysis using zinc Ferrite/water (Hybrid) nanofluids in a circular tube: An experimental investigation and development of new correlations for thermophysical and heat transfer properties. Sustainable Energy Technologies and Assessments, 39(April), 100720. https://doi.org/10.1016/j.seta.2020.100720

Gürdal, M., Arslan, K., Gedik, E., & Minea, A. A. (2022). Effects of using nanofluid, applying a magnetic field, and placing turbulators in channels on the convective heat transfer: A comprehensive review. Renewable and Sustainable Energy Reviews, 162(April), 112453. https://doi.org/10.1016/j.rser.2022.112453

Gustenyov, N., Egerer, M., Hultmark, M., Smits, A. J., & Bailey, S. C. C. (2023). Similarity of length scales in high-Reynolds-number wall-bounded flows. Journal of Fluid Mechanics, 965(8-May), A17. https://doi.org/10.1017/jfm.2023.417

Habibishandiz, M., & Saghir, M. Z. (2022). A critical review of heat transfer enhancement methods in the presence of porous media , nanofluids , and microorganisms. Thermal Science and Engineering Progress, 30(March), 101267. https://doi.org/10.1016/j.tsep.2022.101267

Hangi, M., Rahbari, A., Wang, X., & Lipiński, W. (2022). Hydrothermal characteristics of fluid flow in a circular tube fitted with free rotating axial-turbine-type swirl generators: Design, swirl strength, and performance analyses. International Journal of Thermal Sciences, 173(November 2021), 107384. https://doi.org/10.1016/j.ijthermalsci.2021.107384

Hasan, H. A., Hatem, A. A., Abd, L. A., Abed, A. M., & Sopian, K. (2022). Numerical investigation of nanofluids comprising different metal oxide nanoparticles for cooling concentration photovoltaic thermal CPVT. Cleaner Engineering and Technology, 10(July), 100543. https://doi.org/10.1016/j.clet.2022.100543

He, K., Chen, N., Wang, C., Wei, L., & Chen, J. (2018). Method for Determining Crystal Grain Size by X-Ray Diffraction. Crystal Research and Technology, 53(2), 1–6. https://doi.org/10.1002/crat.201700157

Hellsten, A. (1997). Extension of the k-omega-SST turbulence model for flows over rough surfaces.

Hemmat Esfe, M., Abbasian Arani, A. A., Shafiei Badi, R., & Rejvani, M. (2018). ANN modeling, cost performance and sensitivity analyzing of thermal conductivity of DWCNT–SiO_2/EG hybrid nanofluid for higher heat transfer: An experimental study. Journal of Thermal Analysis and Calorimetry, 131(3), 2381–2393. https://doi.org/10.1007/s10973-017-6744-z

Hemmat Esfe, M., Afrand, M., Yan, W. M., & Akbari, M. (2015). Applicability of artificial neural network and nonlinear regression to predict thermal conductivity modeling of Al2O3-water nanofluids using experimental data. International Communications in Heat and Mass Transfer, 66, 246–249. https://doi.org/10.1016/j.icheatmasstransfer.2015.06.002

Hemmat Esfe, M., Kiannejad Amiri, M., & Alirezaie, A. (2018). Thermal conductivity of a hybrid nanofluid: A new economic strategy and model. Journal of Thermal Analysis and Calorimetry, 134(2), 1113–1122. https://doi.org/10.1007/s10973-017-6836-9

Hemmat, M., & Seyfolah, E. (2015). Turbulent forced convection heat transfer and thermophysical properties of Mgo – water nanofluid with consideration of different nanoparticles diameter , an empirical study. Journal of Thermal Analysis and Calorimetry, 119(16-Octobe), 1205–1213. https://doi.org/10.1007/s10973-014-4197-1

Hermansen, Ø. F. (2021). Transient flow analysis of opening hinged/sliding door. https://hdl.handle.net/11250/2772543

Hilo, A. K., Talib, A. R. A., Iborra, A. A., Sultan, M. T. H., & Hamid, M. F. A. (2020a). Experimental study of nanofluids flow and heat transfer over a backward-facing step channel. Powder Technology, 372, 497–505. https://doi.org/10.1016/j.powtec.2020.06.013

Hilo, A. K., Talib, A. R. A., Iborra, A. A., Sultan, M. T. H., & Hamid, M. F. A. (2020b). Experimental study of nanofluids flow and heat transfer over a backward-facing step channel. Powder Technology, 372, 497–505. https://doi.org/10.1016/j.powtec.2020.06.013

Hirsch, C. (2007). Numerical computation of internal and external flows: The fundamentals of computational fluid dynamics. Elsevier.

Hoekstra, A. J., Derksen, J. J., & Van Den Akker, H. E. A. (1999). An experimental and numerical study of turbulent swirling flow in gas cyclones. Chemical Engineering Science, 54(13–14), 2055–2065. https://doi.org/10.1016/S0009-2509(98)00373-X

Huang, H., Sun, T., Li, N., & Zhang, G. (2022). Sensitization of the modified SST model to the swirling and curvature for turbulent impinging jet heat transfer. International Journal of Heat and Mass Transfer, 182(24-septemper 2021), 121980. https://doi.org/10.1016/j.ijheatmasstransfer.2021.121980

Hunt, J. C. R., & Morrison, J. F. (2000). Eddy structure in turbulent boundary layers. European Journal of Mechanics-B/Fluids, 19(27-March), 673–694.

Hwang, Y., Lee, J. K., Lee, J. K., Jeong, Y. M., Cheong, S. ir, Ahn, Y. C., & Kim, S. H. (2008). Production and dispersion stability of nanoparticles in nanofluids. Powder Technology, 186(2), 145–153. https://doi.org/10.1016/j.powtec.2007.11.020

Indurain, B., Uystepruyst, D., Beaubert, F., Lalot, S., & Helgadóttir. (2020). Numerical investigation of several twisted tubes with non-conventional tube cross sections on heat transfer and pressure drop. Journal of Thermal Analysis and Calorimetry, 140(3), 1555–1568. https://doi.org/10.1007/s10973-019-08965-4

Iyer, J., Moore, T., Nguyen, D., Roy, P., & Stolaroff, J. (2022). Heat transfer and pressure drop characteristics of heat exchangers based on triply periodic minimal and periodic nodal surfaces. Applied Thermal Engineering, 209(August 2021), 118192. https://doi.org/10.1016/j.applthermaleng.2022.118192

Jafari, M., Dabiri, S., Farhadi, M., & Sedighi, K. (2017). Effects of a three-lobe swirl generator on the thermal and flow fields in a heat exchanging tube: An experimental and numerical approach. Energy Conversion and Management, 148, 1358–1371. https://doi.org/10.1016/j.enconman.2017.06.074

Jafari, M., Farhadi, M., & Sedighi, K. (2017a). An experimental study on the effects of a new swirl generator on thermal performance of a circular tube. International Communications in Heat and Mass Transfer, 87(August), 277–287. https://doi.org/10.1016/j.icheatmasstransfer.2017.07.016

Jafari, M., Farhadi, M., & Sedighi, K. (2017b). Thermal performance enhancement in a heat exchanging tube via a four-lobe swirl generator : An experimental and numerical approach. Applied Thermal Engineering, 124, 883–896. https://doi.org/10.1016/j.applthermaleng.2017.06.095

Jamilpanah, P., Pahlavanzadeh, H., & Kheradmand, A. (2016). Thermal conductivity , viscosity , and electrical conductivity of iron oxide with a cloud fractal structure. Heat and Mass Transfer, 53(4-Jan), 1343--1354. https://doi.org/10.1007/s00231-016-1891-5

Jin, C., Wu, Q., Yang, G., Zhang, H., & Zhong, Y. (2021). Investigation on hybrid nanofluids based on carbon nanotubes filled with metal nanoparticles: Stability, thermal conductivity, and viscosity. Powder Technology, 389(5-May), 1–10. https://doi.org/10.1016/j.powtec.2021.05.007

Kamel, M. S., Al-Oran, O., & Lezsovits, F. (2020). Thermal conductivity of al2 o3 and ceo2 nanoparticles and their hybrid based water nanofluids: An experimental study. Periodica Polytechnica Chemical Engineering, 65(1), 50–60. https://doi.org/10.3311/PPch.15382

Kanti, P., Sharma, K. V., Khedkar, R. S., & Rehman, T. ur. (2022). Synthesis, characterization, stability, and thermal properties of graphene oxide based hybrid nanofluids for thermal applications: Experimental approach. Diamond and Related Materials, 128(May), 109265. https://doi.org/10.1016/j.diamond.2022.109265

Karakoyun, Y., Acikgoz, O., Çebi, A., Koca, A., Çetin, G., Dalkilic, A. S., & Wongwises, S. (2021). A Comprehensive Approach to Analyze the Discrepancies in Heat Transfer Characteristics Pertaining to Radiant Ceiling Heating System. Applied Thermal Engineering, 187(23-December), 116517. https://doi.org/10.1016/j.applthermaleng.2020.116517

Kausar, R., Muhammad, H., Farid, A., & Riaz, M. (2023). A Numerically Validated Approach to Modeling Water Hammer Phenomena Using Partial Differential Equations and Switched Differential-Algebraic Equations. J. Ind. Intell, 1(2), 75–86. https://doi.org/https://doi.org/10.56578/jii010201.

Kazemi, I., Sefid, M., & Afrand, M. (2020). Improving the thermal conductivity of water by adding mono & hybrid nano-additives containing graphene and silica: A comparative experimental study. International Communications in Heat and Mass Transfer, 116, 104648. https://doi.org/10.1016/j.icheatmasstransfer.2020.104648

Khashi'ie, N. S., Waini, I., Kasim, A. R. M., Zainal, N. A., Arifin, N. M., & Pop, I. (2022). Thermal progress of a non-Newtonian hybrid nanofluid flow on a permeable Riga plate with temporal stability analysis. Chinese Journal of Physics, 77(March), 279–290. https://doi.org/10.1016/j.cjph.2022.03.019

Khoshvaght-aliabadi, M., & Ghods-nahry, E. A. (2023). Performance evaluation of serpentine tube coupled with modified twisted tapes utilized as heat extraction coil in solar ponds. Solar Energy, 255(March), 191–207. https://doi.org/10.1016/j.solener.2023.03.035

Kline, S., & McClintock, F. (1953). Describing uncertainties in single-sample experiments. Mechanical Engineering, 75, 3–8.

Kong, M., & Lee, S. (2020). Performance evaluation of Al2O3 nanofluid as an enhanced heat transfer fluid. Advances in Mechanical Engineering, 12(8), 1–13. https://doi.org/10.1177/1687814020952277

Kumar, D., Patil, A. K., & Kumar, M. (2020). Experimental investigation of heat transfer and fluid flow in a circular tube with lanced ring insert. Experimental Heat Transfer, 33(6), 560–571. https://doi.org/10.1080/08916152.2019.1691086

Kumar, E. P., Solanki, A. K., & Kumar, M. M. J. (2021). Numerical investigation of heat transfer and pressure drop characteristics in the micro-fin helically coiled tubes. Applied Thermal Engineering, 182(May 2020), 116093. https://doi.org/10.1016/j.applthermaleng.2020.116093

Kumar, S., Dinesha, P., Narayanan, A., & Nanda, R. (2019). Parametric study on the heat transfer characteristics in a circular tube with helical tape insert under laminar flow conditions. Heat Transfer - Asian Research, 48(7), 3384–3398. https://doi.org/10.1002/htj.21553

Lange, C., Barthelmäs, P., Rosnitschek, T., Tremmel, S., & Rieg, F. (2021). Impact of HPC and Automated CFD Simulation Processes on Virtual Product Development—A Case Study. Applied Sciences, 11(15-July), 6552. https://doi.org/https://doi.org/10.3390/app11146552

Laurens, V. H., Dieter, B., & S, P. G. (2023). Experimental methods in chemical engineering : Computational fluid dynamics / finite volume method — CFD / FVM. The Canadian Journal of Chemical Engineering, 101(28-July), 545–561. https://doi.org/https://doi.org/10.1002/CJCE.24571

Li, Guozhen and Tang, Llewellyn and Zhang, Xingxing and Dong, J. (2019). A review of factors affecting the efficiency of clean-in-place procedures in closed processing systems. Energy, 178(1 July), 57–71. https://doi.org/https://doi.org/10.1016/j.energy.2019.04.123

Li, G. (2016). Investigation of swirl pipe for improving cleaning efficiency in closed processing system.PhD Thesis. University of Nottingham.

Li, G., Hall, P., Miles, N., & Wu, T. (2015a). Improving the efficiency of 'Clean-In-Place' procedures using a four-lobed swirl pipe: A numerical investigation. Computers & Fluids, 108, 116–128. https://doi.org/10.1016/j.compfluid.2014.11.032

Li, G., Hall, P., Miles, N., & Wu, T. (2015b). Optimization of a four-lobed swirl pipe for Clean-In-Place procedures. International Journal of Environmental, 9(6), 689–697. https://doi.org/10.13140/RG.2.1.4838.0004

Li, H., Wang, L., He, Y., Hu, Y., Zhu, J., & Jiang, B. (2015). Experimental investigation of thermal conductivity and viscosity of ethylene glycol based ZnO nanofluids. Applied Thermal Engineering, 88(20-June), 363–368. https://doi.org/10.1016/j.applthermaleng.2014.10.071

Li, M., Khan, T. S., Al-Hajri, E., & Ayub, Z. H. (2016). Single phase heat transfer and pressure drop analysis of a dimpled enhanced tube. Applied Thermal Engineering, 101(19-March), 38–46. https://doi.org/10.1016/j.applthermaleng.2016.03.042

Li, Y., Kalbasi, R., Nguyen, Q., & Afrand, M. (2020). Effects of sonication duration and nanoparticles concentration on thermal conductivity of silica-ethylene glycol nanofluid under different temperatures: An experimental study. Powder Technology, 367, 464–473. https://doi.org/10.1016/j.powtec.2020.03.058

Lin, H., Jian, Q., Bai, X., Li, D., Huang, Z., Huang, W., Feng, S., & Cheng, Z. (2023). Recent advances in thermal conductivity and thermal applications of graphene and its derivatives nanofluids. Applied Thermal Engineering, 218(July 2022), 119176. https://doi.org/10.1016/j.applthermaleng.2022.119176

Lindroos, T. J., Mäki, E., Koponen, K., Hannula, I., Kiviluoma, J., & Raitila, J. (2021). Replacing fossil fuels with bioenergy in district heating – Comparison of technology options. Energy, 231(12 May), 120799. https://doi.org/10.1016/j.energy.2021.120799

Liu, H., Joseph, A., Elsayad, M. M., Elshernoby, B., Awad, F., Elsharkawy, M., Kandeal, A. W., Hussien, A. A., An, M., & Sharshir, S. W. (2022). Recent advances in heat pump-coupled desalination systems: A systematic review. Desalination, 543(May), 116081. https://doi.org/10.1016/j.desal.2022.116081

Liu, M. S., Lin, M. C. C., Huang, I. Te, & Wang, C. C. (2006). Enhancement of thermal conductivity with CuO for nanofluids. Chemical Engineering and Technology, 29(1), 72–77. https://doi.org/10.1002/ceat.200500184

Liu, Y., Rao, Y., & Weigand, B. (2019). Heat transfer and pressure loss characteristics in a swirl cooling tube with dimples on the tube inner surface. International Journal of Heat and Mass Transfer, 128, 54–65. https://doi.org/10.1016/j.ijheatmasstransfer.2018.08.097

Ma, M., Zhai, Y., Yao, P., Li, Y., & Wang, H. (2020). Synergistic mechanism of thermal conductivity enhancement and economic analysis of hybrid nanofluids. Powder Technology, 373, 702–715. https://doi.org/10.1016/j.powtec.2020.07.020

Maheshwary, P. B., Handa, C. C., & Nemade, K. R. (2017). A comprehensive study of effect of concentration , particle size and particle shape on thermal conductivity of titania / water based nanofluid. Applied Thermal Engineering, 119(3-March), 79–88. https://doi.org/10.1016/j.applthermaleng.2017.03.054

Maheshwary, P. B., Handa, C. C., Nemade, K. R., & Chaudhary, S. R. (2019). Role of nanoparticle shape in enhancing the thermal conductivity of nanofluids. Materials Today: Proceedings, 28(26-December), 873–878. https://doi.org/10.1016/j.matpr.2019.12.315

Malika, M., & Sonawane, S. S. (2022). The sono-photocatalytic performance of a Fe_2O_3 coated TiO_2 based hybrid nanofluid under visible light via RSM. Colloids and Surfaces A: Physicochemical and Engineering Aspects, 641(December 2021), 128545. https://doi.org/10.1016/j.colsurfa.2022.128545

Manca, O., Nardini, S., & Ricci, D. (2012). A numerical study of nanofluid forced convection in ribbed channels. Applied Thermal Engineering, 37, 280–292. https://doi.org/10.1016/j.applthermaleng.2011.11.030

Mani, M., & Dorgan, A. J. (2023). A Perspective on the State of Aerospace Computational Fluid Dynamics Technology. Annual Review of Fluid Mechanics, 55(25 July), 431–457. https://doi.org/https://doi.org/10.1002/cjce.24571

McEligoi, D. M. (1970). Fundamentals of momentum, heat and mass transfer. In International Journal of Heat and Mass Transfer (Vol. 13, Issue 10). https://doi.org/10.1016/0017-9310(70)90063-3

Megia, P. J., Vizcaino, A. J., Calles, J. A., & Carrero, A. (2021). Hydrogen Production Technologies: From Fossil Fuels toward Renewable Sources. A Mini Review. Energy and Fuels, 35(20), 16403–16415. https://doi.org/10.1021/acs.energyfuels.1c02501

Mehta, B., Subhedar, D., Panchal, H., & Said, Z. (2022). Synthesis , stability , thermophysical properties and heat transfer applications of nanofluid – A review. Journal of Molecular Liquids, 364(20-July), 120034. https://doi.org/10.1016/j.molliq.2022.120034

Menter, F. R. (1993). Zonal two equation kw turbulence models for aerodynamic flows. https://doi.org/https://doi.org/10.2514/6.1993-2906

Michael Joseph Stalin, P., Arjunan, T. V., Matheswaran, M. M., Manoj Kumar, P., & Sadanandam, N. (2020). Investigations on thermal properties of CeO2/water nanofluids for heat transfer applications. Materials Today: Proceedings, 47(6-May), 6815–6820. https://doi.org/10.1016/j.matpr.2021.05.137

Mohammed, H. A., Hasan, H. A., & Wahid, M. A. (2013). Heat transfer enhancement of nano fl uids in a double pipe heat exchanger with louvered strip inserts ☆. International Communications in Heat and Mass Transfer, 40(November), 36 – 46. https://doi.org/10.1016/j.icheatmasstransfer.2012.10.023

Moin, P. (2016). Fundamentals of Engineering Numerical Analysis (Issue April 2002). https://doi.org/10.1139/l02-006

Mousa, M. H., Miljkovic, N., & Nawaz, K. (2021). Review of heat transfer enhancement techniques for single phase flows. Renewable and Sustainable Energy Reviews, 137(September 2020), 110566. https://doi.org/10.1016/j.rser.2020.110566

Nadeem, S., Shah, A., Shahabuddin, S., Faizul, M., Sabri, M., Faiz, M., Salleh, M., Azlin, M., Hayat, N., Azwadi, N., Sidik, C., Samykano, M., & Saidur, R. (2020). International Journal of Heat and Mass Transfer Experimental investigation on stability , thermal conductivity and rheological properties of rGO / ethylene glycol based nanofluids. International Journal of Heat and Mass Transfer, 150(24-May), 118981. https://doi.org/10.1016/j.ijheatmasstransfer.2019.118981

Najafi, A. F., Mousavian, S. M., & Amini, K. (2011). Numerical investigations on swirl intensity decay rate for turbulent swirling flow in a fixed pipe. International Journal of Mechanical Sciences, 53(10), 801–811. https://doi.org/10.1016/j.ijmecsci.2011.06.011

Nikoozadeh, A., Behzadmehr, A., & Payan, S. (2020). Numerical investigation of turbulent heat transfer enhancement using combined propeller-type turbulator and nanofluid in a circular tube. Journal of Thermal Analysis and Calorimetry, 140(3), 1029–1044. https://doi.org/10.1007/s10973-019-08578-x

Omar Al-Abbasi. (2019). Numerical Study and Second Law Analysis of Propeller-Type Vortex Generator in A Circular Pipe Flow. International Journal of Engineering Research And, V8(10), 65–84. https://doi.org/10.17577/ijertv8is100059

Omidi, M., & Farhadi, M. (2018). Numerical study on the effect of using spiral tube with lobed cross section in double-pipe heat exchangers. Journal of Thermal Analysis and Calorimetry, 0123456789(3), 2397--2408. https://doi.org/10.1007/s10973-018-7579-y

Omidi, M., Farhadi, M., & Rabienataj, A. A. (2018). Numerical study of heat transfer on using lobed cross sections in helical coil heat exchangers : E ff ect of physical and geometrical parameters. Energy Conversion and Management, 176(September), 236–245. https://doi.org/10.1016/j.enconman.2018.09.034

Omidi, M., Rabienataj, A. A., Mousa, D., Rabienataj Darzi, A. A., & Farhadi, M. (2019). Turbulent heat transfer and fluid flow of alumina nanofluid inside three-lobed twisted tube. Journal of Thermal Analysis and Calorimetry, 137(4), 1451–1462. https://doi.org/10.1007/s10973-019-08026-w

Oneissi, M., Habchi, C., Russeil, S., Bougeard, D., & Lemenand, T. (2016). Novel design of delta winglet pair vortex generator for heat transfer enhancement. International Journal of Thermal Sciences, 109, 1–9. https://doi.org/10.1016/j.ijthermalsci.2016.05.025

Oz, F., San, O., & Kara, K. (2023). An efficient quantum partial differential equation solver with chebyshev points. Scientific Reports, 13(1), 1–16. https://doi.org/10.1038/s41598-023-34966-3

Pang, X., Huo, Y., Fang, H., & Rao, Z. (2021). Analysis of temperature uniformity of electric vehicle battery system with swirling flow strengthened heat transfer. Applied Thermal Engineering, 193(April), 116995. https://doi.org/10.1016/j.applthermaleng.2021.116995

Patel, A. (2023). Enhancing Heat Transfer Efficiency in Solar Thermal Systems Using Advanced Heat Exchangers. Multidisciplinary International Journal of Research and Development (MIJRD), 2(6), 31–51.

Patil, R. H. (2019). Fluid flow and heat transfer analogy for laminar and turbulent flow inside spiral tubes. International Journal of Thermal Sciences, 139(December 2018), 362–375. https://doi.org/10.1016/j.ijthermalsci.2019.01.036

Patil, S. V., & Babu, P. V. V. (2011). Heat Transfer Augmentation in a Circular tube and Squareduct Fitted with Swirl Flow Generators: A Review. International Journal of Chemical Engineering and Applications, 2(5), 326–331. https://doi.org/10.7763/ijcea.2011.v2.128

Pavia, M., Alajami, K., Estellé, P., Desforges, A., & Vigolo, B. (2021). A critical review on thermal conductivity enhancement of graphene-based nanofluids. Advances in Colloid and Interface Science, 294, 102452.

Pifre, A. (2017). Solar Thermal Electricity and Solar Insolation. https://doi.org/10.1016/B978-0-12-803022-6.00007-1

Pourrajab, R., Noghrehabadi, A., Behbahani, M., & Hajidavalloo, E. (2021). An efficient enhancement in thermal conductivity of water-based hybrid nanofluid containing MWCNTs-COOH and Ag nanoparticles: experimental study. Journal of Thermal Analysis and Calorimetry, 143(5), 3331–3343. https://doi.org/10.1007/s10973-020-09300-y

Promvonge, P. (2008). Thermal augmentation in circular tube with twisted tape and wire coil turbulators. Energy Conversion and Management, 49(11), 2949–2955. https://doi.org/10.1016/j.enconman.2008.06.022

Raylor, B. (1998). Pipe Design for Improved Particle Distribution and Improved Wear, PhD thesis, University of Nottingham. Access.

Reduction, P. D. (2024). Analyzing the Efficacy of Nickel Plating Coating in Hydraulic. Lubricants, 12(23 January), 37.

Rejvani, M., Alipour, A., & Masoud, S. (2019). Optimal characteristics and heat transfer efficiency of SiO 2 / water nanofluid for application of energy devices : A comprehensive study. February, 1–24. https://doi.org/10.1002/er.4854

Reza, V., Abouei, A., & Karimi-maleh, H. (2023). A numerical solution of fractional reaction–convection–diffusion for modeling PEM fuel cells based on a meshless approach Vahid. Engineering Analysis with Boundary Elements, 155(June), 707–716.

Royds, R. (1921). Heat transmission by radiation, conduction and convection, first ed., Constable and Camp. Ltd., London.

Safaei, M. R., Ranjbarzadeh, R., Hajizadeh, A., Bahiraei, M., Afrand, M., & Karimipour, A. (2019). Effects of cobalt ferrite coated with silica nanocomposite on the thermal conductivity of an antifreeze: New nanofluid for refrigeration condensers. International Journal of Refrigeration, 102(23-December), 86–95. https://doi.org/10.1016/j.ijrefrig.2018.12.007

Safiei, W., Rahman, M. M., Yusoff, A. R., & Radin, M. R. (2020). Preparation, stability and wettability of nanofluid: A review. Journal of Mechanical Engineering and Sciences, 14(3), 7244–7257. https://doi.org/10.15282/jmes.14.3.2020.24.0569

Sahel, D., Ameur, H., & Mellal, M. (2020). Effect of tube shape on the performance of a fin and tube heat exchanger. Journal of Mechanical Engineering and Sciences, 14(2), 6709–6718. https://doi.org/10.15282/JMES.14.2.2020.13.0525

Said, Z., Sundar, L. S., Tiwari, A. K., Ali, H. M., Sheikholeslami, M., Bellos, E., & Babar, H. (2022). Recent advances on the fundamental physical phenomena behind stability, dynamic motion, thermophysical properties, heat transport, applications, and challenges of nanofluids. Physics Reports, 946(1-July), 1–94. https://doi.org/10.1016/j.physrep.2021.07.002

Sajid, M. U., & Ali, H. M. (2018). Thermal conductivity of hybrid nanofluids: A critical review. International Journal of Heat and Mass Transfer, 126(11-May), 211–234. https://doi.org/10.1016/j.ijheatmasstransfer.2018.05.021

Salman, S., Talib, A. R. A., Saadon, S., & Sultan, M. T. H. (2020). Hybrid nanofluid flow and heat transfer over backward and forward steps: A review. Powder Technology, 363, 448–472. https://doi.org/10.1016/j.powtec.2019.12.038

Saraç, B. A., & Bali, T. (2007). An experimental study on heat transfer and pressure drop characteristics of decaying swirl flow through a circular pipe with a vortex generator. Experimental Thermal and Fluid Science, 32(1), 158–165. https://doi.org/10.1016/j.expthermflusci.2007.03.002

Shadab, M., Karimipour, M., Najafi, A. F., Paydar, R., & Nourbakhsh, S. A. (2022). Effect of impeller shroud trimming on the hydraulic performance of centrifugal pumps with low and medium specific speeds. Engineering Applications of Computational Fluid Mechanics, 16(1), 514–535. https://doi.org/10.1080/19942060.2021.2016492

Sharma, A. (2021). Introduction to computational fluid dynamics: development, application and analysis. https://doi.org/https://doi,org/10.1007/978-3-030-72884-7

Sharma, R., Chauhan, P., Sharma, A. K., Katiyar, A., Singh, H. K., Rinawa, M. L., & Kumar, P. M. (2022). Characterization of ZnO/nanofluid for improving heat transfer in thermal systems. Materials Today: Proceedings, 62(20-january), 1904–1908. https://doi.org/10.1016/j.matpr.2022.01.107

Shi, W., Liu, T., Song, K., Zhang, Q., Hu, W., & Wang, L. (2021). The optimal longitudinal location of curved winglets for better thermal performance of a finned-tube heat exchanger. International Journal of Thermal Sciences, 167(April), 107035. https://doi.org/10.1016/j.ijthermalsci.2021.107035

Siba, M., Wanmahmood, W., Zaki Nuawi, M., Rasani, R., & Nassir, M. (2016). Flow-induced vibration in pipes: Challengess and solutions - A review. Journal of Engineering Science and Technology, 11(3), 362–382.

Sica, L. U. R., Nobre, G. C. M., Contreras, E. M. C., Bandarra, E. P., Sotomayor, P. O., & Parise, J. A. R. (2021). Heat transfer nanofluids for trigeneration systems : fabrication and experimental investigation of viscosity at Heat transfer nanofluids for trigeneration systems: fabrication and experimental investigation of viscosity at below-ambient temperatures. International Journal of Refrigeration, 129(9-May-2021), 163–174. https://doi.org/10.1016/j.ijrefrig.2021.04.036

Singh, J., Kumar, R., Gupta, M., & Kumar, H. (2020). Thermal conductivity analysis of GO-CuO/DW hybrid nanofluid. Materials Today: Proceedings, 28(May-2020), 1714–1718. https://doi.org/10.1016/j.matpr.2020.05.134

Singh, R. P., Sharma, K., & Tiwari, A. K. (2019). An Experimental Investigation of Thermal Conductivity of TiO 2 Nanofluid : Proposing a New Correlation. Jornal of Scientific & Industrial Research, 78(September), 620–623.

Sun, Y., Wen, G., Xiao, X., Ren, B., Yang, N., & Zhang, L. (2018). Numerical Study on Heat Transfer and Flow Characteristics for Laminar Flow in a Circular Tube with Swirl Generators. Transactions of Tianjin University, 24(3), 244–255. https://doi.org/10.1007/s12209-018-0132-z

Tahani, M., Vakili, M., & Khosrojerdi, S. (2016). Experimental evaluation and ANN modeling of thermal conductivity of graphene oxide nanoplatelets/deionized water nanofluid. International Communications in Heat and Mass Transfer, 76, 358–365. https://doi.org/10.1016/j.icheatmasstransfer.2016.06.003

Taheran, E., & Javaherdeh, K. (2019). Experimental investigation on the effect of inlet swirl generator on heat transfer and pressure drop of non-Newtonian nanofluid. Applied Thermal Engineering, 147(March 2018), 551–561. https://doi.org/10.1016/j.applthermaleng.2018.07.142

Taherialekouhi, R., Rasouli, S., & Khosravi, A. (2019). An experimental study on stability and thermal conductivity of water-graphene oxide/aluminum oxide nanoparticles as a cooling hybrid nanoflui. International Journal of Heat and Mass Transfer, 145(16-September), 118751. https://doi.org/10.1016/j.ijheatmasstransfer.2019.118751

Tahmasebi Sulgani, M., & Karimipour, A. (2019). Improve the thermal conductivity of 10w40-engine oil at various temperature by addition of Al 2 O 3 /Fe 2 O 3 nanoparticles. Journal of Molecular Liquids, 283(24-March), 660–666. https://doi.org/10.1016/j.molliq.2019.03.140

Tanda, G., & Satta, F. (2021). Heat transfer and friction in a high aspect ratio rectangular channel with angled and intersecting ribs. International Journal of Heat and Mass Transfer, 169(19-January), 120906. https://doi.org/10.1016/j.ijheatmasstransfer.2021.120906

Tang, X., Dai, X., & Zhu, D. (2015a). Experimental and numerical investigation of convective heat transfer and fluid flow in twisted spiral tube. International Journal of Heat and Mass Transfer, 90, 523–541. https://doi.org/10.1016/j.ijheatmasstransfer.2015.06.068

Tang, X., Dai, X., & Zhu, D. (2015b). Experimental and numerical investigation of convective heat transfer and fluid flow in twisted spiral tube. International Journal of Heat and Mass Transfer, 90(23-June), 523–541. https://doi.org/10.1016/j.ijheatmasstransfer.2015.06.068

Tian, S., Izza, N., Toghraie, D., & Eftekhari, S. A. (2021). Using perceptron feed-forward Artificial Neural Network (ANN) for predicting the thermal conductivity of graphene oxide-Al2O3/water-ethylene glycol hybrid nanofluid. Case Studies in Thermal Engineering, 26(April), 101055. https://doi.org/10.1016/j.csite.2021.101055

Tomar, M., & Kumar, N. (2020). Effect of multi-walled carbon nanotubes and alumina nano-additives in a light duty diesel engine fuelled with schleichera oleosa biodiesel blends. Sustainable Energy Technologies and Assessments, 42(September), 100833. https://doi.org/10.1016/j.seta.2020.100833

Tombs, M. C. (2014). John C. Crittenden, R. Rhodes Trussell, David W. Hand, Kerry J. Howe, George Tchobanoglous: MWH Water Treatment Principles and Design. Third Edition. Chromatographia, 77(5–6), 527–528. https://doi.org/10.1007/s10337-013-2600-x

Tonkin, R. J. J. (2005). Swirling Pipeflow of Non · Newtonian and Particle · Laden Fluids.

Vasta, M. (2014). Mathematical modeling and simulation: introduction for scientists and engineers (Issue May). John Wiley \& Sons. https://doi.org/10.1007/s11012-009-9215-1

Vinchurkar, S., & Longest, P. W. (2008). Evaluation of hexahedral, prismatic and hybrid mesh styles for simulating respiratory aerosol dynamics. Computers and Fluids, 37(3), 317–331. https://doi.org/10.1016/j.compfluid.2007.05.001

Wanatasanapan, V. V., Abdullah, M. Z., & Gunnasegaran, P. (2020). Effect of TiO2-Al_2O_3nanoparticle mixing ratio on the thermal conductivity, rheological properties, and dynamic viscosity of water-based hybrid nanofluid. Journal of Materials Research and Technology, 9(6), 13781–13792. https://doi.org/10.1016/j.jmrt.2020.09.127

Wang, Yifan, Liu, P., Shan, F., Liu, Z., & Liu, W. (2019). Effect of longitudinal vortex generator on the heat transfer enhancement of a circular tube. Applied Thermal Engineering, 148(19-November), 1018–1028. https://doi.org/10.1016/j.applthermaleng.2018.11.080

Wang, Yongji, Liu, P., Xiao, H., Liu, Z., & Liu, W. (2022). Design and optimization on symmetrical wing longitudinal swirl generators in circular tube for laminar flow. International Journal of Heat and Mass Transfer, 193(29-April), 122961. https://doi.org/10.1016/j.ijheatmasstransfer.2022.122961

Webb, R. L. (1981). OF ENHANCED HEAT TRANSFER SURFACES IN HEAT EXCHANGER DESIGN. 24(4), 715–726.

Webb RL, K. N.-H. (1994). Principles of enhanced heat transfer. Taylor Francis, New York.

Wróblewski, W., & Fraczek, D. (2014). Heat transfer modelling in a rotating cavity using the SST k-ω turbulence model. Archives of Mechanics, 66(5), 343–364.

Xie, G., Liu, X., Yan, H., & Qin, J. (2017). Turbulent flow characteristics and heat transfer enhancement in a square channel with various crescent ribs on one wall. International Journal of Heat and Mass Transfer, 115(3-July), 283–295. https://doi.org/10.1016/j.ijheatmasstransfer.2017.07.012

Yan, T., Qu, J., Sun, X., Chen, Y., Hu, Q., & Li, W. (2020). Numerical evaluation on the decaying swirling flow in a multi-lobed swirl generator. Engineering Applications of Computational Fluid Mechanics, 14(1), 1198–1214. https://doi.org/10.1080/19942060.2020.1816494

Yilmaz, M., Comakli, O., Yapici, S., & Sara, O. N. (2003). Heat transfer and friction characteristics in decaying swirl flow generated by different radial guide vane swirl generators. Energy Conversion and Management, 44(2), 283–300. https://doi.org/10.1016/S0196-8904(02)00053-5

Yin, P., Mohamed, Y., Bashar, B. S., Maher, M., Zahra, A., Mohammed, M., Al, R., Majed, H., Alhani, I., Salaam, E., & Hadrawi, S. K. (2023). Evaluation of efficiency, thermohydraulic performance evaluation criterion, and field synergy principle improvement of the parabolic solar collector containing the hybrid nanofluid using spring turbulators. Case Studies in Thermal Engineering, 41(November 2022), 102571. https://doi.org/10.1016/j.csite.2022.102571

You, Y., Seibold, F., Wang, S., Weigand, B., & Gross, U. (2020). URANS of turbulent flow and heat transfer in divergent swirl tubes using the k - ω SST turbulence model with curvature correction. International Journal of Heat and Mass Transfer, 159, 120088. https://doi.org/10.1016/j.ijheatmasstransfer.2020.120088

Younes, H., Mao, M., Sohel Murshed, S. M., Lou, D., Hong, H., & Peterson, G. P. (2022). Nanofluids: Key parameters to enhance thermal conductivity and its applications. Applied Thermal Engineering, 207(February), 118202. https://doi.org/10.1016/j.applthermaleng.2022.118202

Yuan, S., & Zhu, W. (2023). A Cartesian spatial discretization method for nonlinear dynamic modeling and vibration analysis of tensegrity structures. International Journal of Solids and Structures, 270(5 January), 112179. https://doi.org/10.1016/j.ijsolstr.2023.112179

Yurddas, A. (2022). Numerical analysis of heat transfer of a nanofluid counter-flow heat exchanger. International Communications in Heat and Mass Transfer, 137, 106306. https://doi.org/10.1016/j.icheatmasstransfer.2022.106306

Zaboli, M., Saedodin, S., Mousavi Ajarostaghi, S. S., & Nourbakhsh, M. (2021). Numerical evaluation of the heat transfer in a shell and corrugated coil tube heat exchanger with three various water-based nanofluids. Heat Transfer, 50(6), 6043–6067. https://doi.org/10.1002/htj.22161

Zakaria, I. A., Mohamed, W. A. N. W., Azid, N. H. A., Suhaimi, M. A., & Azmi, W. H. (2022). Heat transfer and electrical discharge of hybrid nanofluid coolants in a fuel cell cooling channel application. Applied Thermal Engineering, 210(August 2021), 118369. https://doi.org/10.1016/j.applthermaleng.2022.118369

Zhang, J., Diao, Y., Zhao, Y., Zhang, Y., & Sun, Q. (2014). International Journal of Thermal Sciences Thermal-hydraulic performance of multiport microchannel fl at tube with a sawtooth fi n structure. International Journal of Thermal Sciences, 84, 175–183. https://doi.org/10.1016/j.ijthermalsci.2014.05.018

Zheng, N., Yan, F., Zhang, K., Zhou, T., & Sun, Z. (2020). A review on single-phase convective heat transfer enhancement based on multi-longitudinal vortices in heat exchanger tubes. Applied Thermal Engineering, 164, 114475. https://doi.org/10.1016/j.applthermaleng.2019.114475and applications. *Neural Computing and Applications*, *32*(16), 12381–12401.

APPENDICES

Appendix A

Table A1. Lobed swirl development under 90 degrees

Plane No.	R_{cs}	r_{lobe}	X/L	Twist degree Clockwise
1	19.452	31.818	0	0
2	19.452	31.818	0.05	4.5
3	19.452	31.818	0.1	9
4	19.452	31.818	0.15	13.5
5	19.452	31.818	0.2	18
6	19.452	31.818	0.25	22.5
7	19.452	31.818	0.3	27
8	19.452	31.818	0.35	31.5
9	19.452	31.818	0.4	36
10	19.452	31.818	0.45	40.5
11	19.452	31.818	0.5	45
12	19.452	31.818	0.55	49.5
13	19.452	31.818	0.6	54
14	19.452	31.818	0.65	58.5
15	19.452	31.818	0.7	63
16	19.452	31.818	0.75	67.5
17	19.452	31.818	0.8	72
18	19.452	31.818	0.85	76.5
19	19.452	31.818	0.9	81
20	19.452	31.818	0.95	85.5
21	19.452	31.818	1	90

Table A2. Lobed swirl development under 180 degrees

Plane No.	R_{cs}	r_{lobe}	X/L	Twist degree Clockwise
1	19.452	31.818	0	0
2	19.452	31.818	0.05	9
3	19.452	31.818	0.1	18
4	19.452	31.818	0.15	27
5	19.452	31.818	0.2	36
6	19.452	31.818	0.25	45
7	19.452	31.818	0.3	54
8	19.452	31.818	0.35	63
9	19.452	31.818	0.4	72
10	19.452	31.818	0.45	81
11	19.452	31.818	0.5	90
12	19.452	31.818	0.55	99
13	19.452	31.818	0.6	108
14	19.452	31.818	0.65	117
15	19.452	31.818	0.7	126
16	19.452	31.818	0.75	135
17	19.452	31.818	0.8	144
18	19.452	31.818	0.85	153
19	19.452	31.818	0.9	162
20	19.452	31.818	0.95	171
21	19.452	31.818	1	180

Table A3. Lobed swirl development under 270 degrees

Plane No.	R_{cs}	r_{lobe}	X/L	Twist degree Clockwise
1	19.452	31.818	0	0
2	19.452	31.818	0.05	13.5
3	19.452	31.818	0.1	27
4	19.452	31.818	0.15	40.5
5	19.452	31.818	0.2	54
6	19.452	31.818	0.25	67.5
7	19.452	31.818	0.3	81
8	19.452	31.818	0.35	94.5
9	19.452	31.818	0.4	108
10	19.452	31.818	0.45	121.5
11	19.452	31.818	0.5	135
12	19.452	31.818	0.55	148.5
13	19.452	31.818	0.6	162
14	19.452	31.818	0.65	175.5
15	19.452	31.818	0.7	189
16	19.452	31.818	0.75	202.5
17	19.452	31.818	0.8	216
18	19.452	31.818	0.85	229.5
19	19.452	31.818	0.9	243
20	19.452	31.818	0.95	256.5
21	19.452	31.818	1	270

Table A4. Lobed swirl development under 360 degrees

Plane No.	R_{cs}	r_{lobe}	X/L	Twist degree Clockwise
1	19.452	31.818	0	0
2	19.452	31.818	0.05	18
3	19.452	31.818	0.1	36
4	19.452	31.818	0.15	54
5	19.452	31.818	0.2	72
6	19.452	31.818	0.25	90
7	19.452	31.818	0.3	108
8	19.452	31.818	0.35	126
9	19.452	31.818	0.4	144
10	19.452	31.818	0.45	162
11	19.452	31.818	0.5	180
12	19.452	31.818	0.55	198
13	19.452	31.818	0.6	216
14	19.452	31.818	0.65	234
15	19.452	31.818	0.7	252
16	19.452	31.818	0.75	270
17	19.452	31.818	0.8	288
18	19.452	31.818	0.85	306
19	19.452	31.818	0.9	324
20	19.452	31.818	0.95	342
21	19.452	31.818	1	360

Table A5. Lobed swirl development under 450 degrees

Plane No.	R_{cs}	r_{lobe}	X/L	Twist degree Clockwise
1	19.452	31.818	0	0
2	19.452	31.818	0.05	22.5
3	19.452	31.818	0.1	45
4	19.452	31.818	0.15	67.5
5	19.452	31.818	0.2	90
6	19.452	31.818	0.25	112.5
7	19.452	31.818	0.3	135
8	19.452	31.818	0.35	157.5
9	19.452	31.818	0.4	180
10	19.452	31.818	0.45	202.5
11	19.452	31.818	0.5	225
12	19.452	31.818	0.55	247.5
13	19.452	31.818	0.6	270
14	19.452	31.818	0.65	292.5
15	19.452	31.818	0.7	315
16	19.452	31.818	0.75	337.5
17	19.452	31.818	0.8	360
18	19.452	31.818	0.85	382.5
19	19.452	31.818	0.9	405
20	19.452	31.818	0.95	427.5
21	19.452	31.818	1	450

Table A6. The calculation of the development transition part

Υ/deg	***f1***	***f***	***Rcs***	***y(mm)***	***rlobe***	***LAi***	***LAfd***	***α-Transition***	***X/L***	***β-Transition***	***X/L***	***Variable Helix (t=1)***
45	0	0.2854	25	0	25	0	763.7934	763.7934	0	0	0	0
46	0.0243	0.3032	24.8809	0.6036	24.4579	18.6614	763.7934	763.7934	0.0999	0.1224	0.2275	20.4783
47	0.0477	0.3215	24.7621	1.1814	23.9413	37.1867	763.7934	763.7934	0.1416	0.1731	0.2732	24.585
48	0.0704	0.3405	24.6436	1.7353	23.4487	55.5813	763.7934	763.7934	0.1739	0.212	0.3046	27.4157
49	0.0924	0.3601	24.5254	2.2665	22.9787	73.8504	763.7934	763.7934	0.2013	0.2448	0.3295	29.6579
50	0.1138	0.3803	24.4073	2.7765	22.5297	91.999	763.7934	763.7934	0.2256	0.2738	0.3506	31.5525
55	0.212	0.4901	23.8192	5.0486	20.5616	181.1039	763.7934	763.7934	0.3238	0.3884	0.4283	38.5496
60	0.2988	0.6142	23.2322	6.9421	18.9695	267.8834	763.7934	763.7934	0.4035	0.4784	0.4863	43.7644
65	0.3773	0.7514	22.6428	8.5436	17.6666	352.8349	763.7934	763.7934	0.4758	0.5577	0.5368	48.3131
70	0.4497	0.9003	22.0477	9.9142	16.5911	436.396	763.7934	763.7934	0.5456	0.6323	0.5853	52.674
75	0.5176	1.059	21.4435	11.0983	15.6982	518.9533	763.7934	763.7934	0.6168	0.7069	0.6358	57.2225
80	0.5823	1.2253	20.8269	12.1283	14.9543	600.8473	763.7934	763.7934	0.6943	0.7864	0.6941	62.4721
85	0.6451	1.3967	20.1943	13.0283	14.3343	682.3756	763.7934	763.7934	0.7883	0.8786	0.7734	69.6085
86	0.6576	1.4314	20.0656	13.1943	14.2233	698.6606	763.7934	763.7934	0.8113	0.8997	0.7949	71.5388
87	0.6699	1.4662	19.936	13.3561	14.1163	714.9432	763.7934	763.7934	0.8372	0.9221	0.82	73.7985
88	0.6823	1.501	19.8056	13.5136	14.0133	731.225	763.7934	763.7934	0.8676	0.9461	0.8509	76.5777
89	0.6947	1.5359	19.6743	13.667	13.914	747.5079	763.7934	763.7934	0.9067	0.9719	0.8928	80.3563
90	0.707	1.5708	19.5422	13.8163	13.8184	763.7934	763.7934	763.7934	1	1	1	90

Appendix B

Appendix B1. Temperture Calibrator

Appendix B2. Power supply

Appendix B3. A digital multimeter

Appendix B4. Industrial water chiller

Appendix B5. Differential pressure gauge

Appendix B6. Thermocouples

Appendix B7. Data logger device

Appendix B8. A flow meter (FC-SD85L-L200)

Appendix B9. A High-accuracy weighing scale (Sartorius, M-pact AX224)

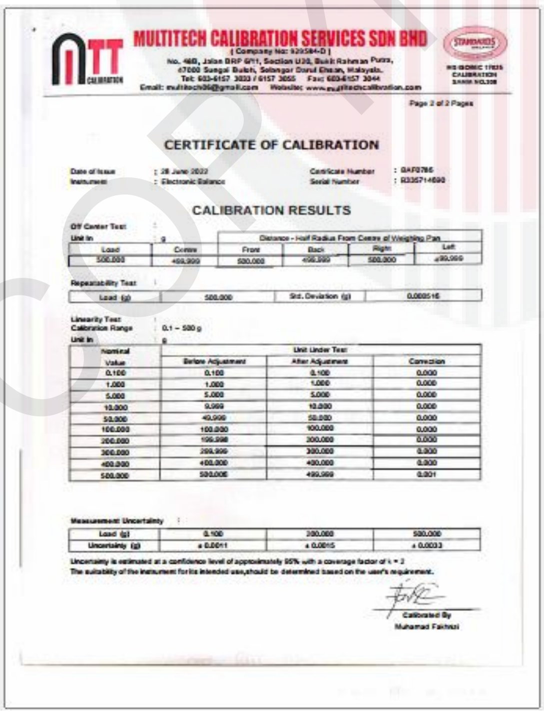

MULTITECH CALIBRATION SERVICES SDN BHD
(Company No: 929584-D)
No. 48B, Jalan BRP 6/11, Section U20, Bukit Rahman Putra,
47000 Sungai Buloh, Selangor Darul Ehsan, Malaysia.
Tel: 603-6157 3033 / 6157 3055 Fax: 603-6157 3044
Email: multitech86@gmail.com Website: www.multitechcalibration.com

STANDARDS MALAYSIA
MS ISO/IEC 17025 CALIBRATION SAMM NO.308

Page 2 of 2 Pages

CERTIFICATE OF CALIBRATION

Date of Issue : 28 June 2022
Instrument : Electronic Balance
Certificate Number : BAF0786
Serial Number : B335714690

CALIBRATION RESULTS

Off Center Test :
Unit In : g

Load	Centre	Distance - Half Radius From Centre of Weighing Pan			
		Front	Back	Right	Left
500.000	499.999	500.000	499.999	500.000	499.999

Repeatability Test :

Load (g)	500.000	Std. Deviation (g)	0.000516

Linearity Test :
Calibration Range : 0.1 – 500 g
Unit In : g

Nominal Value	Unit Under Test		
	Before Adjustment	After Adjustment	Correction
0.100	0.100	0.100	0.000
1.000	1.000	1.000	0.000
5.000	5.000	5.000	0.000
10.000	9.999	10.000	0.000
50.000	49.999	50.000	0.000
100.000	100.000	100.000	0.000
200.000	199.998	200.000	0.000
300.000	299.999	300.000	0.000
400.000	400.000	400.000	0.000
500.000	500.006	499.999	0.001

Measurement Uncertainty :

Load (g)	0.100	200.000	500.000
Uncertainty (g)	± 0.0011	± 0.0015	± 0.0033

Uncertainty is estimated at a confidence level of approximately 95% with a coverage factor of k = 2
The suitability of the instrument for its intended use,should be determined based on the user's requirement.

Calibrated By
Muhamad Fakhrul

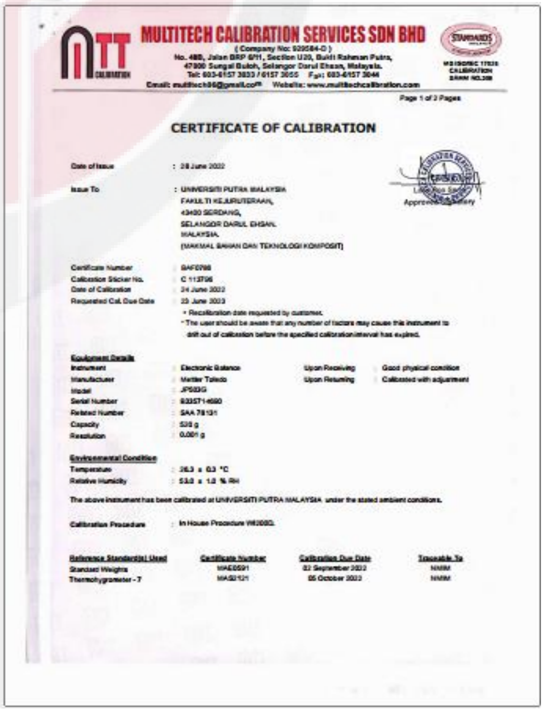

MULTITECH CALIBRATION SERVICES SDN BHD
(Company No: 929584-D)
No. 48B, Jalan BRP 6/11, Section U20, Bukit Rahman Putra,
47000 Sungai Buloh, Selangor Darul Ehsan, Malaysia.
Tel: 603-6157 3033 / 6157 3055 Fax: 603-6157 3044
Email: multitech86@gmail.com Website: www.multitechcalibration.com

STANDARDS MALAYSIA
MS ISO/IEC 17025 CALIBRATION SAMM NO.308

Page 1 of 2 Pages

CERTIFICATE OF CALIBRATION

Date of Issue : 28 June 2022

Issue To : UNIVERSITI PUTRA MALAYSIA
FAKULTI KEJURUTERAAN,
43400 SERDANG,
SELANGOR DARUL EHSAN.
MALAYSIA.
(MAKMAL BAHAN DAN TEKNOLOGI KOMPOSIT)

Approved Signatory

Certificate Number : BAF0786
Calibration Sticker No. : C 113796
Date of Calibration : 24 June 2022
Requested Cal. Due Date : 23 June 2023
* Recalibration date requested by customer.
* The user should be aware that any number of factors may cause this instrument to drift out of calibration before the specified calibration interval has expired.

Equipment Details
Instrument : Electronic Balance
Manufacturer : Mettler Toledo
Model : JP503G
Serial Number : B335714690
Related Number : SAA 78131
Capacity : 520 g
Resolution : 0.001 g
Upon Receiving : Good physical condition
Upon Returning : Calibrated with adjustment

Environmental Condition
Temperature : 26.3 ± 0.3 °C
Relative Humidity : 53.0 ± 1.0 % RH

The above instrument has been calibrated at UNIVERSITI PUTRA MALAYSIA under the stated ambient conditions.

Calibration Procedure : In House Procedure WI200D.

Reference Standard(s) Used	Certificate Number	Calibration Due Date	Traceable To
Standard Weights	MAE0591	02 September 2022	NMM
Thermohygrometer - 7	MAS0121	05 October 2022	NMM

Appendix B10. Electronic Balance

Appendix B11. Hot plate magnetic stirring

Appendix B12. Hot bath sonication (SOO347181)

Trescal

| CALIBRATION SOLUTIONS TO IMPROVE YOUR PERFORMANCE |

STANDARDS MALAYSIA SAMM 011

Certificate of Calibration

Cert. No. PSYP- 22034837

Page 1 of 2

Reference No	R122073607
Date of Issue	02 Jun 2022
Customer	UNIVERSITI PUTRA MALAYSIA Blok G2.4 Fakulti Kejuruteraan Universiti Putra Malaysia 43400 Serdang Selangor
ID: 039048	
Instrument	Viscometer
Model	AND SV-10
Serial No	14800345
Control No	CA7644E
Equipment ID	N/A
Capacity/Range	0.3 mPa.s to 10000 mPa.s
Date of Calibration	02 Jun 2022
Recalibration Date (Specified by Customer)	02 Jun 2023 The User should be aware there are many factors may cause this instrument to drift out of calibration limits prior to the stated recalibration date
Condition of Instrument	
Before Calibration	Good Physical Condition
After Calibration	Calibrated and Serviceable
Location of Calibration	Trescal Laboratory
Calibration Environment	(23 ± 2) °C, (55 ± 10) %rh
Calibration Method	LCP.01503

Reference Standard Used

Reference Instrument	Equipment ID	Control No	Certificate No	Traceable to	Due Date
Standard Oil S200	PH-VY-SO14	C3320V	U3854	NPL	14 Oct 2023
Standard Oil N35	PH-VY-SO15	C3335V	U3544	NPL	14 Oct 2023
Standard Oil S60	PH-VY-SO13	C3360V	U3857	NPL	14 Oct 2023
Thermometer With Sensor	PH-V-TS2	CW2222	PSYP-21087201	NMIM	29 Dec 2022

Calibrated By

Noorbaitisuhaila Binti Mhmd Safii

Approved Signatory

Fatimah Binti Azlan

This certificate is issued in accordance with the condition of accreditation granted by the SAMM which has assessed the measurement capability of the laboratory and its traceability to recognized national standards and to the units of measurement realised to the corresponding national standards laboratory. Copyright of this certificate is owned by the issuing laboratory and may not be reproduced other than in full except with the prior written approval of the Head of the issuing laboratory.

TRESCAL (MALAYSIA) SDN. BHD.

Lot 148, No. 2A, Jalan U1/19, Hicom-Glenmarie Industrial Park, 40150 Shah Alam, Selangor Darul Ehsan, Malaysia. Tel: +603-5569 1648 Fax: +603-5569 1548
www.trescal.com

Trescal

| CALIBRATION SOLUTIONS TO IMPROVE YOUR PERFORMANCE |

STANDARDS MALAYSIA SAMM 011

Certificate of Calibration

Control No. CA7644E

Cert. No. PSYP- 22034837

Page 2 of 2

Instrument Calibrated

Unit of Measurement	mPa.s

Specification (±)
3 % (1 mPa.s to 1000 mPa.s)

Accuracy Test					
Spindle No.	Speed (RPM)	Reference Value At 25 °C	UUT Read At 25 °C	Correction	Specification (±)
N/A	100	7.52	7.63	-0.11	30.00
	50	56.31	57.9	-1.6	30.0
	10	98.83	104.0	-5.2	30.0
	5	394.5	394.0	0.5	30.0
Measurement Uncertainty = 1 % of Reading				k = 2	

Remark : (*) Mean out of specification

TRESCAL (MALAYSIA) SDN. BHD.

Appendix B13. vibro viscometer (AND SV-100) and cirtificate of calibration

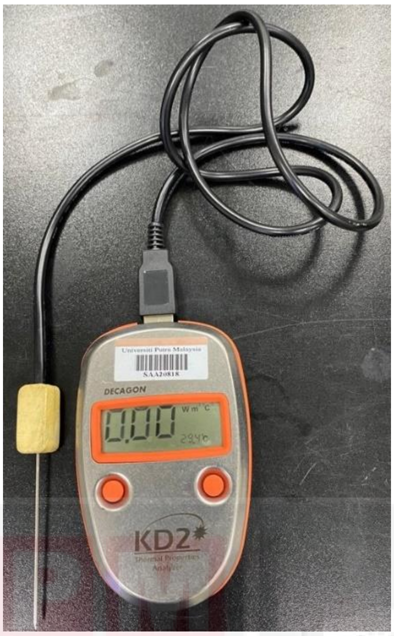

Appendix B14. KD2-Pro thermal conductivity measurement

Appendix C

1- Heat transfer

$$q = \frac{q}{A_c} = \frac{VI}{\pi DL}$$

$$U_q = \sqrt{\left(\frac{\partial q}{\partial V}\ U_V\right)^2 + \left(\frac{\partial q}{\partial I}\ U_I\right)^2 + \left(\frac{\partial q}{\partial L}\ U_L\right)^2 + \left(\frac{\partial q}{\partial D}\ U_D\right)^2} \qquad \text{(B-1)}$$

2- Reynolds number:

$$Re = \frac{4m}{\pi D\mu}$$

$$U_R = \sqrt{\left(\frac{\partial R}{\partial m}\ U_m\right)^2 + \left(\frac{\partial R}{\partial D}\ U_D\right)^2 + \left(\frac{\partial R}{\partial \mu}\ U_\mu\right)^2} \qquad \text{(B-2)}$$

3- Heat transfer coefficient:

$$h = \frac{q}{(T_w - T_b)}$$

$$U_h = \sqrt{\left(\frac{\partial h}{\partial q}\ U_q\right)^2 + \left(\frac{\partial h}{\partial T_w}\ U_{T_w}\right)^2 + \left(\frac{\partial h}{\partial T_b}\ U_{T_b}\right)^2} \qquad \text{(B- 3)}$$

4- Nusselt number:

$$Nu = \frac{hD}{K}$$

$$U_{Nu} = \sqrt{\left(\frac{\partial Nu}{\partial h}\ U_h\right)^2 + \left(\frac{\partial Nu}{\partial D}\ U_D\right)^2 + \left(\frac{\partial Nu}{\partial K}\ U_K\right)^2} \qquad \text{(B-4)}$$

5- Friction factor:

$$f\ = \frac{\Delta P}{\left(\frac{L}{D}\right)\left(\frac{\rho v^2}{2}\right)}$$

$$U_f = \sqrt{\left(\frac{\partial f}{\partial \Delta p}\ U_{\Delta P}\right)^2 + \left(\frac{\partial f}{\partial D}\ U_D\right)^2 + \left(\frac{\partial f}{\partial \rho}\ U_\rho\right)^2 + \left(\frac{\partial f}{\partial L}\ U_L\right)^2 + \left(\frac{\partial f}{\partial v}\ U_v\right)^2} \qquad \text{(B-5)}$$

BIODATA OF STUDENT

Farag Abd Allah Diabis Ayad was born in Albayidha, Libya, On 04th Jun 1971. He received his Bachelor in the power of Electrical Energy in Mechanical Engineering degree from the College of Electrical and Electronic Technology, Benghazi 1993. He received his Master of Mechanical Engineering (Energy Engineering) program from the faculty of Mechanical Engineering, Universiti Teknikal Malaysia (UTeM) in the semester 2018/2019. He embarked on his PhD research titled "EXPERIMENTAL AND NUMERICAL STUDY ON THE THERMAL PERFORMANCE OF 4-LOBE SWIRL GENERATOR UNDER DIFFERENT TWISTED ANGLES AND β-TRANSITION USING GO-CuO/WATER, SiO_2/WATER NANOFLUIDS" at Universiti Putra Malaysia on 11-NOV-2019. He can be contacted at faragayad61@gmail.com

LIST OF PUBLICATIONS

F. A. Diabis, A. Rahim, A. Talib, Y. Al-tarazi, N. Mazlan, and E. Elianddy., (2022) Thermal Performance of Four-Lobe Swirl Generator and its Transition Parts Under Different Type of Nanofluids. CFD Lett, vol. 11, no. 11, pp. 63–74, 2022, doi: https://doi.org/10.37934/cfdl.14.11.6374.

F. A. Diabis, A. Rahim, A. Talib, N. Mazlan, E. Elianddy, T. Yusaf and U. Kale., (2024) Review on heat transfer enhancement and fluid flow characteristics of lobe swirl generators Journal of King Saud University – Science-Acceptable for publication Ref.: Ms. No. JKSUS-D-22-01341R2

Diabis, F. A., Mazlan, N., & Supeni, E. E. (2025). An experimental study on the effect of lobe swirl device and its transition parts on thermal performance using Graphene-CuO/water nanohybrid. Case Studies in Thermal Engineering, 68, 105925. https://doi.org/10.1016/j.csite.2025.105925

F. A. Diabis, A. Rahim, A. Talib, N. Mazlan, E. Elianddy, (2025). Numerical study on the effect of four-lobe swiri geerator and its transition parts on thermal performance enhancement and fluid flow. CFD Letter Journal -Acceptable for publication